In presenting the dissertation as a partial fulfillment of the requirements for an advanced degree from the Georgia Institute of Technology, I agree that the Library of the Institute shall make it available for inspection and circulation in accordance with its regulations governing materials of this type. I agree that permission to copy from, or to publish from, this dissertation may be granted by the professor under whose direction it was written, or, in his absence, by the Dean of the Graduate Division when such copying or publication is solely for scholarly purposes and does not involve potential financial gain. It is understood that any copying from, or publication of, this dissertation which involves potential financial gain will not be allowed without written permission.

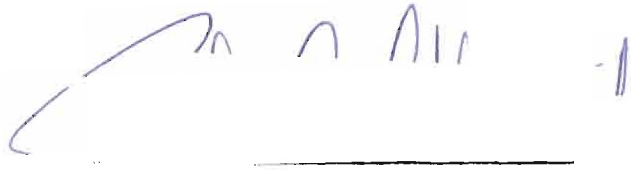

7/25/68

PHYSICAL ADSORPTION ON CRYSTALLINE TITANIUM CARBIDE

A THESIS

Presented to

The Faculty of the Graduate Division

by

Richard George Varsanik

In Partial Fulfillment

of the Requirements for the Degree

Doctor of Philosophy

in the School of Chemistry

Georgia Institute of Technology

June, 1972

PHYSICAL ADSORPTION ON CRYSTALLINE TITANIUM CARBIDE

Approved:

Chairman

Date approved by Chairman: 4 June, 1972

DEDICATION

This thesis is dedicated to my wife Rosemarie.

ACKNOWLEDGMENT

The author wishes to express his appreciation to his thesis advisor, Dr. Bruce W. Davis, for his encouragement, and to the Petroleum Research Foundation for their support.

TABLE OF CONTENTS

Page

DEDICATION ii

ACKNOWLEDGMENTS. iii

LIST OF TABLES vi

LIST OF ILLUSTRATIONS. viii

SUMMARY. x

Chapter

I. INTRODUCTION. 1

The Gas-Sold System 1
The Solid Surface 3
Powder Metallurgy Techniques for Preparing Stoichiometric Transition Metal Carbides 8
Statement of the Problem. 11

II. PREPARATION AND CHARACTERIZATION OF TITANIUM CARBIDE. . . . 14

Preparation of Titanium Carbide 14
The Reaction System 15
Characterization of Titanium Carbide. 17
X-Ray Diffraction 17
Results and Discussion of X-Ray Data. 21
Electron Diffraction. 25
Electron Microscopy 28
X-Ray Emission Microprobe Analysis. 34

III. EXPERIMENTAL EQUIPMENT AND PROCEDURES 36

The Adsorption System 36
The McLeod Gauge. 39
Thermal Transpiration Corrections 42
Construction and Calibration of the McLeod Gauge and Bulb B1 45
Materials 49
The Adsorption System for Studying Benzene on TiC-8 52
The Cryostat. 53

Chapter Page

III. EXPERIMENTAL EQUIPMENT AND PROCEDURES (Continued)

Calibration of High Pressure Side and Calculation of Adsorption Isotherms. 57
Calibration of Low Pressure Side and Calculation of Adsorption Isotherms. 62

IV. THERMODYNAMICS OF ADSORPTION. 63

V. ADSORPTION MEASUREMENTS 67

Adsorption of Ar and N_2 in the High Pressure Range. 67
Adsorption of Argon and Methane in the Low Pressure Range. 73

VI. SITE ENERGY DISTRIBUTIONS 90

The Langmuir Equation 90
Localized Harmonic Oscillator Model 96
Evaluation of b° for Benzene-- Localized Harmonic Oscillator Model. 100
Localized Particle-in-a-Box Model 104
Evaluation of b° for Benzene-- Localized Particle-in-a-Box Model. 107
Langmuir Equation with Lateral Interactions 111
Calculation of Site Energy Distributions. 113

VII. CONCLUSIONS AND RECOMMENDATIONS 123

Conclusions 123
Recommendations 124

APPENDIX A 125

APPENDIX B 129

APPENDIX C 140

APPENDIX D 149

BIBLIOGRAPHY 152

VITA 158

LIST OF TABLES

Table		Page
1.	Crystal Lattice Constants for TiC	22
2.	X-Ray Emission Electron Microprobe Analysis of Impurities.	35
3.	McLeod Gauge and B1 Volumes	47
4.	Capillary Corrections	48
5.	Monolayer Capacities and Adsorbate Cross-Sections	89
6.	Localized Monolayer--Harmonic Oscillator Model Parameters, Entropies and Vibrational Frequencies for Benzene on TiC-8.	105
7.	Localized Monolayer--Particle-in-a-Box Model Parameters, Entropies, and Vibrational Frequencies for Benzene on TiC-8.	110
8.	Antoine Constants	127
9.	C_6H_6—TiC-8 Isotherm at 273.35°K.	130
10.	C_6H_6—TiC-8 Isotherm at 268.11°K.	131
11.	C_6H_6—TiC-8 Isotherm at 263.01°K.	132
12.	C_6H_6—TiC-8 Isotherm at 258.62°K.	133
13.	C_6H_6—TiC-8 Isotherm at 251.73°K.	134
14.	C_6H_6—TiC-8 Isotherm at 77.08°K	135
15.	Ar—TiC-8 Isotherm at 77.08°K	136
16.	Ar—TiC-8 Isotherm at 90.05°K	137
17.	N_2—TiC-8 Isotherm at 77.23°K	138
18.	CH_4—TiC-8 Isotherm at 77.10°K.	139
19.	Spreading Pressures for Benzene on TiC-8 at 258.62°K.	141

Table		Page
20.	Spreading Pressures for Benzene on TiC-8 at 273.35°K. . . .	142
21.	Spreading Pressures for Benzene on TiC-8 at 268.11°K. . . .	143
22.	Spreading Pressures for Benzene on TiC-8 at 263.01°K. . . .	144
23.	Spreading Pressures for Benzene on TiC-8 at 251.73°K. . . .	145
24.	Isothermal Differential Heats of Adsorption for Benzene on TiC-8	146
25.	Isosteric Heats of Adsorption for Argon on TiC-8.	147
26.	Isosteric Heats of Adsorption for Benzene on TiC-8.	148

LIST OF ILLUSTRATIONS

Figure		Page
1.	The Reaction System	16
2.	The Geometry of Diffraction	19
3.	The Straumanis Film Mounting in the Debye-Scherrer Powder Camera.	20
4.	X-Ray Diffraction Powder Patterns	24
5.	Electron Diffraction Pattern for TiC-8.	29
6.	Transmission Electron Micrograph of Sterling FT and TiC-8.	30
7.	Scanning Electron Micrograph of TiC-8	32
8.	The High Pressure Side, Side 1.	37
9.	The Low Pressure Side, Side 2	38
10.	The McLeod Gauge.	40
11.	The Cryostat.	54
12.	The Dead Space.	59
13.	The Adsorption Sample Cell.	68
14.	Adsorption Isotherms of Nitrogen at 77°K.	69
15.	Adsorption Isotherms of Argon at 77°K	72
16.	Adsorption Isotherms of Methane at 77°K	74
17.	Adsorption Isotherms of Argon on TiC-8.	76
18.	Adsorption Isotherms of Argon on TiC-8.	77
19.	Adsorption Isotherms of Argon on TiC-8.	78
20.	Isosteric Heats of Argon on P33 (2700°) and TiC-8	79

Figure Page

21. Adsorption Isotherms of Benzene on TiC-8. 81

22. Adsorption Isotherms of Benzene on TiC-8. 82

23. Adsorption Isotherms of Benzene on TiC-8. 83

24. Adsorption Isotherms of Benzene on TiC-8. 84

25. Adsorption Isotherms of Benzene on TiC-8. 85

26. Adsorption Isotherms of Benzene on TiC-8. 86

27. Adsorption Isotherms of Benzene on TiC-8. 87

28. Isosteric Heats of Benzene on Sterling MT and TiC-8 88

29. Site Energy Distribution Curve for Benzene on TiC-8 118

30. Site Energy Distribution Curve for Argon on TiC-8 120

31. Site Energy Distribution Curve for Argon on MT-3100 121

SUMMARY

A crystalline stoichiometric titanium carbide was prepared by the reaction of titanium hydride and Sterling FT graphitized carbon at 1250±50°C. The resultant carbide was examined using x-ray powder diffraction techniques and its crystal lattice constant was found to be 4.3268±0.0006Å. Electron diffraction patterns from a small grouping of the polyhedral crystallites yielded a crystal lattice constant of 4.32±0.03Å, which confirmed the x-ray diffraction results. X-ray emission electronmicroprobe analysis indicated that the titanium carbide formed contained only about 1.2wt% impurities. Analysis of transmission electron micrographs yielded a surface area of 4.4±0.5 m^2/g.

A volumetric gas adsorption apparatus was constructed which is capable of studying the physical adsorption of gases over a pressure range of 2×10^{-5} to 50 torr and 50-500 torr. This apparatus was used to study physical adsorption on titanium carbide of nitrogen and argon at 77°K in the range of 50-500 torr and methane at 77°K and argon at 77°K and 90°K over the range of 2×10^{-5} to 50 torr. A nitrogen surface area of 6.5 m^2/g was found for the titanium carbide.

A cryostat was constructed which is capable of holding any temperature over the range of 250-270°K to within ±0.02°K for extended periods. The physical adsorption of benzene on titanium carbide was studied over the pressure range of 2×10^{-5}-25 torr and over a temperature range of 251-273°K.

Adsorption isotherms obtained on titanium carbide are compared to those obtained on various graphitized carbon blacks. The isosteric heats of adsorption for argon and benzene on titanium carbide are calculated and compared to those found on various carbon blacks. For benzene on titanium carbide spreading pressures and isothermal differential heats of adsorption are calculated.

Distributions of site energies for the titanium carbide surface are then calculated for agon and benzene. For benzene the Langmuir equation for localized adsorption is chosen as the local isotherm function and two models are based upon this equation. The first model assumes the adsorbed molecule to be a three-dimensional harmonic oscillator about a fixed point on the surface, and the second model assumes the molecule is free to translate about a two-dimensional box whose area is equal to the size of the adsorption site. Analysis of the site energy distributions obtained from each model suggests that the particle-in-a-box model is the more correct one.

For argon the Langmuir plus lateral interaction equation is used as the local isotherm function, and the best value for the interaction energy is found to be 462.5 cal/mole.

CHAPTER I

INTRODUCTION

The Gas-Solid System

When a gas is in equilibrium with a solid substrate, a concentration gradient of gas molecules will develop at the gas-solid interface. This build-up of gas molecules at the gas-solid interface is known as adsorption.

Adsorption will occur with any gas-solid system at any temperature, however, as the temperature of the system is raised, or if gases of low molecular weight are used the amount of adsorption becomes increasingly difficult to measure. At this point it is imperative that we make a distinction between two different types of adsorption, namely chemisorption and physical adsorption. In chemisorption the gas molecule is held to the surface by a chemical bond; i.e., a chemical reaction has occurred between the gas molecule and the molecules of the solid surface (known henceforth as the adsorbent) to form a new chemical species as a part of the surface. In physical adsorption the forces involved are the mutually attractive (and repulsive) forces of the gas molecule and the surface. Adsorption must not be viewed as a static but rather as a dynamic situation. The admolecule (adsorbed gas molecule) is in a state of dynamic equilibrium between the gas phase and the adsorbed phase.

We have been discussing the completely idealized case of a surface whose every part appears the same as every other part to the gas molecule, except of course for periodic undulations in potential energy due to the surface structure. This is the so-called homogeneous surface which can never exist in its pure form--although it is very closely approximated by some adsorbents. A "real" surface consisting of cracks and dislocations along with contributions due to nearly-homogeneous areas does not necessarily exhibit the same degree of attraction for the gas molecule, and indeed if several different crystal faces are involved, we can say that they certainly will not be equally attractive to the gas molecule.

The study of the physical adsorption of a gas on a solid surface can serve as a probe into the nature of the solid surface and into the nature and magnitude of the forces involved between molecules in the vicinity of the surface. To use this probe we measure what is known as an adsorption isotherm. This is a plot of the concentration of gas molecules in the adsorbed phase versus the concentration of gas molecules in the gas phase at a constant temperature.

An ideal situation would be to develop a realistic statistical mechanical model of the adsorption of a gas on a surface and to describe this model in the form of an isotherm equation. Many such isotherm equations have been developed, and great care must be exercised when interpreting experimental results in the framework of a particular adsorption model. One must be careful since virtually all models have used an idealized surface consisting of either a completely smooth

interaction potential or a single type of adsorption site. An obvious extension in the application of nearly any isotherm equation developed for an idealized surface to a real heterogeneous surface is to use the idealized surface equations for the portion of the total surface which is homogeneous, along with a suitable distribution of local interaction energies. This approach was developed by Adamson and co-workers (1,2) into a useable form, later used extensively by Hseih (3,4), and was used in this work to determine the distribution of site energies for argon and benzene on titanium carbide. The sub-monolayer region of the experimental adsorption isotherms was used along with a suitable local isotherm function to determine the distribution of site energies on the titanium carbide surface. These site energy distributions then compared with the site energy distributions for argon on a graphitized carbon (MT-3100). This information when combined with the information gained from the adsorption isotherms and the isosteric heats of adsorption of various adsorbates on both titanium carbide and graphitized carbon blacks enables us to draw some conclusions regarding the nature of the titanium carbide surface.

The Solid Surface

Substrates chosen for gas adsorption studies are usually of a few main types; the graphitized carbons (5), the alkali halides (6), the transition metal oxides (7), the metal halides (8), boron nitride (9), and metals (10). These particular surfaces have received much attention for several reasons. First, they possess a high degree of homogeneity, and are thus well suited for the purpose of gaining

information about the "idealized" surface. Second, they can be prepared with relative ease, and lastly, they can be prepared in a reproducible fashion. Recently, Dormant and Adamson (11) attempted to add molecular solids (e.g., H_2O, NH_3, CH_3OH) to the main types of substrates; however, the study of the molecular solids is complicated by sintering effects which reduce the surface area and make physical adsorption measurements uncommonly difficult.

This study was carried out to investigate the possibility of an entire new class of adsorbates--the transition metal carbides and nitrides. All of the transition metal carbides and nitrides are closely related in crystal structure, bonding characteristics, and magnetic and electric properties. These properties would make their study as a group valuable since the effects of a variation in metal component and lattice parameter upon adsorption behavior can be investigated. This relationship is easily understood in view of the similarities between the size, electronegativity, and electron structure of carbon and nitrogen. Transition metal borides do not exhibit these similarities because of the boron-boron bonds which exist in these compounds. Transition metal oxides are also excluded for the most part because they are very difficult to prepare in a pure form and because their surface is very susceptible to contamination with chemisorbed CO_2 and H_2O.

Titanium carbide was chosen for the initial phase of this study, and a brief discussion of the properties of the transition metal carbides and nitrides in general, and of titanium carbide in particular will hopefully serve to illustrate the interesting aspects as well as problems associated with this choice.

1. These compounds are among the hardest known. Most carbides have hardnesses which lie between that of Al_2O_3 and diamond. TiC is the hardest of the carbides at room temperature (12). The hardness of TiC_x is very dependent upon composition and increases sharply as stoichiometry (x=1) is approached (13). This would present a problem since the titanium carbide surface is very sensitive to slight deviations from stoichiometry; thus the utmost care must be taken to insure that a stoichiometric titanium carbide is formed.

2. The transition-metal carbides and nitrides have very high melting points. Titanium carbide melts at 3067°C, and TaC has the highest melting point of any material known, 3983°C (graphite sublimes at about 4000°C) (14). This property would certainly imply that any sintering or alteration of the surface by thermal treatment, using standard equipment, would not be feasible. Thus, the surface, as prepared, must be suitable for gas adsorption studies. This property would also imply that any conventional procedure used to "bake-out" or remove surface contaminants *in vacuuo* could not possibly alter the titanium carbide surface initially formed.

3. The transition metal carbides are extremely strong, particularly at high temperatures. Above the brittle-to-ductile transition point (about 800°C for $TiC_{0.95}$ (15,16)), they are the strongest materials known. The observed tensile strength of a material is directly related to the nature of surface imperfections (17), and the high tensile strength of titanium carbide would indicate that the surface formed would be less likely to be seriously marred by cracks and flaws. The

presence of surface flaws is highly undesirable, since surface flaws contain high energy adsorption sites which are a mark of surface heterogeneity.

The remarkable correlation between tensile strength and surface flaws in titanium carbide can be shown in the studies of the tensile strengths of single crystals of TiC at room temperature as conducted by Williams (18) and Williams and Schaal (19). The strengths of the freshly cleaved crystals ranged from 41,000 to 97,000 psi, and electropolishing to remove surface flaws increased these strengths to 100,000-800,000 psi. Thus, by removing surface flaws with electropolishing, an eight-fold increase in strength was observed. However, we are more interested in the converse of this example; that is, does a compound with an intrinsically higher tensile strength possess an inherently smoother surface? We have seen how removing surface flaws greatly increases tensile strength; now we will compare the tensile strengths of the cleaved crystals with their theoretical tensile strengths. Adamson (17) has given the formula for theoretical tensile strength as

$$2\gamma = d\tau \qquad (I\text{-}1)$$

where 2γ = the work of cohesion.

d = the range of action of the forces between the separating planes.

τ = the tensile strength.

Toth (20) gives the theoretical tensile strength for unpolished titanium carbide crystals as about 2,400,000 psi and the observed

tensile strength for cleaved crystals is about 97,000 psi (18,19) so the observed tensile strength is about 25 times lower than the theoretical tensile strength. Studies performed by Stranski (21) on the change in tensile strength of sodium chloride crystals as their surfaces were gradually etched with a salt solution showed that the observed tensile strength was from a hundredth to a thousandth of the theoretical tensile strength. Thus, we might expect that since crystals of titanium carbide closely approach their theoretical tensile strength they might be expected to form crystals with intrinsically smoother surfaces.

4. The transition metal carbide and nitrides are chemically stable at room temperature, being attacked only by very concentrated acid solutions (except for VC which is slowly attacked by air at room temperature). This property means that the titanium carbide surface, once formed, would require no special handling techniques to protect it from chemical attack.

5. Ideal stoichiometry is usually not found among the transition metal carbides and nitrides, and it is always very difficult to obtain a 1-to-1 metal atom to non-metal atom ratio. This fact makes the crystal structure study of the carbide phases very difficult. However, when the metal atom to non-metal atom ratio is unity, nearly all of the transition-metal carbides and nitrides exhibit B1 crystal structure, as do the alkali halides. Thus, adsorption data obtained on a transition-metal carbide or nitride can be compared with adsorption data obtained on alkali halides, such as sodium chloride. Thus, if we had prepared a sample of titanium carbide which exhibited a homogeneous surface, we

could have performed lattice sums as described by Orr (22) and compared our heats of adsorption, potential energy curves and adsorption isotherms to those obtained by Hayakawa (23) who has done extensive studies on sodium chloride.

Powder Metallurgy Techniques for Preparing Stoichiometric Transition-Metal Carbides

It was decided to begin our study by preparing a carbide of Group IV transition-metal, i.e. Ti, Zr, or Hf. Group IV was chosen because it ideally forms only one carbide, MC, although great care must be exercised to produce a stoichiometric carbide. However, it was felt that titanium carbide would be the easiest carbide to prepare in a pure and stoichiometric form consisting of regular polyhedral crystallites of sub-micron dimensions desirable for gas adsorption studies.

There are four standard classes of reactions employed in the field of powder metallurgy to produce metal carbides (24). The first is the widely-used industrial preparation involving the direct reaction of the metal oxide with excess carbon in a reducing or protective atmosphere, *viz.*

$$MO + 2C \rightarrow MC + CO \qquad (I-2)$$

This synthesis was not used because it generally produces a carbide which is usually badly contaminated with oxygen.

A second reaction involves the reaction of the metal with a carburizing gas (24):

$$M + 2CO \rightarrow MC + CO_2 \qquad (I\text{-}3)$$

$$xM + C_xH_y \rightarrow xMC + \left(\frac{y}{2}\right)H_2 \qquad (I\text{-}4)$$

Reaction (I-3) was discarded since it introduced the possibility of oxygen contamination. Reaction (I-4) was performed using CH_4 and C_2H_4 and in both cases the resultant carbide was a black inhomogeneous mass which was not suitable for gas adsorption studies.

A third class of reactions involves the precipitation from the gas phase by reacting a metal carbonyl or a metal halide in hydrogen (24):

$$M - Carbonyl + H_2 \rightarrow MC + (CO, CO_2, H_2, H_2O) \qquad (I\text{-}5)$$

$$MCl_4 + C_xH_y + 2H_2 \rightarrow MC + 4HCl + (C_mH_m) \qquad (I\text{-}6)$$

Reaction (I-5) was not attempted, but reaction (I-6) was studied extensively using $TiCl_4$ and CH_4 or C_2H_4. The reaction product using CH_4 was not acceptable; however the reaction produce using C_2H_4 seemed at first to prove promising. Unfortunately, subsequent investigation of the TiC formed from $TiCl_4$ and C_2H_4 showed it to be hopelessly contaminated with organic waxes and oils. Mass spectrometric analysis of these waxes and oils showed them to consist of a vast array of both linear and branched hydrocarbons of nearly every conceivable molecular weight. Recently, it has been reported (25) that a commercial process has been

developed by Esso Research and Engineering Company to oligomerize ethylene using $TiCl_4$ and an alkyl aluminum chloride. This process forms olefins having an even number of carbon atoms ranging from C_4 to above C_{1000}! Mass spectrometric examination of the effluent gas from the reaction showed large amounts of HCl and CH_4 along with ethane and propane. Also present were cyclohexane, cyclohexene and benzene. Because of the large amount of contaminants formed, this reaction could not be used to produce a TiC of the desired purity.

A fourth method of preparation entails the reaction of the metal hydride with carbon, or of metal with carbon (24):

$$M + C \rightarrow MC \qquad (I-7)$$

$$2MH + 2C \rightarrow 2MC + H_2 \qquad (I-8)$$

Actually, reaction (I-8) could follow two paths, one as written, and one where the metal hydride first decomposes and then the metal reacts with the carbon as in reaction (I-7). The temperature claimed to be necessary for the reactions of the Group IV transition metal hydrides to form carbides are given by Schwartzkopf and Kieffer (26) as:

$Ti(TiH_2) + C \rightarrow TiC$	1700-2100°C
$Zr(ZrH_2) + C \rightarrow ZrC$	1800-2200°C
$Hf(HfH_2) + C \rightarrow HfC$	1900-2300°C

Bleecker (27) has stated that the reaction of titanium hydride with carbon to form titanium hydride can proceed at temperatures of 1100-1300°C and in this study we have observed the reaction to proceed smoothly and completely at 1250°C, thus confirming the results of Bleecker.

This reaction produced a finely divided, light grey, crystalline TiC which was characterized using X-ray diffraction, electron diffraction, and X-ray emission techniques along with both transmission and scanning electron microscopy.

Statement of the Problem

The purpose of this work was threefold. First, was to produce a sample of stoichiometric titanium carbide of the highest purity possible in the form of a powder containing submicron crystallites of uniform particle morphology. Second, was to characterize the aforementioned stoichiometric titanium carbide using the best methods available to determine its purity along with the nature and source of any contaminants. X-ray diffraction was used to measure the lattice parameter of the titanium carbide formed, and using data given by Storms (28) the carbon-to-metal ratio could be approximated. X-ray emission electron microprobe analysis was used to determine a final carbon-to-metal ratio, as well as to check the final product, the reactants, and the intermediate mixture for purity. Transmission and scanning electron micrographs were employed both to measure an average particle size and to examine the particle morphology of the stoichiometric titanium carbide. The third goal was to construct and calibrate a volumetric adsorption

apparatus in order to study the physical adsorption of selected gases and vapors on this thoroughly characterized stoichiometric titanium carbide, and to extract any information obtainable from the measurements made with this apparatus which relate to the nature of the titanium carbide surface.

The method of attack consisted of:

1. Preparing samples of titanium carbide using the various techniques of powder metallurgy as described in the previous section, and selecting the best method of preparation.

2. Preparing several samples and carefully selecting the best one, with respect to purity, stoichiometry and particle morphology.

3. Thoroughly characterizing the chosen sample with respect to the purity requirements set forth in the above paragraph.

4. Constructing and calibrating a volumetric adsorption apparatus capable of studying any gas or vapor chosen to serve as a probe of the titanium carbide surface.

5. Gathering the necessary data and reducing them to a useable form in order to extract information about the nature of the titanium carbide surface; this includes surface area, the variations of the heat of adsorption

with surface coverage, and a qualitative investigation of the distribution of site energies of the surface.

CHAPTER II

PREPARATION AND CHARACTERIZATION OF TITANIUM CARBIDE

Preparation of Titanium Carbide

The titanium carbide samples finally used in this study were prepared by a synthesis similar to that used by Bleecker (27) and Ogawa and Bando (29). The synthesis involves the following steps:

1. Weighing out and mixing titanium metal with graphitized carbon.
2. Placing the reactants under a hydrogen atmosphere and heating them to convert the titanium metal to its hydride.
3. Raising the temperature to reduce the titanium hydride to titanium metal which in turn reacts to form titanium carbide.
4. Heat treating the resultant titanium carbide *in vacuuo* to remove gaseous impurities.

Several samples of titanium carbide were prepared from reaction mixtures containing either 19.5% graphitized carbon (TiC-8, TiC-9, and TiC-10) or 20% graphitized carbon (TiC-4 and TiC-6). Although the stoichiometric percentage of carbon in titanium carbode is close to 20%, Bleecker (27) recommends the use of 19.5% carbon in the reaction mixture in order to minimize the amount of free, or unreacted carbon in the

resulting carbide. In this study we have confirmed his observation. A reaction mixture was obtained by first weighing out the appropriate amounts of titanium metal (Ventron, 325 mesh lot No. 2F186) and Sterling FT graphitized carbon (Cabot, lot No. D-5) and then mixing the components thoroughly in a small pyrex ball mill for eight hours.

The Reaction System

A 5.0 gram portion of the reaction mixture was spread evenly in a 7×½-inch graphite boat. The graphite boat was machined from a single piece of graphite rod and was designed to pass through a female ℔ 24/40 quartz joint and down the quartz tube into the furnace area. The quartz tube was then sealed onto the manifold with Apiezon W high vacuum black wax. A cylinder of Matheson (Prepurified) Hydrogen fitted with a hydrogen regulator was then attached to the manifold and the system was evacuated. After the quartz tube, manifold, manometer and hydrogen inlet were pumped down to about 10^{-3} torr, the manometer and hydrogen inlet were sealed off with stopcocks A, B, and C. A Hoskins Model FD 303A tube furnace was then put in place and heated to 335±5°C. Outgassing of the sample at 335±5°C continued at 10^{-3} torr for eight hours. Stopcock D was then closed and stopcocks A and C opened, introducing hydrogen gas into the system. The pressure was periodically adjusted to maintain 740 torr during the 72-hour period needed to convert the metal to its hydride. The Hoskins Model FD303A tube furnace was then taken away and a pre-heated Sentry Model VH tube furnace put in place and the system rapidly heated to 1250°C with fluctuations of ±50°C observed. The temperature was read on a Hoskins Pyrometer Type AH

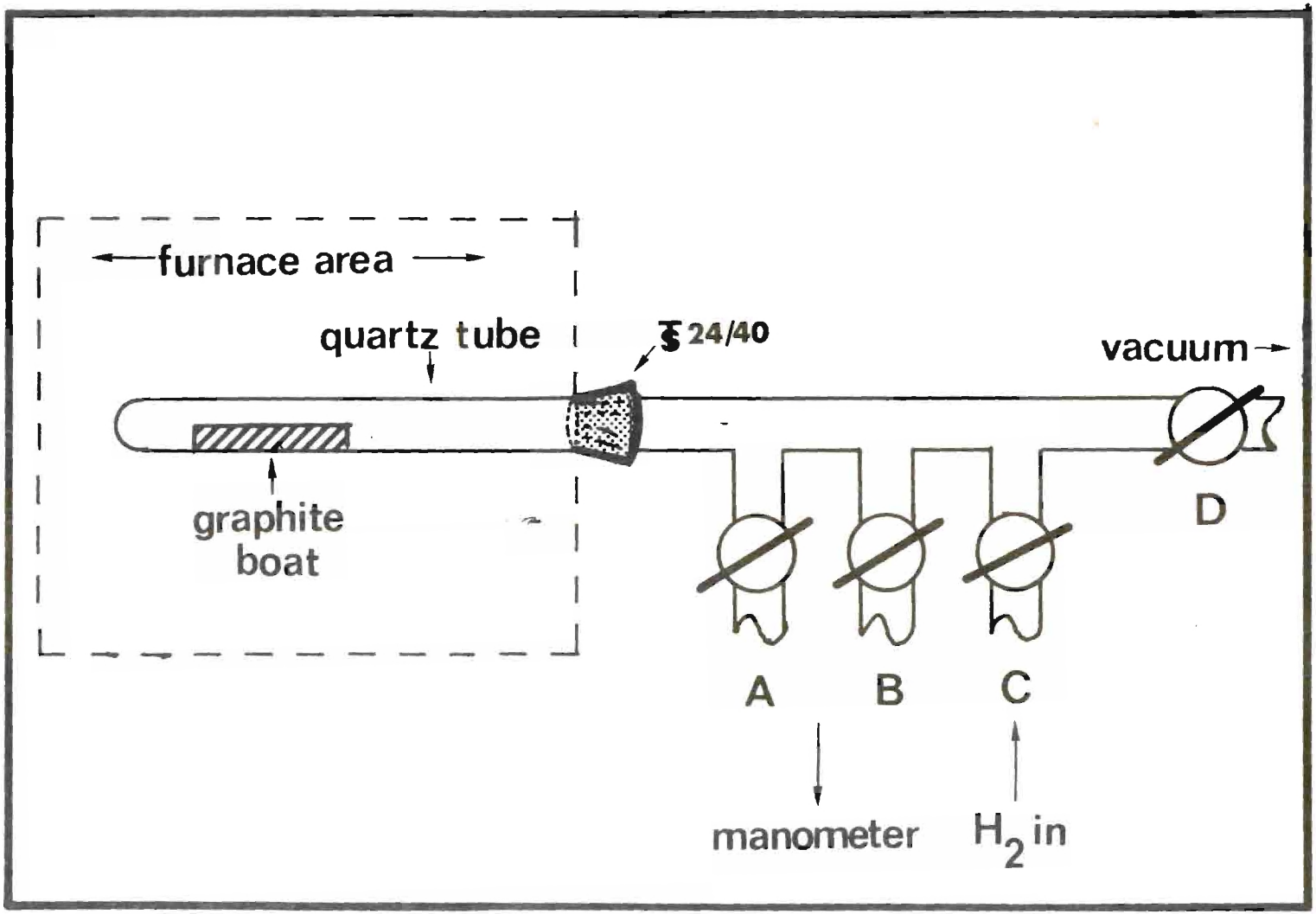

Figure 1. The Reaction System

(No. 29175) which was previously calibrated using the melting point of copper (1083±0.1°C) and sodium chloride (801°C). Besides a small increase due to thermal expansion, there was a substantial pressure increase due to the release of H_2 from the titanium hydride. Consequently, it was necessary to pump off excess H_2 during the rapid heating to maintain pressure of 740 torr. The sample was held at 1250±50°C for eight hours under the hydrogen atmosphere, during which the conversion to titanium carbide went to completion. At the end of the treatment, the system was evacuated and heat treatment continued at 1300±50°C for one hour. Finally, the system was allowed to cool to room temperature and the graphite boat containing the sample was removed.

Characterization of Titanium Carbide

X-Ray Diffraction

All X-ray diffraction measurements on titanium carbide samples were done with Ni filtered copper radiation as recommended by Nuffield (30) in order to give sharp patterns with little background. Each sample for X-ray study was loaded into a 0.5mm, lead-free glass capillary tube and mounted in a Phillips Type 52056/0 Debye-Scherrer camera. Each sample was exposed for 6.5 hours, during which sharp forward rings were produced with little background. Back reflections were too broad and diffuse to be included in the present measurements. Wavelengths used were $CuK_{\alpha 1}$ = 1.5405Å, $CuK_{\alpha 2}$ = 1.5443Å. The weighted average is

$$K_{\alpha} = \frac{(2\alpha_1+\alpha_2)}{3} = 1.5418\text{Å}. \qquad \text{(II-1)}$$

The interplanar spacing, d, was calculated using the Bragg equation,

$$n\lambda = 2d\sin\theta, \qquad \text{(II-2)}$$

which gives the angle θ at which a set of planes of spacind d cooperatively reflect rays of wavelength λ in the *nth* order. The derivation of this equation is shown in Figure 2.

Powder diffraction patterns were photographed on Ilford "Industrial G" X-ray film using a 114.6 mm diameter Debye-Scherrer camera having a Straumanis film mounting. The Debye-Scherrer camera was mounted on a Phillips Type 12045 B/3 X-ray diffraction unit. In the 114.6mm Debye-Scherrer camera, the diameter of the arcs is related to the apex angle of the cone, 4θ, by the conversion factor

$$1^\circ \text{ of } \theta = 2\text{mm of S} \qquad \text{(II-3)}$$

where S is the distance measured on the film.

The exposed film was developed in Kodak Rapid X-ray Developer for the recommended time and then fixed and washed. Diffraction arcs were measured on a Starrett vernier with sliding scale to within ±0.125mm. Although the arc distance FB in the Debye-Scherrer camera (Figure 3a) is exactly 180mm, the film shrinks as it is developed and dried. To correct for this the distance FB (Figure 3b) was measured on the film and the relationship

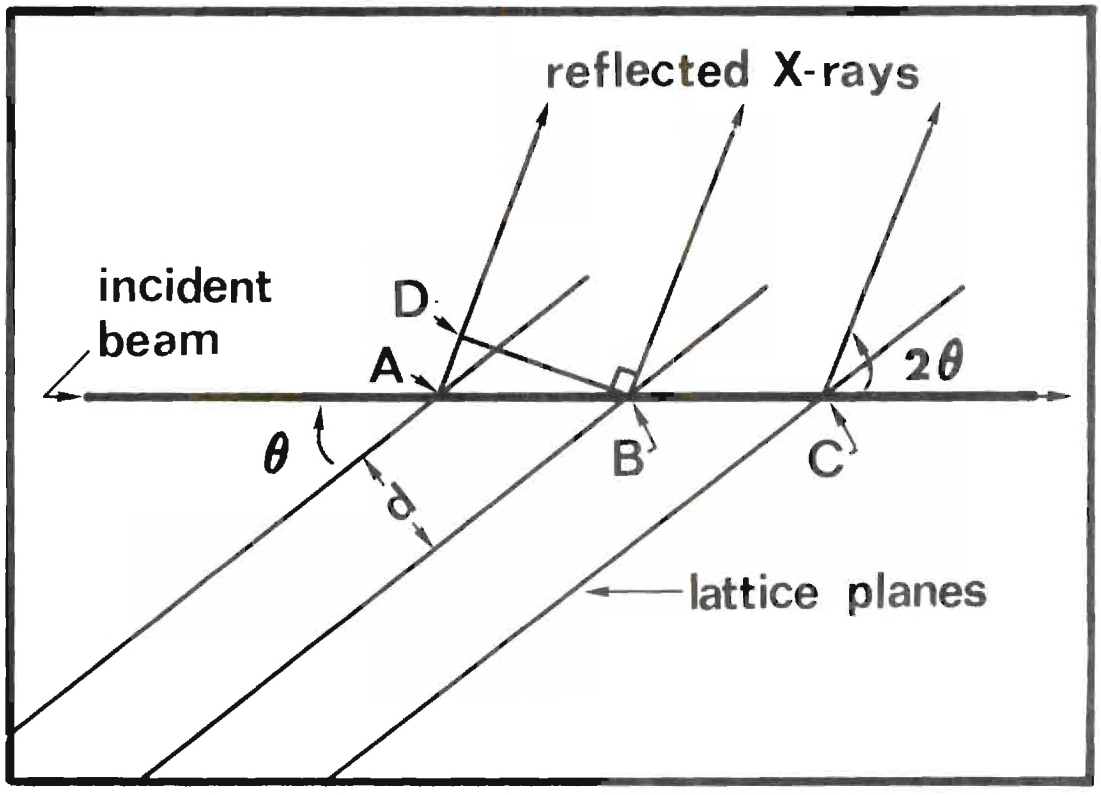

Derivation of the Bragg Law

The lengths AB and AD are given by

$\sin(\angle ABD) = d/AB$; $AB = d/\sin\theta$

$\cos(\angle DAB) = AD/AB$; $AD = (d/\sin\theta)\cos 2\theta$

$AD = AB\cos 2\theta$; $AD = (d/\sin\theta)\cos 2\theta$

The requirement for sucessive reflected rays to be in phase is

$AB - AD = n\lambda$ with $n = 1,2,3\ldots$, thus,

$n\lambda = (d/\sin\theta)(1-\cos 2\theta)$

$= (d/\sin\theta)(2\sin^2\theta)$ or,

$n\lambda = 2d\sin\theta$ which is the Bragg equation.

Figure 2. The Geometry of Diffraction

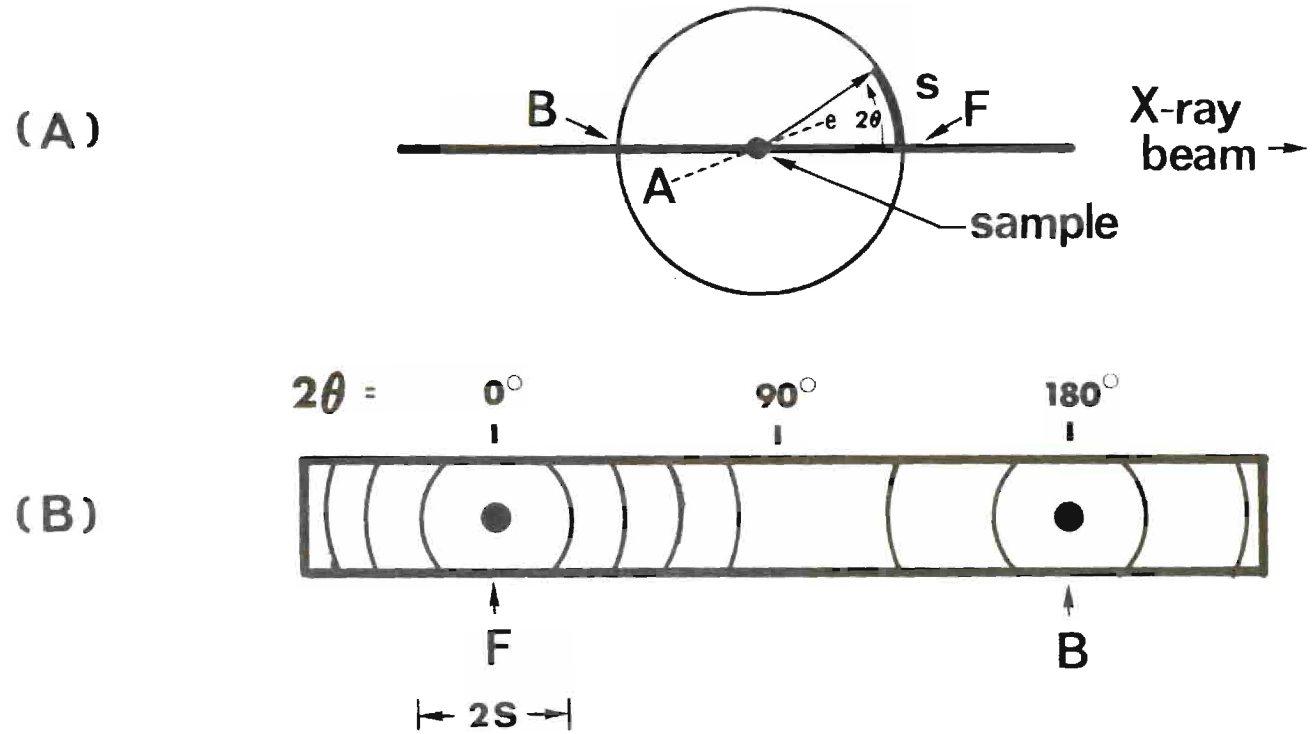

Figure 3. The Straumanis Film Mounting in the Debye-Scherrer Powder Camera

$$2\theta = \left(\frac{180}{FB}\right)S \qquad \text{(II-4)}$$

was applied. In measuring the arc positions, both edges of the arc were measured and the midpoint was taken as the arc position. The measured angles, 2θ, were then converted to d spacings using Equation (II-2), and the d spacings were converted into lattice spacings, by using the relationship for the relative spacings of cubic planes, *viz.*

$$d_{hk\ell} = \frac{a}{(h^2+k^2+\ell^2)^{\frac{1}{2}}} \qquad \text{(II-5)}$$

where $d_{hk\ell}$ is the spacing between successive planes with the Miller indexes ($hk\ell$).

All X-ray diffraction powder patterns were corrected for the refraction of X-rays as described by Taylor and Sinclair (31), and for the film shrinkage effects described. Analysis of the X-ray diffraction powder patterns yields a lattice parameter of 4.3268±0.0006Å for TiC-8. This uncertainty of ±0.0006Å is based upon the uncertainty involved in measuring the position of the diffraction arcs on the film using the Starrett vernier.

Results and Discussion of X-Ray Data

In Table 1 are listed lattice constants for five TiC samples as well as values for a commercial sample (Shieldalloy, SC Grade, 2) and two high purity samples evaluated in the literature (27,28). Two samples (TiC-4 and TiC-6) which were made from starting mixtures

Table 1. Crystal Lattice Constants for TiC

Sample	% Carbon in Reaction Mixture	Lattice Constant $\overset{o}{(A)}$
TiC-4	20.0	4.2816±.0006
TiC-6	20.0	4.2923±.0006
TiC-8	19.5	4.3268±.0006
TiC-9	19.5	4.3240±.0006
TiC-10	19.5	4.3238±.0006
Shieldalloy	20.2[a]	4.328 ±.001
Bleecker (27)	19.5	4.3275
Storms (28)	-	4.3280

[a]Represents total of combined and free carbon in the final product.

containing 20.0% carbon had lattice constants slightly lower than those produced from mixtures containing 19.5% carbon, and it is not known whether this is due to contamination of these particular samples by small amounts of O and N or to some other difference in the resultant carbides. For TiC-4 and TiC-6 it was possible to detect the (002) diffraction line for graphite, indicating the presence of uncombined graphitized carbon. The (002) diffraction line of graphite was not detected in the Shieldalloy sample even though the supplier stated in his specifications that it contains 0.4wt% free carbon. It may be concluded that the amount of free carbon is either too small to detect by X-ray diffraction or alternatively that the carbon is present primarily in a non-graphitic form. The lattice constant for TiC-8 agrees particularly well with the accepted literature values for stoichiometric TiC. Furthermore, all the lines in its spectrum (Figure 4c) may be identified with planes of a NaCℓ structure. Because the lattice constant for TiC-8 was in better agreement with the value of Bleecker (27) and Storms (28) than any of the other samples synthesized, it was chosen for all subsequent measurements. In Figure 4 spectrum A corresponds to pure Sterling FT graphitized carbon, one of the starting materials in the synthesis, and is typical of graphitic carbons which have both oriented and disoriented graphite layer planes (32). Spectrum B is of the reaction mixture of TiC-8 after it is removed from the ball mill, and spectrum C is of TiC-8. As previously mentioned, all the lines of the TiC-8 pattern can be identified in terms of planes in the NaCℓ structure. Notice particularly the

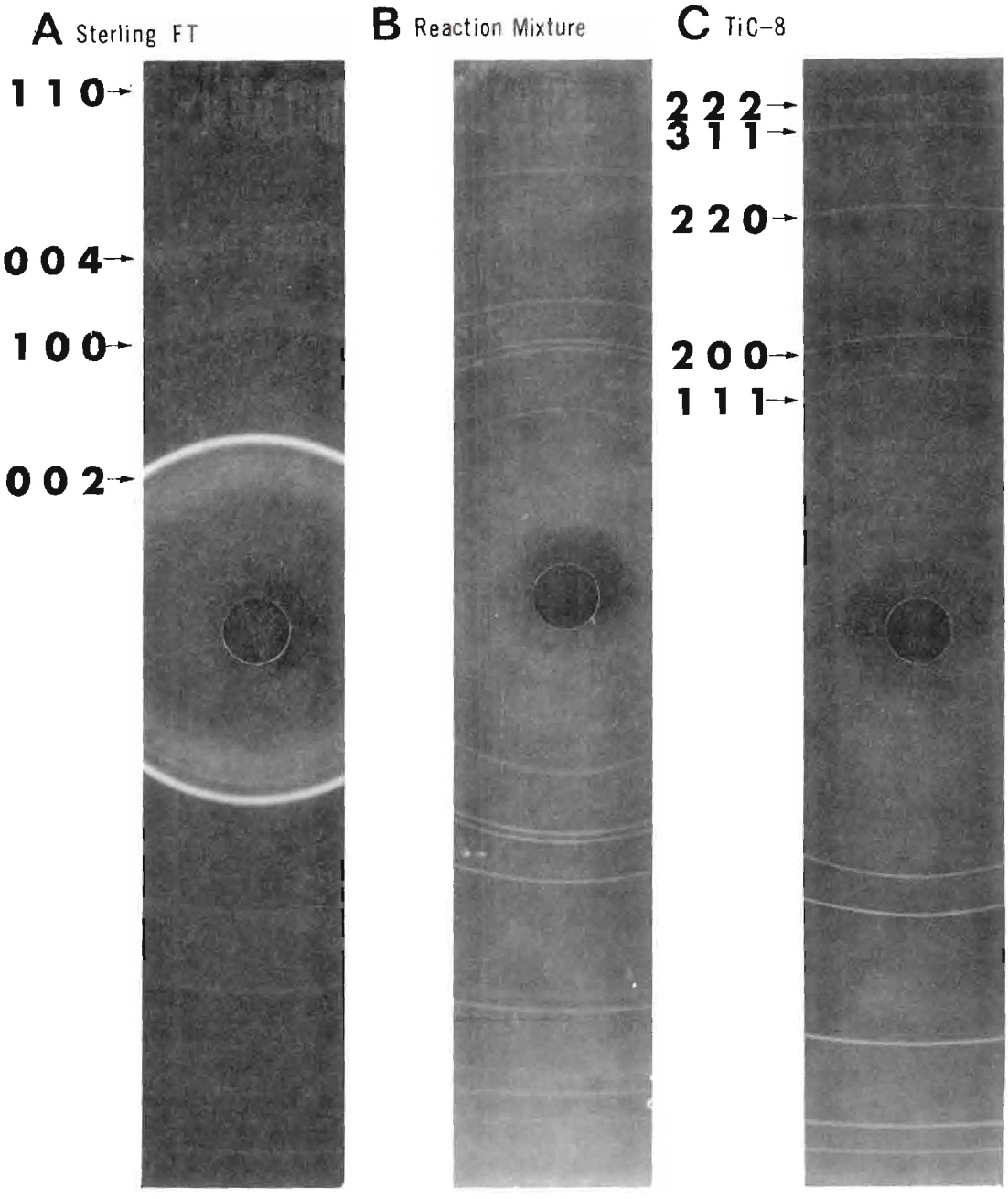

Figure 4. X-Ray Diffraction Powder Patterns

apparent absence of lines that might be attributable to uncombined carbon or titanium metal. Impurities incorporated into the TiC-8 lattice amounting to more than a few mole percentage would certainly be detected since their presence would cause measurable changes in the lattice constant. An exception to this statement might occur if the presence of different types of impurities having opposing effects on the lattice constant produced no net change in that parameter.

Electron Diffraction

In order to establish that a small group of polyhedral particles was in fact crystalline TiC having the correct lattice constant, an electron diffraction pattern was made in conjunction with the electron microscopy experiments described previously. Although electron diffraction cannot determine the lattice parameter with as high an accuracy as X-ray diffraction, it does possess the distinct advantage of allowing selection of a very small part of a sample for study. In an electron microscope there exists the capability of using a selector aperture to choose an area of the total sample for study. If the selector aperture encompasses a large number of randomly-oriented crystallites, then Debye-Scherrer ring patterns will be obtained analogous to the X-ray powder diffraction patterns discussed earlier. If a small group of particles is chosen, then the observed diffraction patterns are made up of "spotty" rings since there are no longer a sufficient number of randomly-oriented crystallites present to create a continuous diffraction cone. If a single crystal were present in the electron beam, it would produce a symmetrical arrangement of spots, each of which has a

different value of h, k, and ℓ. Spots which lie at an equal distance from the center and which are diametrically opposed are indexed as hkℓ and $\bar{h}\bar{k}\bar{\ell}$.

The electron diffraction patterns obtained are solved by relating distances on the pattern to distances and angles in the crystal lattice. From geometry (33)

$$\frac{D/2}{L} = \tan 2\theta, \qquad \text{(II-6)}$$

where D is the ring diameter, D/2 is the distance of a spot to the center of the pattern, L is the effective camera length and θ is the diffraction angle. The angle θ is very small (usually less than 3°) so we can assume

$$\tan 2\theta \simeq 2\sin\theta. \qquad \text{(II-7)}$$

Using the Bragg equation to eliminate θ gives

$$D = 2L\,\frac{\lambda}{d} \qquad \text{(II-8)}$$

where λ and d have been defined previously, or

$$\frac{D \cdot d}{2} = L\lambda = \text{Camera Constant} \qquad \text{(II-9)}$$

In practice $2L\lambda$ is used as the camera constant since the diameters of rings are measured, or distances between diametrically opposed spots.

All electron diffraction work was done on a Phillips EM-200 electron microscope using a beam current of 80kv. A diffraction pattern of vapor deposited TlCl was photographed using identical instrument settings to provide a standard for evaluating the camera constant. Vapor deposited TlCl was chosen for the reference because it gives a large number of very sharp rings, whose corresponding d spacings are well known. Since facilities necessary for measuring the small distances involved on the original negative of the diffraction pattern were not available, it was necessary to resort to a series of photographic enlargements made by the Engineering Experiment Station. A series of 8 inch by 8 inch enlargements were needed to plainly reveal all the details of the diffraction pattern. The standard pattern was treated in an identical manner and great care was taken to insure that the plane of the negative remained parallel to the plane of the enlarging paper so that there would be no distortion in the enlargement of the diffraction pattern.

To index the TlCl pattern the following procedure was used. First, the lattice parameter and d spacing values for TlCl were obtained (34), then the d spacings of three lines of known intensities were obtained from the ASTM Fink Index (35). Three lines on the photo enlargements were then chosen to correspond to those lines and a plot of d spacing as a function of distance on the enlargement was made.

To insure that the proper lines were chosen as the reference lines, the d spacings for the remaining TlCℓ lines were calculated and compared with the known values of d spacings. When the TlCℓ pattern was fully indexed, the ring diameter and spot diameters for the TiC-8 were measured and the resultant d spacings calculated. A blank grid pattern was also obtained so that the lines due to an empty grid could be distinguished. The five rings of the pattern (Figure 5) are identified with the following reflections: blank grid, unidentified; TiC (200); blank grid, unidentified; TiC (222); blank grid, unidentified. Barely visible in Figure 5 are some spots which are due to the (111) and (220) planes of TiC. Not visible in Figure 5, but plainly showing in the enlargements are spots due to the (311) and a ring due to the (400) planes of TiC. Calculation of the lattice constant based on the d spacings obtained yield a value for the lattice of 4.32±0.03Å which agrees with the X-ray value to within experimental error. The uncertainty of ±0.03Å is again attributed to the uncertainty involved in measuring the diffraction rings (and spots).

Electron Microscopy

After synthesizing TiC-8, preliminary micrographs taken on a Joelco Model JEM-50-B electron microscope proved that this material was composed of particles essentially identical in their morphology to the graphitized carbon in the reaction mixture. More extensive studies on a Phillips EM-200 electron microscope were then undertaken. Examples of representative micrographs of Sterling FT and TiC-8 taken on this instrument are shown in Figure 6. Several different types of polyhedra

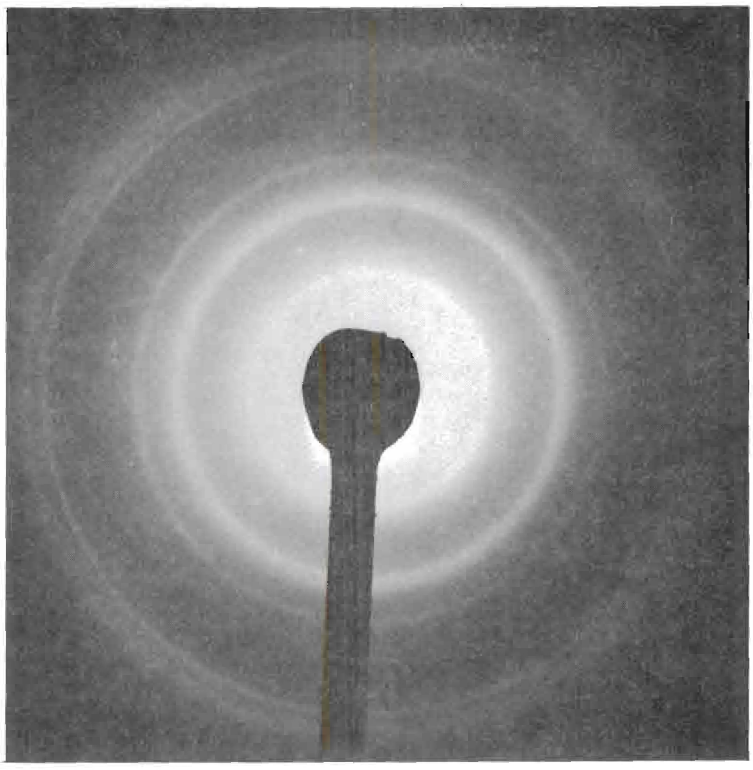

Figure 5. Electron Diffraction Pattern for TiC-8

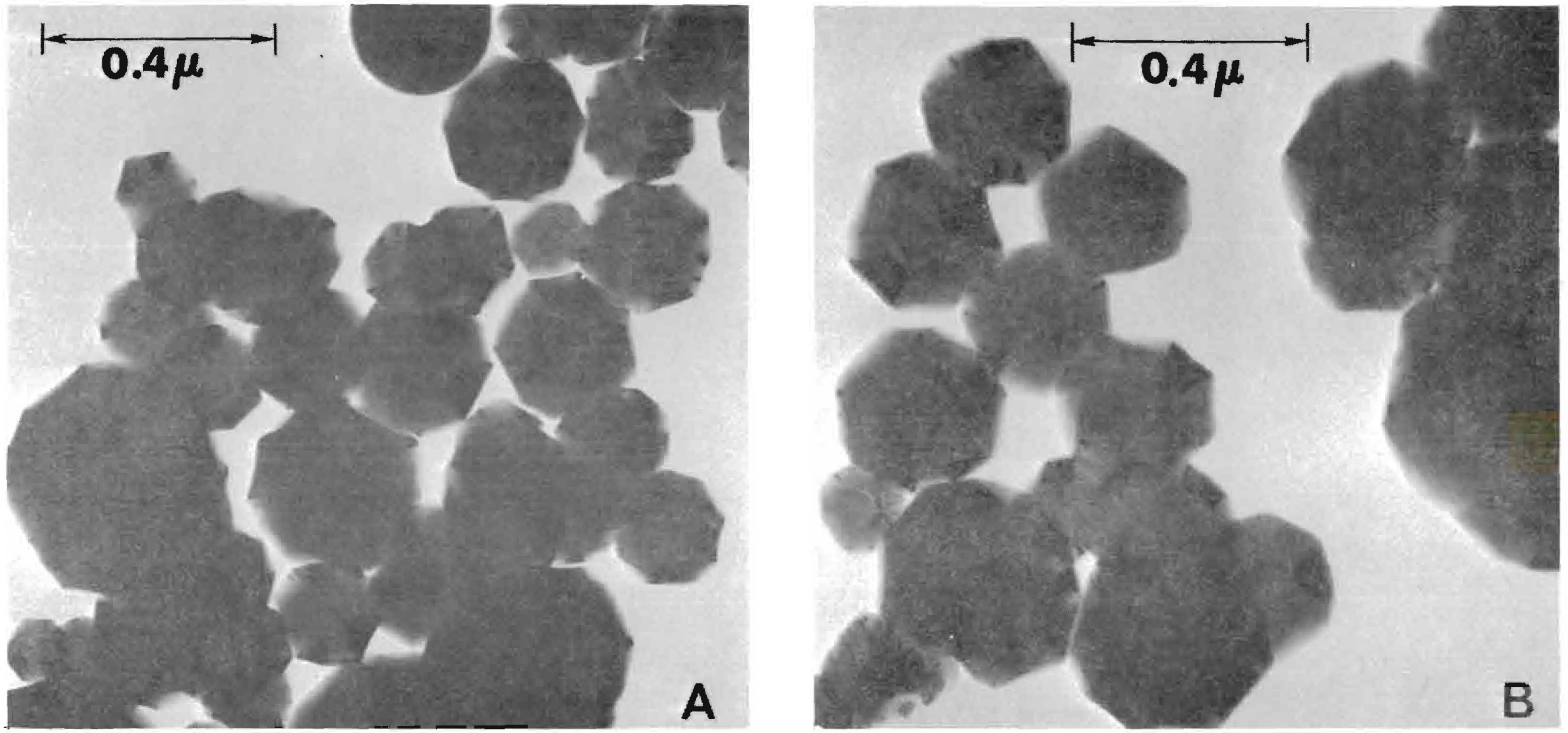

Figure 6. Transmission Electron Micrograph of Sterling FT and TiC-8

are seen in these samples. Mostly there are irregular, doubly truncated, hexagonal and octagonal bipyramids. In addition there are other irregular polyhedra among which are seen a fair number of twinned particles. No systematic differences in particle geometry between TiC-8 and Sterling FT were obvious.

The geometrical features of TiC-8 are confirmed from a micrograph (Figure 7) taken on a Cambridge Stereoscan Mark II scanning electron microscope. Although the resolution (~200Å) is much below that of a transmission microscope, the scanning picture does provide a more realistic perspective of the particles. It is obvious from this micrograph that most of the TiC-8 particles are roughly "spherical" and are primarily irregular polyhedra of different types.

From sets of transmission micrographs for Sterling FT and TiC-8 particle size analyses were carried out (36). Particles were either measured directly from photographic enlargements or from the screen of a table-top slide projector which magnified the micrographs by a known amount. For each particle the maximum distance across was measured and designated *a*. The perpendicular bisector of *a* was then measured and designated *b*. The two dimensions did not differ much for a given particle except in the case of a twinned particle. Assuming spherical particles, the surface area per unit volume, S', for a system of N particles is given by

$$S' = 6 \sum_{i=1}^{N} d_i^2 / \sum_{i=1}^{N} d_i^3 \qquad \text{(II-10)}$$

where d_i is the diameter of the *ith* particle.

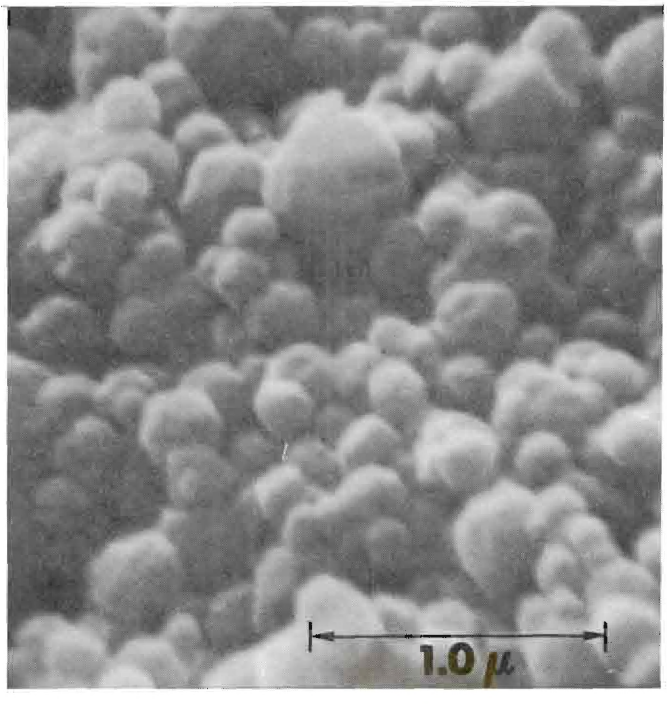

Figure 7. Scanning Electron Micrograph of TiC-8

In order to estimate an effective spherical diameter, d_i, a particle diameter was defined by the geometric mean relation

$$d_i = (a_i b_i)^{\frac{1}{2}}. \qquad \text{(II-11)}$$

This assumption is reasonable if $a_i \simeq b_i$, *i.e.* if the particles are nearly spherical. Application of the above method to the micrographs gives S' equal to 26.5 m^2/cc (using measurements of 109 particles) for Sterling FT and 21.8 m^2/cc (using 305 particles) for TiC-8. Clearly, the average particle size of TiC-8 is larger than that for Sterling FT and since there are no obvious differences in the particle morphology of the two materials, it is conjectured that Sterling FT particles remain virtually intact as they react with Ti metal to form TiC. If this is correct, it should be possible to calculate the increase in average particle size just on the basis of the change in molar volume on going from graphitized carbon to TiC. The ratio of the surface areas per unit volume on this basis, is simply

$$S'_{FT}/S'_{TiC} = (\bar{V}_{TiC}/\bar{V}_{FT})^{1/3}, \qquad \text{(II-12)}$$

if the particles are assumed to be spheres. Using $\bar{V}_{TiC}$ = 12.20 cc/mole and $\bar{V}_{FT}$ = 5.46 cc/mole, we find that the ratio is 1.31. The electron microscopy values give a value of 1.22 for this ratio. Since an error of the order of 10% would be expected in the electron microscopy ratio, it may be said that the two calculations agree to within experimental

error. This evidence together with the apparent absence of change in particle geometry tends to confirm the conjecture of a one-to-one correspondence between graphitized carbon particles and TiC particles.

X-Ray Emission Electron Microprobe Analysis

In order to obtain quantitative estimates of impurities both in the starting materials and in TiC-8, measurements were carried out with an electron probe X-ray microanalyzer (Acton Laboratories, Model MS64).* Since this analytical method is a relative one, standards were chosen to determine absolute amounts of impurities. Analyses for certain trace elements in the Shieldalloy TiC and the Ventron Ti metal had already been carried out by the suppliers. The limits of precision on these standards are not known, but they are probably not seriously in error. The relative amounts of impurity are undoubtedly of higher precision than the absolute values. Results of the microprobe analysis are given in Table 2. There were no appreciable amounts of trace elements in TiC-8 other than those shown. This implies that the total impurity content amounts to about 1.2wt%. The reaction mixture for TiC-8 contained very nearly the same amounts of impurities as the final product. This proves that no additional impurities were introduced during synthesis. The low silicon content of the reaction mixture establishes the fact that there was little or no borosilicate contamination introduced by milling with Pyrex balls. Furthermore, since the Si content of the final product is virtually identical to the reaction mixture,

---

*These measurements were performed by the staff of the Engineering Experiment Station at The Georgia Institute of Technology.

transport of SiO_2 from the quartz reaction tube to the sample during synthesis must have been negligible. The oxygen content was somewhat higher than expected, but since there is about the same amount of oxygen in the reaction mixture, it is likely that it was simply retained and incorporated into the TiC lattice during synthesis.

Table 2. X-Ray Emission Electron Microprobe Analysis of Impurities

Sample	Weight Per Cent Impurity					
	O	N	Aℓ	Si	Fe	W
Ventron Ti Metal	0.15	0.05	0.87[a]	0.03[a]	0.01	b
TiC-8 Reaction Mixture, After Ball Milling	0.46	0.06	0.89	0.07	0.01	b
TiC-8	0.41	0.08	0.61	0.05	b	b
Shieldalloy	0.10[a]	0.05[a]	0.79	0.06	0.05[a]	0.03

[a]Taken as standard.

[b]Below limit of detection, i.e. less than 0.005%.

Besides the results given in Table 2, it was also possible (using X-ray emission electron microprobe techniques) to compare the C/Ti ratio of TiC-8 with that of the Shieldalloy TiC. Results showed that the C/Ti ratio for TiC-8 is slightly higher than that of the Shieldalloy sample. Since the supplier's analysis for the latter gives C/Ti = 0.97, it may be concluded that TiC-8 is stoichiometric to within about 2%.

CHAPTER III

EXPERIMENTAL EQUIPMENT AND PROCEDURES

The Adsorption System

The all-glass volumetric adsorption system used to study the physical adsorption of gases on titanium carbide is shown schematically in Figure 8 and in Figure 9. The system consists of two sides. The side shown in Figure 8, Side 1, is used for measuring physical adsorption of gases in the pressure range from 50 to 500 torr using a mercury manometer, MAN 1, for pressure measurement. Side 1 is not designed to make measurements on gases which are soluble in stopcock grease. The side shown in Figure 9, Side 2, is used to measure the physical adsorption of gases in the range of 2×10^{-5} to 50 torr using a McLeod gauge for pressure measurement, and exposes no stopcocks to the adsorbate dose. Thus, through the extensive use of mercury cut-offs to replace stopcocks, gases which are soluble in stopcock grease may be studied. In the measurements on TiC-8, Side 1 was used to study the adsorption of Ar and N_2 at 77° and Side 2 was used to study Ar at 77 and 90°K, CH_4 at 77°K and C_6H_6 in the range of 251 to 273°K. The main pumping system consists of a two-stage mercury diffusion pump, separated from the main manifold by a slush bath of crushed dry-ice and acetone, and a Model 1400 Welch Duo-Seal roughing pump. This arrangement is capable of reducing the pressure in the system to below 10^{-6} torr.

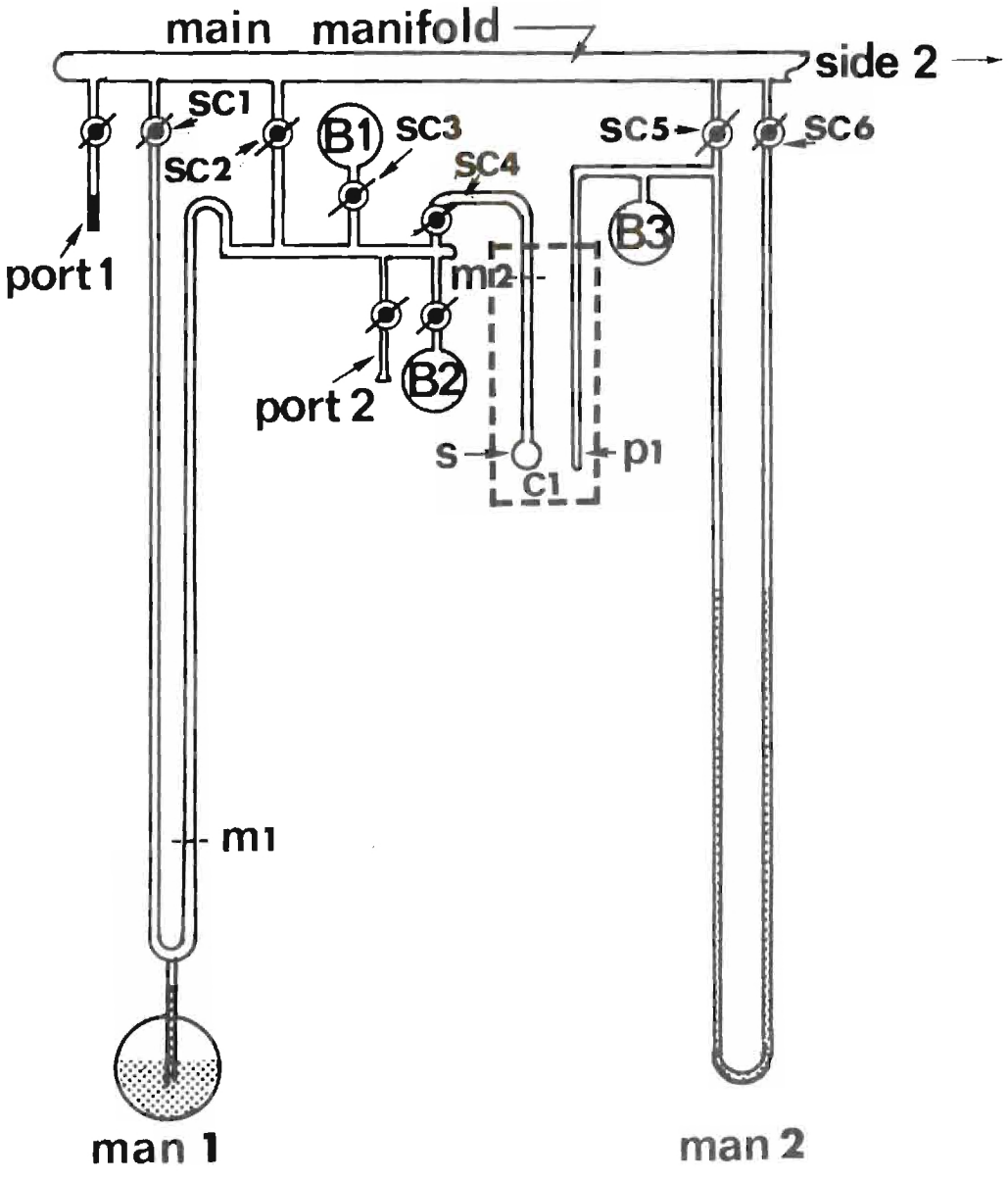

Figure 8. The High Pressure Side, Side 1

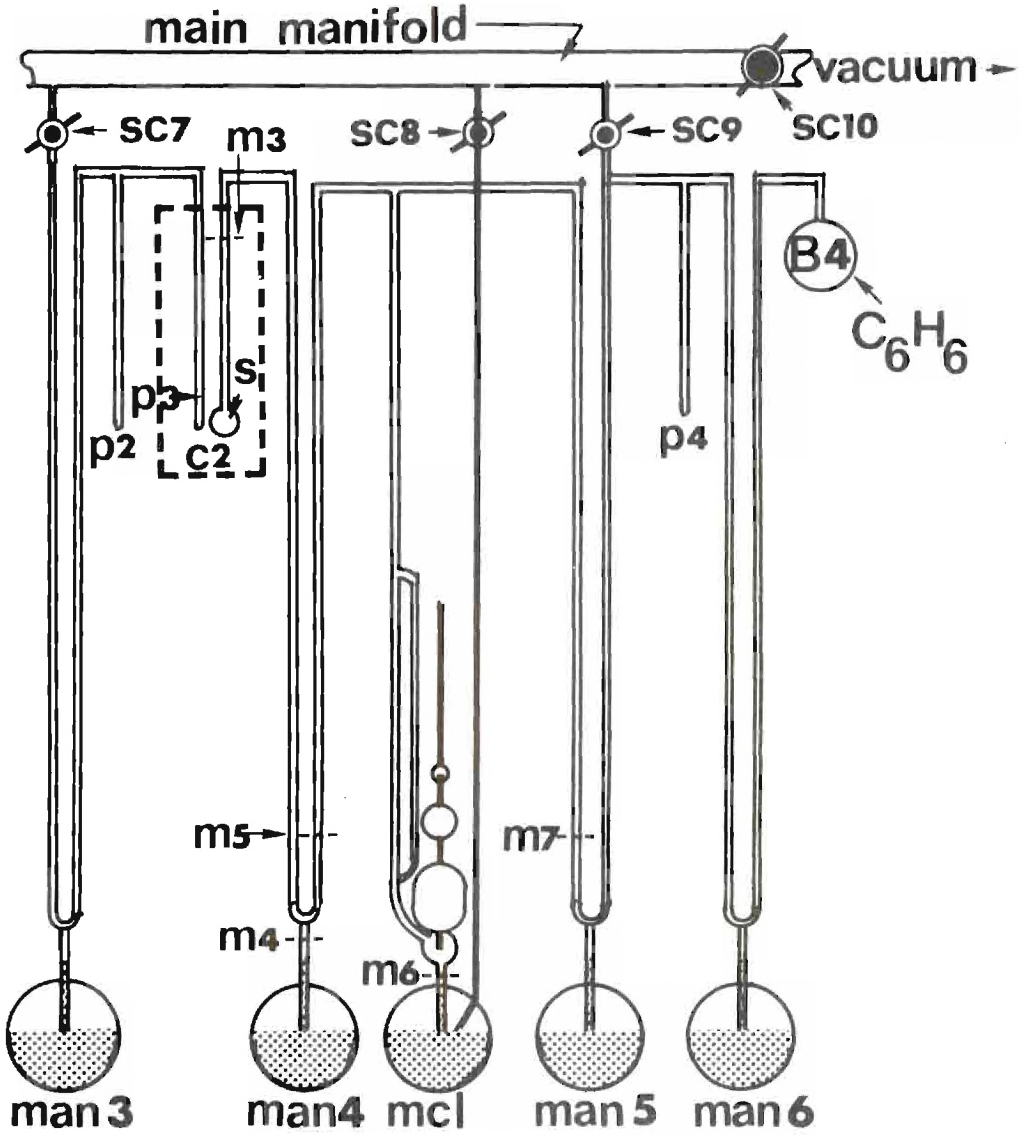

Figure 9. The Low Pressure Side, Side 2

An additional pumping system utilizing a Precision Model 25 vacuum pump was used to operate the mercury cut-offs.

The McLeod Gauge

The McLeod gauge constructed for this study can measure pressures of 2×10^{-5} torr to 50 torr using five compression stages (Figure 10). By raising the mercury level using atmospheric pressure, the gas in volume V, the total volume of the McLeod gauge, is compressed. The pressure of the compressed gas is then equal to the difference in height of the mercury column in the closed-off section and the mercury height in the reference tube. The pressure of the gas in the system can then be found by using the measured pressure of the gas in the McLeod gauge combined with a suitable equation of state for the gas. For helium, argon, and methane the ideal gas law was used as the equation of state.

As a correction for the non-deality of benzene vapor, the virial equation was used as an equation of state for the vapor in the McLeod gauge. The virial equation was truncated after the third term, *viz.*

$$P_1V_1 = n_1RT + n_1B(T)P_1 + n_1C(T)\frac{(P_1)^2}{RT} \qquad \text{(III-1)}$$

where P_1 equals the pressure in the system and V_1 is the volume of the entire McLeod gauge. Of course there is an identical expression for P_2V_2, the product of the pressure inside the McLeod gauge and the compression volume. Realizing that at all times $P_2 >> P_1$ and if $P_1 << 1$ we can write

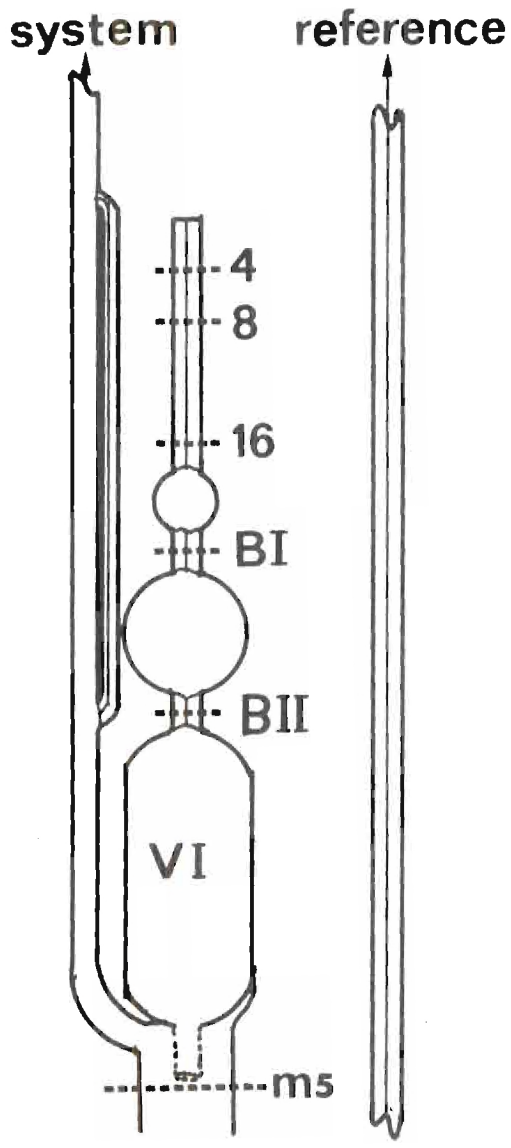

Figure 10. The McLeod Gauge

$$P_1 = \frac{V_2}{V_1} P_2 \left\{ \frac{1}{1 + B(T)\left(\frac{P_2}{RT}\right) + C(T)\left(\frac{P_2}{RT}\right)^2} \right\} \qquad \text{(III-2)}$$

where of course $\frac{V_2}{V_1}$ is a constant for each level of the gauge.

The second virial coefficient, B(T), and the third virial coefficient, C(T), were used in correcting pressures of benzene vapor read in the McLeod gauge. The procedure used in this calculation was that outlined by Eggers, Gregory, Halsey and Rabinovitch (37). The value of B(T) was found by use of the relationship

$$B(T) = b_o B^*(T^*) \qquad \text{(III-3)}$$

where

$$b_o = \frac{2}{3} \pi N \sigma^3, \qquad \text{(III-4)}$$

where N is Avogadro's number and

σ = the interatomic distance at which the potential energy given by the Lennard-Jones (6-12) potential is zero.

T^* = a reduced temperature which can be calculated from the equation

$$T^* = kT/\epsilon^* \qquad \text{(III-5)}$$

where ϵ^*/k is the depth of the minimum in the potential energy curve for benzene.

Both σ and ϵ^*/k were taken from tables provided by Hirschfelder, Curtiss and Bird. The value used for σ was 5.270Å and the value used for ϵ^*/k was 440°K (38); both of these values were obtained by Hirschfelder *et al.* from gas viscosity data. Values of $B^*(T^*)$ were obtained from tables provided by Hirschfelder, Curtiss, and Bird.

To find the third virial coefficient, C(T), the following equation was used

$$C(T) = b_o^2 C^*(T^*) \qquad \text{(III-6)}$$

where

$$b_o = \frac{2}{3}\pi N\sigma^3 \qquad \text{(III-7)}$$

and T^* is defined by Equation (III-5). The value of $C^*(T^*)$ was also obtained from tables in Hirschfelder, Curtiss, and Bird (39).

Thermal Transpiration Corrections

Whenever a manometer or a McLeod gauge is being used to measure low pressures in a system where a thermal gradient exists, it is necessary to correct for thermal transpiration. Because of the thermal gradient, the gas tends to pass from the cooler to the warmer regions of the system and eventually sets up a pressure gradient in the system. Thus if the sample is colder than the McLeod gauge, the pressure measured on the gauge is greater than the pressure in the cold part of the system. At low pressures the magnitude of this discrepancy can become

very large (40). Weber (41) has developed a series of equations which can be used to correct measurements for thermal transpiration effects.

Miller (42) has proposed a useful approximate solution to Weber's equations which takes the form

$$\frac{dP}{dT}\left(\frac{2T}{P}\right) \simeq \frac{\Delta P}{\Delta T}\left(\frac{2T}{P}\right) \simeq \frac{1 - (P_1/P_2)}{1 - (T_1/T_2)} = x \qquad \text{(III-8)}$$

where

$$x = \frac{1}{\alpha y^2 + \beta y + \mu}; \qquad T_2 > T_1 \qquad \text{(III-9)}$$

and

$$y(P_1,T_1) > y > y(P_2,T_2) \qquad \text{(III-10)}$$

The equations have the correct limiting forms,

$$\lim_{y\to 0} (P_1/P_2) = (T_1/T_2)^{\frac{1}{2}} \qquad \text{(III-11)}$$

$$\lim_{y\to \infty} (P_2-P_1) = 0 \qquad \text{(III-12)}$$

The parameter y is calculated using the kinetic gas theory equation

$$P = kT/\pi(2)^{\frac{1}{2}}\sigma_T^2 \qquad \text{(III-13)}$$

where k is the Boltzmann constant and σ_T is the hard sphere diameter at temperature $T = (T_1+T_2)/2$.

In usual experimental conditions P_2, T_2 and T_1 are known and P_1 is to be calculated. In order to avoid dependence of y on P_1, the following choice is made

$$y = d/\lambda = P_2 d\pi(2)^{\frac{1}{2}}\sigma_T^2/kT \qquad \text{(III-14)}$$

$$y = (P_2 d\sigma_T^2/2.33T) \times 10^3 \qquad \text{(III-15)}$$

where P_2 is in torr, σ_T is in $\mathring{A}$, d is the inside diameter of the tube in millimeters and $T = (T_1+T_2)/2$.

Miller (42) has eliminated α, β and b from Equation III-9 and has found that the following general equation applies

$$x = \left(0.030y^2 + 0.245y + \frac{1 + 2.5y}{1 + 2y}\right)^{-1} \qquad \text{(III-16)}$$

To correct for thermal transpiration, Equations (III-8), (III-15), and (III-16) due to Miller (42) were used. Values of σ_T for the gases studied were obtained from

$$\sigma_T^2 = \sigma_\infty^2(1+C/T) \qquad \text{(III-17)}$$

where σ_∞ and C are constants given by Landolt-Bornstein (43). The values used were (43):

Adsorbate	σ_∞ (Å)	C
N_2	3.22	105
Ar	2.99	142
CH_4	3.33	162
C_6H_6	4.71	448

Construction and Calibration of the McLeod Gauge and Bulb B1

The McLeod gauge was designed to measure pressures in the range of 2×10^{-5} torr to 50 torr and was constructed especially for this study.

The total volume selected for the gauge was 150 ml, the compression volumes necessary for five overlapping stages were calculated using the ideal gas law. Next, lengths of uniform capillary tubing were chosen for use in the McLeod gauge and as reference capillaries. The capillary tubing was calibrated by measuring the length (about 10-12 cm) of a mercury column as it was moved horizontally along the capillary tubing. By recording the column length in pre-marked sections of the capillary tubing and then weighing the column, the cross sectional area of the capillary could be calculated. Capillary tubing finally used used was chosen for uniformity of cross section along its entire length. The diameter of the capillary tubing used in both the McLeod gauge and in the system side reference arm was 2.135±0.001 mm, and that of the vacuum reference side 2.151±0.001 mm. The McLeod gauge

was constructed in two parts: part A which contained all the compression stages, BI, BII, 16, 8, 4, and part B which contained the remainder of the gauge. Part A was calibrated first, and then parts A and B were joined and the total volume was calibrated. Part A was calibrated by filling it to the various stages with mercury and then weighing it on a kilogram Mettler balance. Five separate calibrations were carried out, and between calibrations the capillary was washed consecutively with nitric acid, cleaning solution, and distilled water, and then dried. All weighing measurements were corrected for buoyancy (the displacement of air by mercury) as described by Jasper (44). The temperature of the mercury was measured on an ASTM thermometer to ±0.005°C; the variation in the temperature of the mercury during calibration was typically ±0.050°C. The volumes obtained are listed in Table 3. When Part A and Part B of the McLeod gauge were joined, volume VI was determined. The McLeod gauge was supported upside down and filled with mercury. The mercury was then withdrawn down to the BII level in aliquots and weighed on the kilogram Mettler balance. The gauge was then emptied and cleaned as described before; the data were treated as described before, and the result of five separate runs is given in Table 3.

Table 3. McLeod Gauge and BI Volumes

Stage	Volume (ml)
4	0.1441 ± 0.0003*
8	0.2836 ± 0.0003
16	0.5706 ± 0.0004
BI	6.0286 ± 0.0005
BII	16.7001 ± 0.0008
VI	140.80 ± 0.02
V_{TOT}	157.50
Bulb	
BI	127.76 ± 0.01

*Average deviations.

The total volume of the McLeod gauge was used as a standard when calibrating the volume of the low pressure side (Figure 9) as will be described later. In order to calibrate the volume of the high pressure side (Figure 8), Bulb B1 was employed. The volume of the bulb B1 (Figure 8) was accurately calibrated using mercury. The procedure was identical to that already described for volume VI of the McLeod gauge. The entire volume of B1 (including the bore of the stopcock SC3) was filled with mercury and then removed by aliquots. The volume found in three calibration runs is also given in Table 3. Before benzene adsorption measurements were made, precise determinations of the

capillary correction were made using a Gaertner (No. 2163A) Cathetometer. To make capillary corrections, the McLeod gauge and reference capillary were thoroughly evacuated to the ultimate limit of the pumping apparatus (below 10^{-6} torr). To implement this, prolonged pumping was combined with the use of a Tesla coil to remove any adsorbed gases or water vapor off the walls of the system. To determine that a pressure less than 10^{-6} torr had been reached, Side 2 was sealed off from the pumping system at SC9 and the pressure was allowed to build up for about two hours with intermittent sparking. When a measurable pressure failed to build up after this time, the system was considered to be thoroughly outgassed. The mercury was then raised to each level of the McLeod gauge and the difference in height of the column in the McLeod gauge and in the vacuum reference side was measured. These differences in height are corrections which must be applied to the measured height of the mercury column and are due to variations in the cross-sectional area of the capillary tubing. The values of the capillary corrections which are an average over four determinations are given in Table 4.

Table 4. Capillary Corrections

Stage	Capillary Correction (mm)
4	+0.86 ± .03*
8	+0.55 ± .03
16	-0.09 ± .03
BI	-0.30 ± .03
BII	-0.49 ± .03

*Average deviations.

Materials

The benzene used for adsorption studies on TiC-8 was triply distilled into the benzene storage bulb shown in Figure 2, from a flask fitted with a KOVAR seal and attached to the KOVAR seal entrance port (shown in Figure 8) by means of a SWAGELOK coupler. The flask used to hold the benzene for distillation had a volume of about 250 ml, and prior to filling with benzene it was filled about 1/3 full of Davison Molecular Sieves (Type 5A Grade 522, 8-12 mesh, Beads, 5Å pore size, Fisher No. M-522 Lot 703511). The flask was then placed in a drying oven at 100°C for two days, and then capped off with a SWAGELOK coupler and a KOVAR seal with a 4mm HV stopcock and a ♀ 10/30 joint. The flask was then attached at PORT 2 (Figure 8) and evacuated, to remove any residual air trapped in the sieves. The flask was also preheated with a heat gun as an added precaution against the entrapment of any moisture. The flask was then filled with an atmosphere of helium and its stopcock was closed. The flask was then transferred to a plastic bag flushed with tank grade helium, the flask filled with benzene (Fisher Certified ACS Spectranalyzed No. B-411, Lot No. 704706) and then sealed with a KOVAR seal with a capped end. The flask was allowed to stand for eight days, and was periodically agitated. The bulb was then placed on the system and gently pumped to remove any helium or dissolved air. A large Dewar was placed around the supply flask and filled with crushed ice. The benzene was allowed to freeze overnight, and then was pumped for about an hour. Subsequently the stopcock on PORT 1 was closed and the system evacuated. Bulb B2 was

then surrounded by liquid nitrogen and after the main stopcock SC10 was closed, PORT 1 was opened to the system. Benzene was allowed to distill into B2 for eight hours; then PORT 1 was closed and SC10 opened to pump on B2. Pumping was continued until about 1/4 of the material in B2 was gone and then SC10 was closed. Bulb B4 was then surrounded by liquid nitrogen and about 1/2 of the original amount of benzene in B2 was transferred to B4. Bulb B4 was then isolated from the system and the remaining benzene in B2 was pumped away. This entire distillation procedure was repeated twice, and about 50 ml of benzene was accumulated in B4. Bulb B4 was covered with aluminum foil and placed under water in a covered Dewar. The presence of any dissolved gases was checked in two ways. First the vapor pressure of the liquid benzene at the temperature of the water surrounding bulb B4 was calculated using the Antoine equation (see Appendix A) and this value was compared to that measured on manometer MAN6 using a Gaertner (No. 2163A) cathetometer. The measured vapor pressure agreed with the calculated value to within the resolution of the cathetometer, ±.025 mm. A second and more sensitive test is to fill the volume between SC9 and mark M4 with benzene to its equilibrium vapor pressure at room temperature (about 100 torr) and then after raising MAN6 to close off the benzene storage bulb, placing a liquid nitrogen bath around probe P4, and allowing the system to come to equilibrium. The vapor pressure of benzene at liquid nitrogen pressure is vanishingly small (on the order of 10^{-30} torr) so any residual pressure is due to gases dissolved in the benzene. When this procedure was followed, the pressure dropped to a level below the limit of the McLeod gauge.

All of the gases used in this study were supplied by Matheson in lecture bottle sizes, and were connected to the KOVAR seal at PORT 1. The helium used for calibration was Matheson "High Purity" and was used without further purification. The carbon dioxide used to measure dry-ice temperature was Matheson "Bone Dry" and was distilled once before filling MAN2. The nitrogen used both as an adsorbate and in manometer MAN2 to measure the temperature of the liquid nitrogen was Matheson "Extra Dry." The oxygen used to measure the temperature of the liquid oxygen bath was also Matheson lecture bottle grade oxygen. The argon used as an adsorbate was Matheson "Extra High Purity" and was used as received. The methane used as an adsorbate was Matheson lecture bottle grade and was distilled once *in vacuo* before use.

To measure temperatures in the range of 251-273°K manometer MAN3 was filled with 2-methylbutane. A sample of 2-methylbutane was dried with heat-activated molecular sieves as was the benzene; after MAN3 had been thoroughly outgassed, it was filled with helium through SC7 and then an orifice was opened in probe P3 and about 3-5 ml of 2-methylbutane added and the orifice sealed with TORR-SEAL epoxy. After the epoxy had cured, MAN3 was gently evacuated while the 2-methylbutane was frozen at liquid nitrogen temperature in probe P3. After pumping on the 2-methylbutane to remove any dissolved gases, SC7 was closed and P3 was allowed to warm up. When the cryostat was positioned at C2, a series of measurement were made of the vapor pressure of 2-methylbutane over the temperature range of 251°K to 273°K. The vapor pressures were read using a Gaertner (No. 2163A) cathetometer and were converted to

temperatures using the Antoine equation (Appendix A) and these temperatures were compared to those read using a platinum resistance thermometer (Leeds and Northrup No. 1655162) and Mueller Bridge (Leeds and Northrup). The temperature given by the Antoine equation was found to be within the ±0.002°C error limit of the platinum resistance thermometer. In all manometer readings the heights of the mercury columns were corrected as described in Appendix A.

The mercury used in all volume calibrations and in all manometers, mercury cut-offs and the McLeod gauge was triply-distilled mercury taken from previously unopened bottles and was filtered before use.

The Adsorption System for Studying Benzene on TiC-8

Adsorption studies of benzene on TiC-8 required the low pressure adsorption system whose final configuration is shown in Figure 9. After the system was assembled, leak tested and thoroughly outgassed, bulb B4 was charged with benzene as previously described, and manometer MAN3 was charged with 2-methylbutane.

Temperature measurement was divided into three major categories:

1. Measurement of cryostat temperature (i.e. isotherm temperature).
2. Detection of fluctuations in cryostat temperature.
3. Measurement of room temperature.

The cryostat temperature was determined by measuring the vapor pressure of 2-methylbutane on manometer MAN3 (Figure 9) using a Gaertner (No. 2163A) cathetometer and converting the measured vapor pressure to temperature as described previously.

The cryostat temperature was continuously monitored on a thermistor bridge which was used as a null instrument. The thermistor bridge was constructed by the Instrument Shop of the School of Chemistry and incorporated a Yellow Springs Industries No. 44203 thermistor network as the temperature probe. The null meter was calibrated in divisions of 0.01°C, and the fluctuations observed were on this order of magnitude, although the cryostat occasionally had to be corrected for a drift problem.

Room temperatures were measured on two thermometers placed on MAN3 and MAN5. The thermometers were graduated to 0.01°C.

The Cryostat

The cryostat was designed for studies of benzene adsorption in the range of 251°K to 271°K. It employed two separate principles of temperature control. A thermoelectric cold plate was set so that the cryostat temperature would slowly drift below the desired control temperature. The heating coil on a copper block inside the cryostat was adjusted so that the downward drifting tendency was just balanced. The temperature was thus regulated by varying the current supplied to to the copper block heater.

The arrangement of the cryostat components are shown in Figure 11. The aluminum can shown in Figure 11 was surrounded by a cylindrical Dewar especially constructed for this cryostat by the Glassblowing Laboratory of the School of Chemistry. The cryostat was housed in a styrofoam container which was covered with heavy aluminum foil to minimize radiative heat transfer.

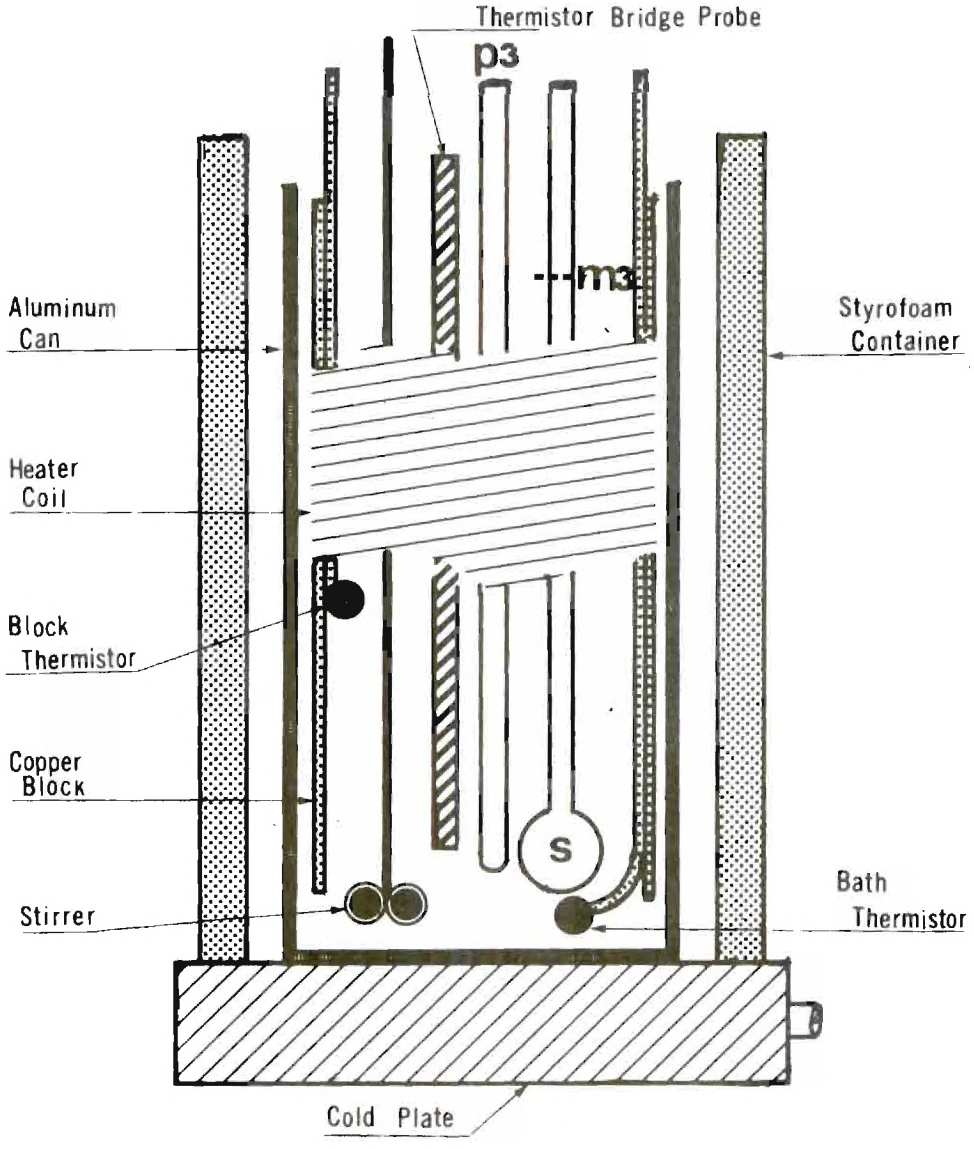

Figure 11. The Cryostat

The aluminum can was assembled by brazing a 4 inch by 4 inch by 3/8 inch aluminum plate onto a 9-1/2 inch length of aluminum pipe of 3-1/4 inch O.D. and 3 inch I.D. The O.D. was then machined down to 3-1/8 inch and the bottom plate was machined to 3-1/2 inch diameter. A 2 inch by 5/16 inch well was machined into the bottom of the can to fit the thermoelectric cold plate. This portion of the cryostat was built in conjunction with R. A. Magee (45). The thermoelectric cold plate is a Model CP-2 supplied by Thermoelectrics Unlimited. The cold plate power supply was constructed by the Instrument Shop of the School of Chemistry and is capable of delivering variable direct current of zero to eight amperes at zero to six volts with less than 5% ripple. The cold plate heat exchanger was supplied with a continuous flow of 50% ethylene glycol solution at -2 to -4°C at a rate of two liters per minute. This apparatus was described previously by Magee (45).

The copper block was out of a 7 inch length of copper tubing of 2-1/4 inch O.D. and 2 inch I.D. Four supporting lugs were brazed onto the top of the block and two lengths of 1/8 inch I.D. copper tubing were brazed onto the inside wall of the block as shown in Figure 5. The entire block weighed 518 grams. The two lengths of 1/8 inch tubing were used to house Yellow Springs Industries No. 44018 thermistors. As shown in Figure 5, one thermistor was used to sense the bath temperature. The thermistors were sealed into the tubes with silicone rubber cement. The outside of the block was covered with a layer of Teflon tape and then the heater was wound with 29-1/4 ft of Cerro 28 ga. CHROMEL A Nichrome wire having a resistance of 4.10 ohms per foot.

The entire copper block assembly was hung from a Flexaframe support cage by nylon string attached to the four hanging lugs on the copper block. The block was positioned so that it did not touch the aluminum can. A high-speed stirrer was placed near the bottom of the aluminum can, and the can was filled up to mark M3 with a 50% ethylene glycol solution.

The copper block heater and associated thermistors were connected to a cryostat controller designed and built by the Instrument Shop of the School of Chemistry. The cryostat controller was equipped with direct reading temperature readouts of the block and sample temperatures, a heater control with coarse and fine adjustments for heater current, and was capable of both manual and regulated mode operation. The aluminum can also held the probe for the thermistor bridge which monitored temperature fluctuations, the vapor pressure thermometer probe, P3, and the sample bulb.

To operate the cryostat it was first necessary to circulate the chilled water through the heat exchanger of the thermoelectric cold plate. A voltage was then safely applied to the cold plate and the temperature of the bath, which was continually stirred, began to drop. The temperature drop was easily followed on the direct sample temperature readout on the cryostat controller. As the desired temperature was approached, the cold plate voltage was reduced to a level where the temperature was slowly drifting downward. The heater of the copper block was then adjusted using the coarse and fine heater controls on the cryostat controller. By a careful adjustment of the cold plate

voltage and the heater controls of the cryostat controller, temperature could be stabilized at any point in the useable range. When this was accomplished the cryostat controller was switched from manual to regulated mode, and the thermilinear bridge was nulled.

When in the regulate mode, the cryostat controller employed the block thermistor (Figure 11) to sense temperature changes in the block. As the temperature of the block fluctuated, the cryostat controller adjusted the heat output to the block heater in proportion to this temperature change.

Using this cryostat benzene adsorption was studied at 268.11°K, 263.01°K, 258.62°K and 251.73°K with an average deviation of ±0.02°K. Benzene adsorption was also studied at 273.35°K±0.02°K using a well-stirred ice bath as a cryostat.

Calibration of High Pressure Side and Calculation of Adsorption Isotherms

In order to determine an adsorption isotherm using a volumetric adsorption apparatus it is necessary to have values for all of the volumes involved. To determine these volumes, helium was stored in the calibrated volume B1 (refer to Figure 8) at a known pressure which was read on MAN1. The helium was expanded into an evacuated unknown volume and the final pressure was read. Use of the ideal gas law allowed determination of the unknown volume. Two quantities had to be determined: the manifold volume, V_M, and the effective dead space volume, V_{Deff}, which is a function of the temperature of the adsorption isotherm.

The manifold volume is the volume defined between mark M1 and stopcock SC4, with all other stopcocks (SC2, SC3, PORT2 and B2) closed. Volume V_M was calibrated by expanding helium which was stored in the calibrated bulb B1 at a known pressure and temperature into the volume V_M, and then the final pressure and temperature were read after the mercury in MAN1 was adjusted to mark M1.

The effective dead space volume, V_{Deff}, can be broken into two parts V_{D2}, and V_{D1} (Figure 12). The volume of the sample bulb and tubing in the cryostated area is designated as the cold dead space volume, V_{D1}, and is maintained constant at temperature T_1 by holding the level of the cryogenic medium at mark M2. The remainder of the dead space consists very nearly of a volume V_{D2} at temperature T_2 (room temperature). This is the so-called two temperature approximation, and every effort was made to make the division between V_{D2} and V_{D1} which occurs at mark M2 as sharp as possible. This was done by placing mark M2 within 1/2 inch of the top of the Dewar holding the cryogenic liquid, and placing a sheet of rubber dam at the liquid-air interface to help control evaporation.

In order to get an expression for the variation of effective dead space, V_{Deff}, with temperature, it was necessary to make volume measurements of V_{Deff} at several temperatures and to solve the equation

$$V_{Deff} = V_{D1}\left(\frac{T_2}{T_1}\right) + V_{D2} \qquad \text{(III-18)}$$

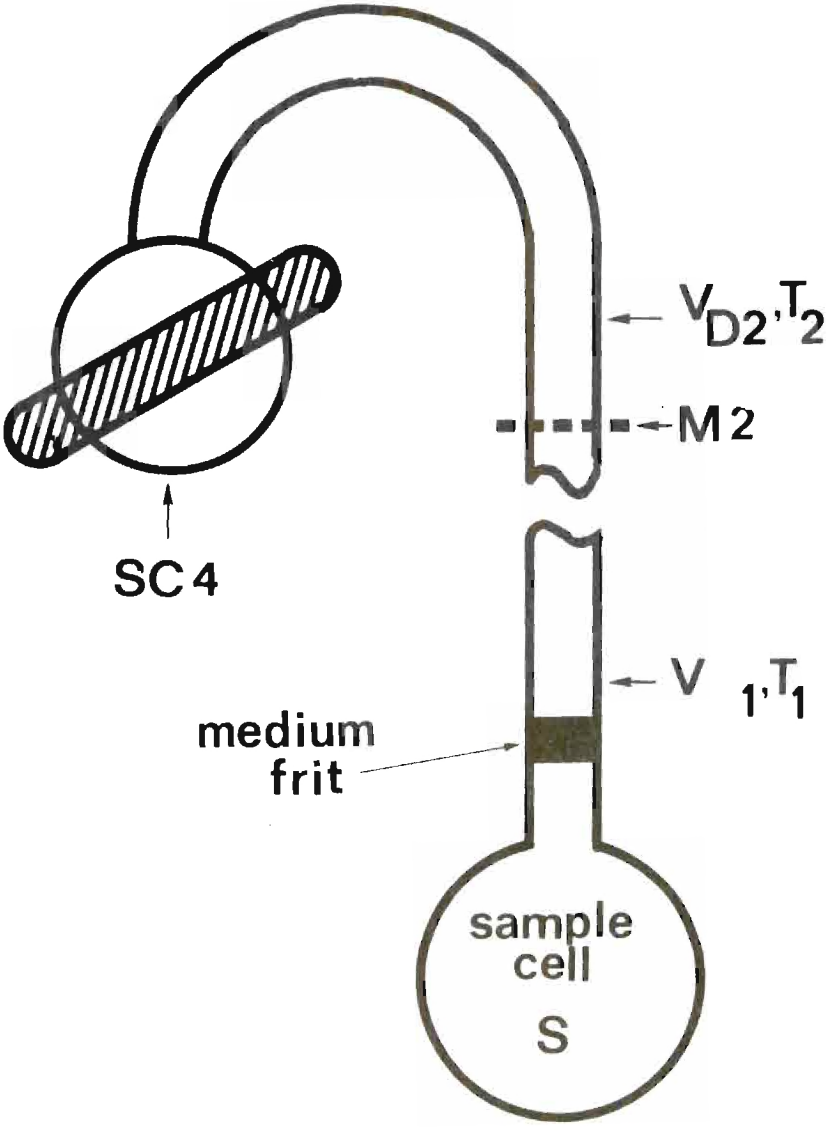

Figure 12. The Dead Space

simultaneously using measurements made at different values of T_1. To implement this, volume V_M was first calibrated and then measurements of V_{Deff} were made using T_1 = room temperature, T_1 = liquid nitrogen temperature and T_1 = dry ice temperature.

The temperature of the cryogenic medium was measured with a vapor pressure thermometer MAN2 (Figure 8) which was filled with a suitable gas; Matheson "Extra Dry" Nitrogen for liquid nitrogen temperature, and Matheson "Bone Dry" CO_2 for dry ice temperature). The tip of Probe P1 was blown very thin and placed as close as possible (1/8 inch) to the sample bulb so that the probe temperature would be very nearly the same as the sample bulb temperature. The pressure of gas read on MAN2 was converted to its corresponding temperature using the Antoine equation (see Appendix A).

To carry out isotherm measurements on the high pressure side, an amount of gas is admitted into the manifold volume, V_M, and its pressure is measured on manometer MAN1. The amount (in micromoles) of gas admitted to V_M is called a dose, N_{DOSE}, and the amount adsorbed N_{ADS} is found from the following equation

$$N_{ADS} = \left(\sum_{DOSES} N_{DOSE} \right) - N_{DS} \qquad \text{(III-19)}$$

where N_{DS} is the amount (micromoles) in the dead space.

Knowing the effective dead space, V_{Deff}, as a function of temperature permitted calculation of N_{DS} since

$$N_{DS} = \frac{P_f VD2}{RT_{2f}} + \frac{P_f VD1}{RT_1} \qquad \text{(III-20)}$$

where P_f is the final pressure in V_M, T_{2f} is the final temperature T_2, and R is the gas constant. Thus,

$$N_{DS} = \frac{P_f}{RT_{2f}} \left[VD1 \frac{T_{2f}}{T_1} + VD2 \right]. \qquad \text{(III-21)}$$

We recognize the expression in brackets as Equation (III-18) and thus,

$$N_{DS} = \frac{P_f}{RT_{2f}} V_{Deff} \qquad \text{(III-22)}$$

The quantity N_{DOSE} is actually the number of micromoles of gas which has disappeared from the manifold into the sample bulb; this is the difference between the amount initially in V_M, and that remaining after SC4 is opened. N_{DOSE} is thus

$$N_{DOSE} = \frac{P_i VM}{RT_{2i}} - \frac{P_f VM}{RT_{2f}} \qquad \text{(III-23)}$$

and

$$N_{DOSE} = \frac{VM}{RT_{2i}} \left[P_i - P_f \left(\frac{T_{2i}}{T_{2f}} \right) \right]. \qquad \text{(III-24)}$$

Thus, with Equations (III-19), (III-22) and (III-24), we can find the number of micromoles of gas adsorbed as a function of the final pressure, P_f. The data obtained are plotted as amount adsorbed per gram, N_{ADS}/W, where W = 4.7327 grams for TiC-8.

Calibration of the Low Pressure Side and Calculation of Adsorption Isotherms

On the low pressure side (Figure 9) the manifold volume, VM, is defined as the volume between marks M5, M6, and M7, this includes the volume of the McLeod gauge. The effective dead space, V_{Deff}, lies between marks M4, M5 and S, again being divided into a room temperature dead space, VD2 (between marks M4, M5, and M3) and a cold temperature dead space (mark M3 to S). The cold dead space was transferred intact from the high pressure side, so a recalibration of VD1 utilizing several temperatures was not necessary. Of course VM and VD2 had to be calibrated. This was done by expanding helium (Matheson "High Purity") from the known volume of the McLeod gauge into the proper sections of the system, and applying the ideal gas law. The equations used to calculate N_{ADS} are identical to those described previously with one slight addition. When the P_f is read the mercury in MAN4 is at mark M4, but when a new dose is added, the mercury must be at mark M5; thus some gas is forced out of VD2 when the mercury is raised from M4 to M5. This is easily corrected by reading a new final pressure after the mercury is raised and employing Equation (III-24) to calculate the amount expelled. This amount is subtracted from $\sum_{DOSES} N_{DOSE}$ in Equation (III-14). Of course when thermal transpiration corrections are important (usually below 1 torr) they must be applied to the pressure in VD1 when calculating the N_{DS}, using the procedure described earlier.

CHAPTER IV

THERMODYNAMICS OF ADSORPTION

The thermodynamics of adsorption are given in the excellent treatments of Young and Crowell (46), Ross and Olivier (39), and Hill (47). The procedures used in this study for calculating the thermodynamic properties of the adsorbed phase follow closely those outlined by the above.

One of the most useful thermodynamic properties to calculate for the adsorbed phase is the isosteric heat of adsorption, q_{st}. The isosteric heat is the amount of heat absorbed when one mole of gas is desorbed at constant temperature, T and pressure, p from an infinitely large surface without changing the surface concentration, θ. This heat is easily calculated from a series of isotherms by applying the following equation (which is derived from the Clausius-Clayperon equation)

$$q_{st} = -RT^2\left(\frac{\partial \ell np}{\partial T}\right)_\theta = R\left(\frac{\partial \ell np}{\partial (1/T)}\right)_\theta \qquad \text{(IV-1)}$$

where R = the gas constant.

T = the temperature in °K.

p = the pressure.

θ = the surface coverage.

This heat of adsorption is called the isosteric heat of adsorption

because it is calculated from adsorption isosteres (p vs. T at constant θ).

In the present work Equation (IV-1) was used to obtain the isosteric heats of adsorption of argon and benzene on TiC-8. For argon adsorption there were only two temperatures involved and thus the partial derivatives were changed to differentials. In the case of benzene adsorption however, there were five temperatures involved. In this situation the isosteric heats were determined by applying a linear least-squares analysis to the lnp vs. 1/T data after plotting on large-scale graph paper showed that this relationship was linear within experimental precision. These results will be discussed in the next chapter. The values of the isosteric heats can be found tabulated in Appendix C.

The next thermodynamic property of the adsorbed layer which was calculated was the spreading pressure, ϕ. The spreading pressure was calculated so that the molar entropy of the adsorbed layer could be found for benzene (this quantity is needed later in calculating the site energy distributions). The procedure used is that described by Hill (47). The following equation is used to determine ϕ from adsorption isotherms (θ vs. p at constant T)

$$\phi = RT \int_0^p \Gamma d(\ln p). \qquad \text{(IV-2)}$$

where Γ equals the number of moles of gas adsorbed per unit surface area.

In order to evaluate the integral in Equation (IV-2), the experimental data of the isotherms were plotted as N_{ADS}/W vs. p on very large pieces of graph paper (using a number of different scales) and smooth curves were very carefully drawn through the data and extrapolated to the origin. The isotherms were then taken in sections and values of N_{ADS}/W at selected intervals of p were read off. A Simpson's rule area was then calculated to evaluate the integral at each pressure. The first section included the origin and a number of low coverage points. The resultant spreading pressures are very sensitive to the manner in which the experimental curves are extrapolated, but fortunately the low coverage area contained data with very little scatter. The values of ϕ found for benzene on TiC-8 are given in Appendix C.

Next the isothermal differential heats of adsorption, $\Delta\bar{H}$ were calculated using the following

$$\Delta\bar{H} = RT^2\left(\frac{\partial \ln p}{\partial T}\right)_{\phi} = -R\left(\frac{\partial \ln p}{\partial (1/T)}\right)_{\phi} \qquad \text{(IV-3)}$$

In order to evaluate this heat, plots of ϕ vs. lnp were made on very large pieces of graph paper (again using a number of different scales). Values of p were read off each plot at constant ϕ. Plots were then made of lnp vs. 1/T and these were found to be linear within experimental error. A linear least-squares analysis was then performed on the lnp vs. 1/T data and values of the isothermal differential heat of adsorption were calculated. Values of this heat are tabulated in Appendix C.

Values of the difference in molar entropies of the gas and adsorbed phase can now be calculated using the relationship

$$\bar{S}_G - \bar{S}_S = \frac{\Delta\bar{H}}{T} = \Delta\bar{S}^{\circ} \qquad \text{(IV-4)}$$

where $\bar{S}_G$ is the molar entropy of the gas phase and $\bar{S}_S$ is the molar entropy of the adsorbed phase and S is the experimental differential molar entropy. This calculation was done only for the reference state for the adsorbed phase which was chosen as $\theta = 0.5$. The value of $\theta = 0.5$ was chosen as a reference state for the adsorbed phase mainly as a matter of convenience and also to eliminate any contributions from a configurational entropy term (39).

In order to evaluate $\Delta\bar{S}^{\circ}$, values of the pressure at $\theta = 0.5$ were read off at the large isotherm plots and then values of ϕ were obtained from the ϕ vs. p plots. The value of $\Delta\bar{H}$ was then obtained at this constant ϕ using Equation (IV-3) and Equation (IV-4) was then used to evaluate $\Delta\bar{S}^{\circ}$. The values obtained for the various isotherms will be presented and discussed in Chapter VI.

CHAPTER V

ADSORPTION MEASUREMENTS

Adsorption of Ar and N_2 in the High Pressure Range

The physical adsorption of Ar and N_2 on TiC-8 at liquid nitrogen temperature was studied using the high pressure (50-500 torr) side of the adsorption apparatus (Figure 8). A 4.7327 gram sample of TiC-8 was loaded into an adsorption sample cell (Figure 13) by means of the capillary neck. The sample cell was then sealed and attached to the adsorption system at position S (Figure 8) using 1/4-inch precision bore tubing. The 1/4-inch precision bore tubing extended beyond the border of the cryostatted area C1.

Adsorption isotherms of Ar and N_2 were measured at 77°K using liquid nitrogen as the cryogenic fluid. The gases used were transferred from lecture bottles to bulb B1 using PORT1 (Figure 8). Nitrogen was used in MAN2 to measure the temperature of the isotherm.

An expanded portion of the isotherm of nitrogen on TiC-8 is shown in Figure 14* along with an isotherm run on a 5.7242 g sample of Sterling FT graphitized carbon, the starting material from which TiC-8 was synthesized. The purpose of comparing these two isotherms is to notice the anomalous Joyner hump which begins at about 0.3 relative pressure on the Sterling FT, but which is absent on the TiC-8 isotherm.

---

*See Appendix D for error analysis.

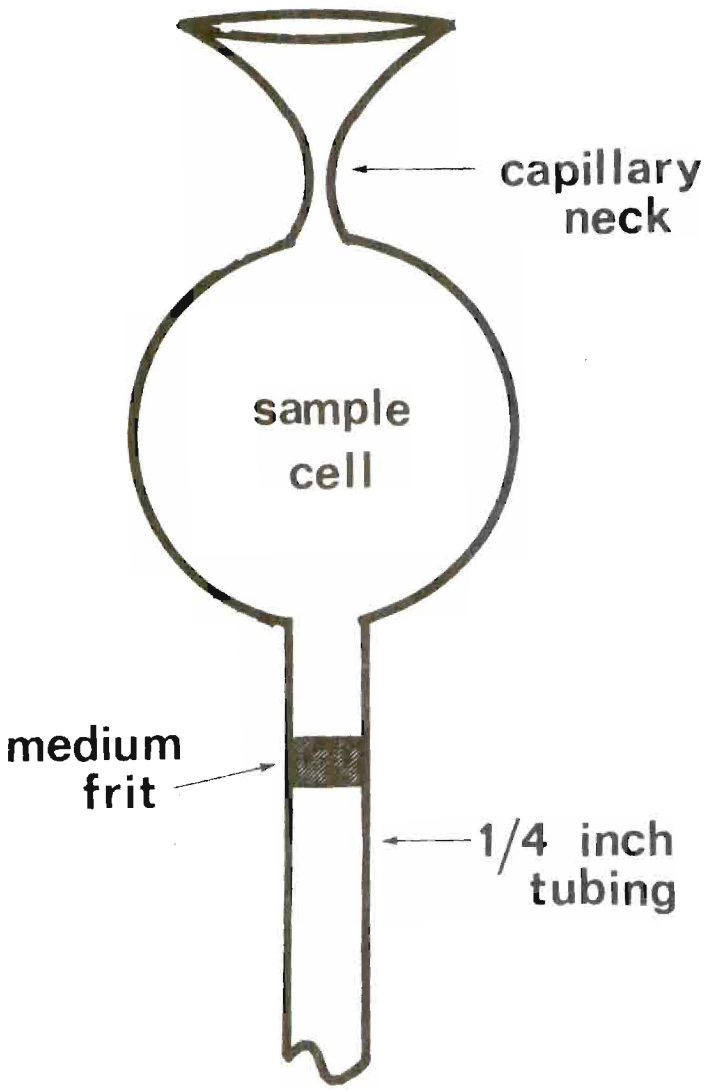

Figure 13. The Adsorption Sample Cell

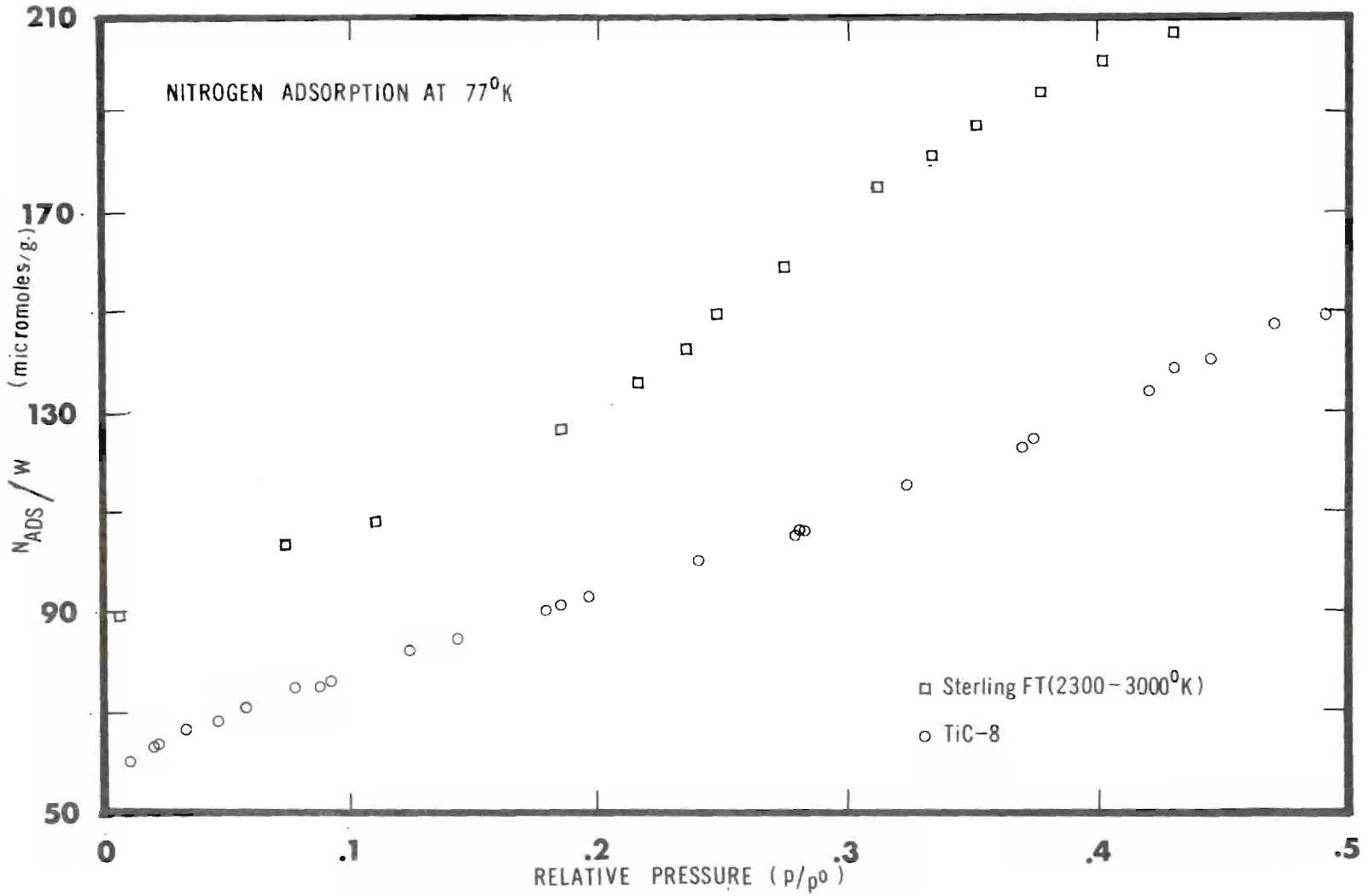

Figure 14. Adsorption Isotherms of Nitrogen at 77°K

Nitrogen on Graphon (3200°) or Sterling MT (3100°) also displays this Joyner hump (48). This result is significant in that it serves as one clue that we are not dealing with a single isoenergetic surface as is the case with the various graphitized carbon blacks. The Joyner hump is a sign of a single isoenergetic surface and is believed to be due to a change in the packing of the adsorbed nitrogen molecules (49). According to Pierce (49), the nitrogen molecules are lattice localized at the monolayer point and thus the effective cross-sectional area of the nitrogen molecule is greater than in the normal close-packed monolayer. As adsorption continues past the monolayer point, additional nitrogen molecules are accommodated in this first layer until there is a change from a localized to a mobile monolayer. It is this additional "crowding" in the first layer which leads to the step-like rise in the nitrogen isotherm which is called the Joyner hump. Because of this localized monolayer, the effective cross-sectional area of the nitrogen molecule on a graphite surface is 19.3$\mathring{A}^2$ (49), whereas on a normal close-packed monolayer it is 16.2$\mathring{A}^2$ (50). Another noteworthy difference between the isotherms is the "flatness" of the TiC-8 isotherm, which indicates a reduced tendency for multilayer formation. Both isotherms shown are composed of a mixture of adsorption and desorption points. Both isotherms were completely reversible with no hysteresis. The complete isotherm plots can be found in Appendix C and the isotherm data in Appendix B.

The monolayer capacity of nitrogen on Sterling FT at 77.20°K was determined using isotherm data points for the region of relative

pressures below 0.1 and applying this data using a linear least-squares fit to the BET equation (51). This method yielded a monolayer capacity of 97.5 micromoles/g. Using 19.3$\mathring{A}^2$ as the cross-sectional area for a nitrogen molecule on graphitized carbon as recommended by Pierce (49) yielded a surface area of 11.3 m^2/g.

The nitrogen—TiC-8 isotherm at 77.23°K did not obey the BET equation well enough to arrive at a reliable surface area. The monolayer capacity was obtained by the Point B method (52) which was later employed for all TiC-8 isotherms. The Point B method utilized a graphical detection of the change in the slope of the isotherm to estimate the monolayer capacity. When all isotherm measurements on TiC-8 were subjected to a Point B analysis, a self consistent set of adsorbate cross-sections were obtained, whereas the BET equation yielded various results. The monolayer capacity, V_M obtained for nitrogen on TiC-8 was 66.70 micromoles/g. Using 16.2$\mathring{A}^2$ as the cross-section of nitrogen (50) yields a surface area of 6.5±0.5 m^2/g. This value of the surface area is somewhat higher than the value of 4.4±0.5 m^2/g found from the electron microscopy particle size analysis (based on a density of 4.91 g/cc as calculated from the crystal lattice constant found for TiC-8). This higher surface area implies a roughness factor of about 1.5 (53), which suggests that TiC-8 has a greater amount of internal surface and/or a rougher outward surface than Sterling FT.

The adsorption isotherm of argon on TiC-8 turns out to be significantly different than the adsorption isotherm of argon on a graphitized carbon black. In Figure 15 are plotted isotherms for argon on

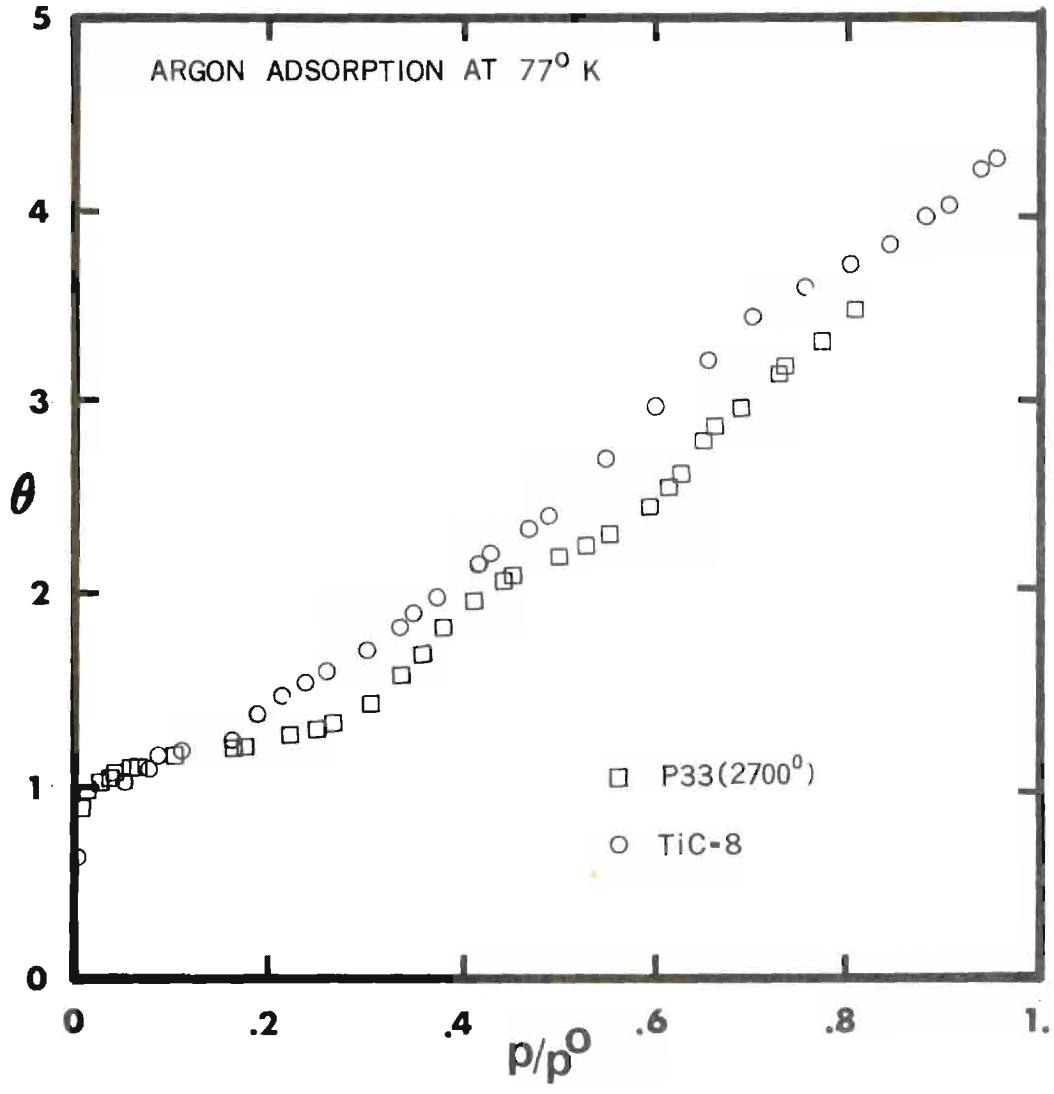

Figure 15. Adsorption Isotherms of Argon at 77°K

TiC-8* at 77.08±.03°K along with data of Singleton and Halsey (54) for argon on P-33 (2700°) graphitized carbon black at 77°K. The isotherms are plotted as a function of the surface coverage, θ, for comparison. The monolayer capacity, V_M, for TiC-8 is 66.70 micromoles/g and V_M given by Singleton and Halsey for P-33 (2700°) is 184.8 micromoles/g. As can be seen from Figure 15, argon on P-33 (2700°) exhibits a well-defined second layer step at about 0.37 relative pressure. This has also been reported by Prenzlow and Halsey (55). Argon on TiC-8 exhibits no signs of multilayer step formations. This would also serve to indicate the presence of some high energy sites instead of a uniform isoenergetic surface such as exhibited by the graphitized carbon blacks.

Adsorption of Argon and CH_4 in the Low Pressure Range

Isotherms of argon and methane were obtained in the low pressure range using the apparatus shown in Figure 9. Argon adsorption was studied at 77.08±.03°K and 90.05±.05°K using liquid nitrogen and liquid oxygen as the cryogenic fluids. Methane adsorption on TiC-8 was studied at 77.10±.04°K using liquid nitrogen as the cryogenic fluid.

In Figure 16 the adsorption of methane on TiC-8* at 77.10°K is compared with the adsorption of methane on exfoliated graphite at 77.4°K as reported by Thomy and Duval (56). The isotherms are plotted as a function of surface coverage, θ, versus relative pressure for comparison. It can be seen that methane on exfoliated graphite exhibits a nearly vertical second layer step at a relative pressure of about 0.36,

---

*See Appendix D for error analysis.

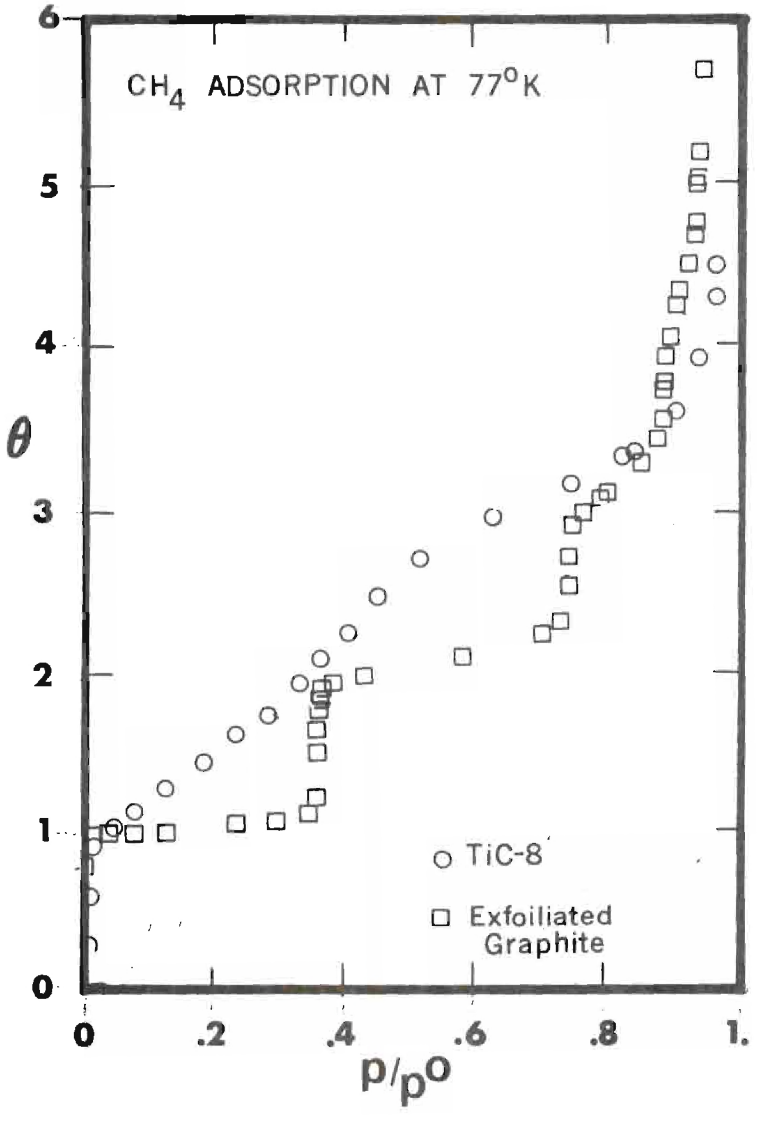

Figure 16. Adsorption Isotherms of Methane at 77°K

and also exhibits pronounced third and fourth layer steps as well. Methane on TiC-8 reveals none of these steps and is indeed quite featureless when compared to the exfoliated graphite isotherm.

Isotherms of argon on TiC-8* at 77.08°K and 90.05°K are shown in Figures 17, 18 and 19. The isotherms are composed of both adsorption and desorption points and are completely reversible. The solid line drawn through the points in Figure 17 is a visual aid only and is not intended to represent any type of mathematical fit to the data points.

The isosteric heat of adsorption was calculated as described earlier and is shown in Figure 20b. In Figure 20a the isosteric heat of adsorption of argon on P-33 (2700°) graphitized carbon is shown (57). There are several qualitative conclusions which can be drawn from the comparison of these two heat curves.

1. The isosteric heat showed an initial sharp decrease as high energy sites present on the TiC-8 were filled. There were not enough high energy sites on the P-33 (2700°) to show this effect.

2. The isosteric heat for argon on P-33 (2700°) decreases at the monolayer to nearly the heat of vaporization of bulk argon, H_v, and then increases as the second layer is filled. The isosteric heat for argon on TiC-8 actually dips very slightly below H_v at the completion of a monolayer. The values of the isosteric heat are tabulated in Appendix C.

---

*See Appendix D for error analysis.

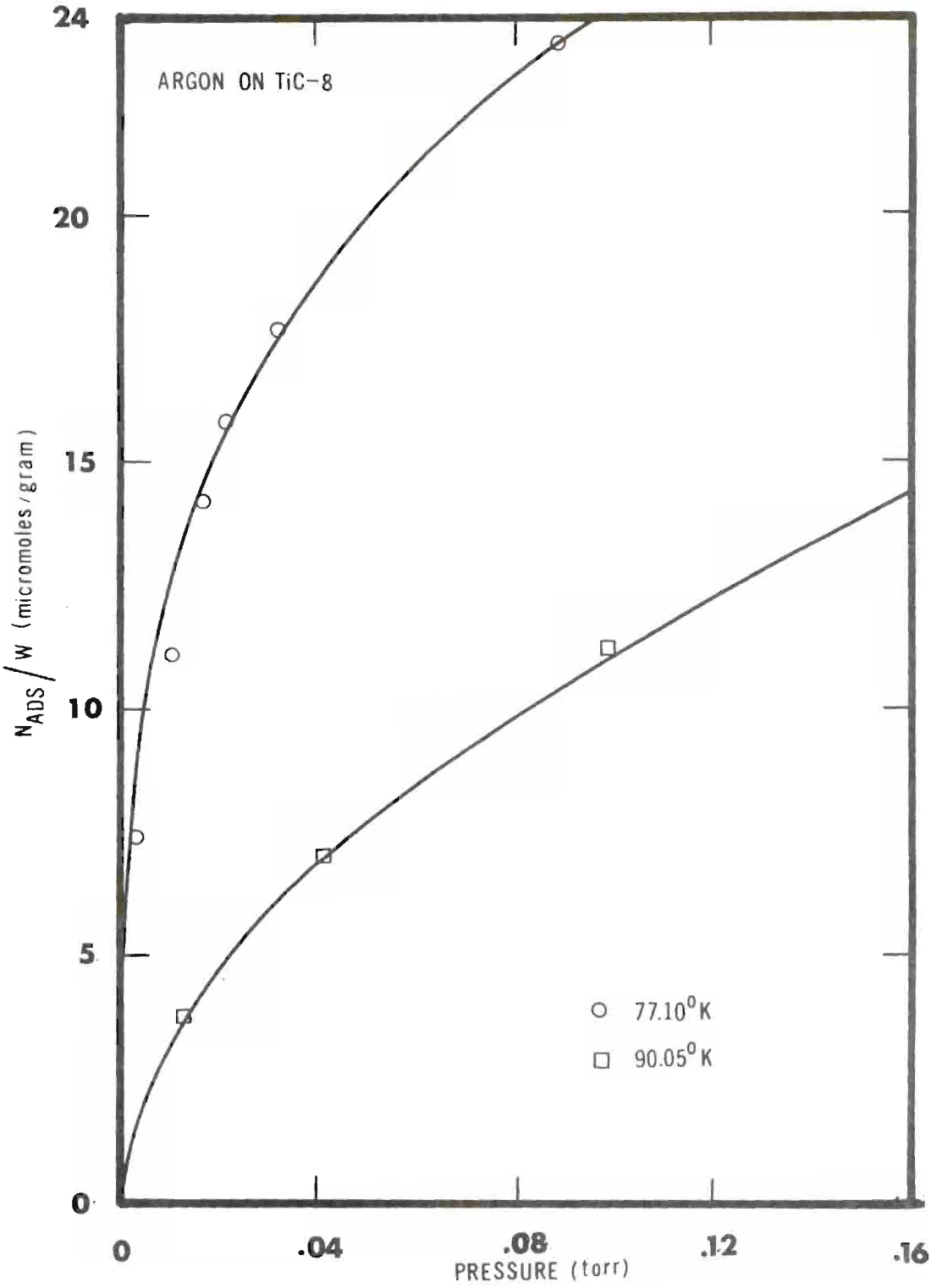

Figure 17. Adsorption Isotherms of Argon on TiC-8

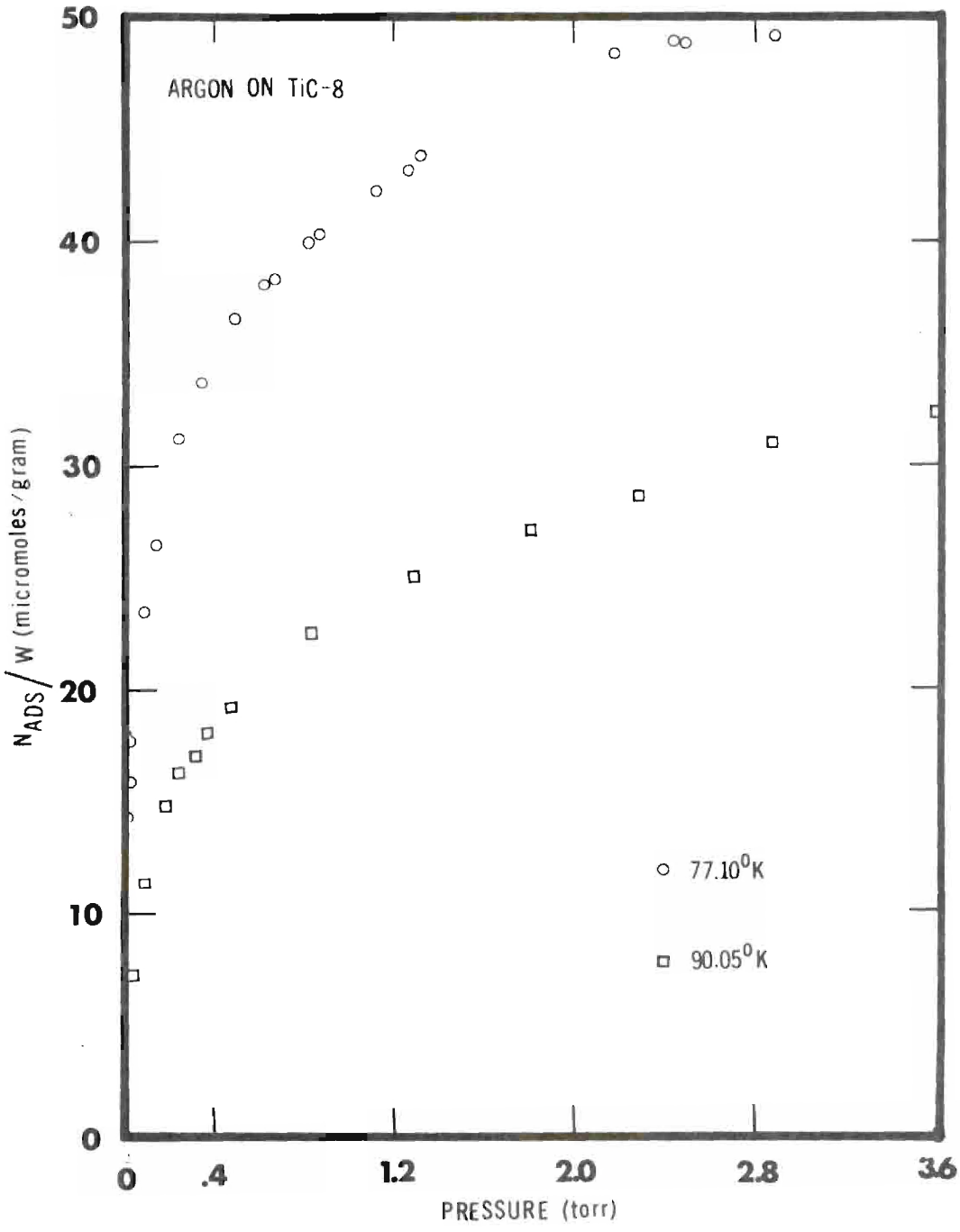

Figure 18. Adsorption Isotherms of Argon on TiC-8

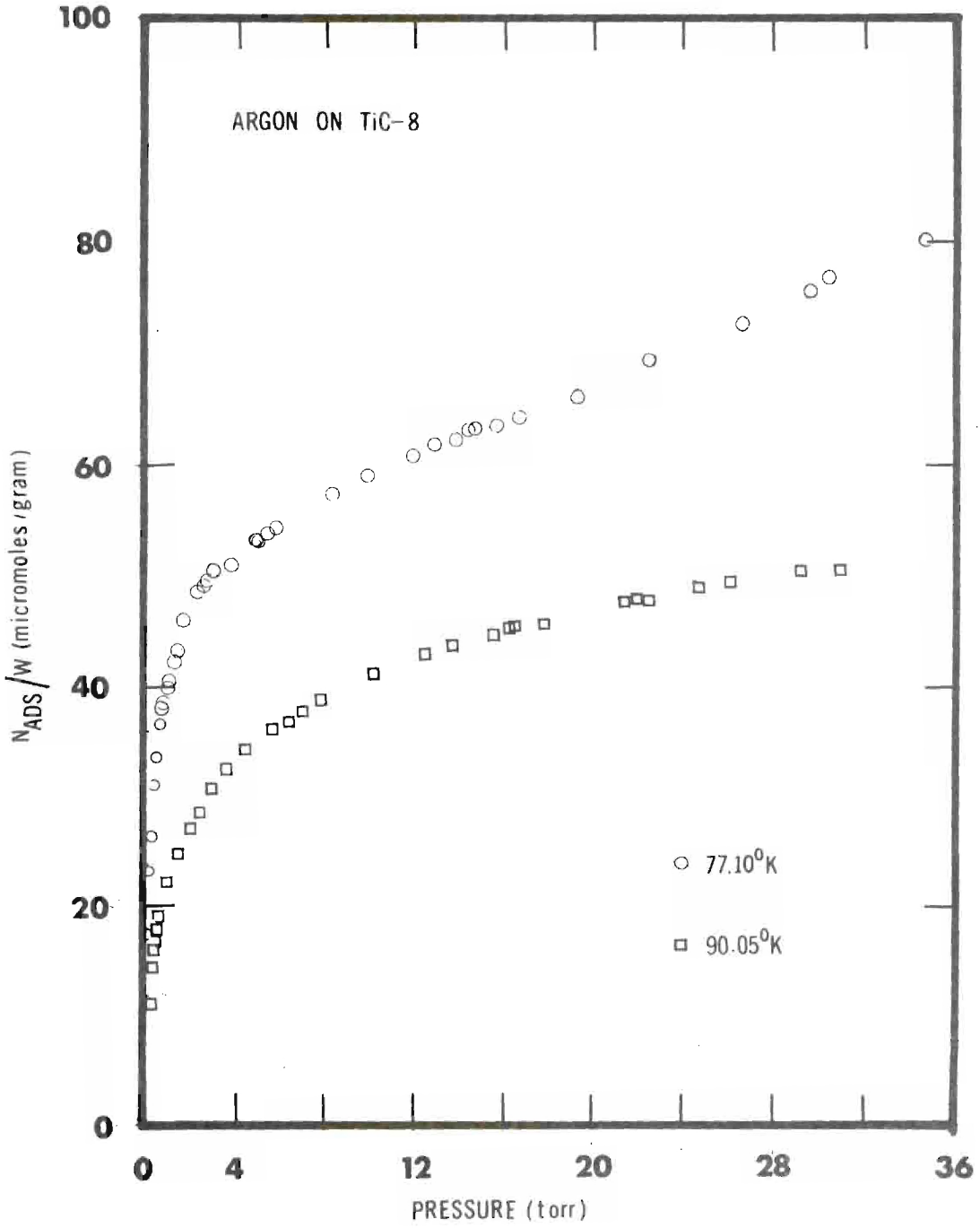

Figure 19. Adsorption Isotherms of Argon on TiC-8

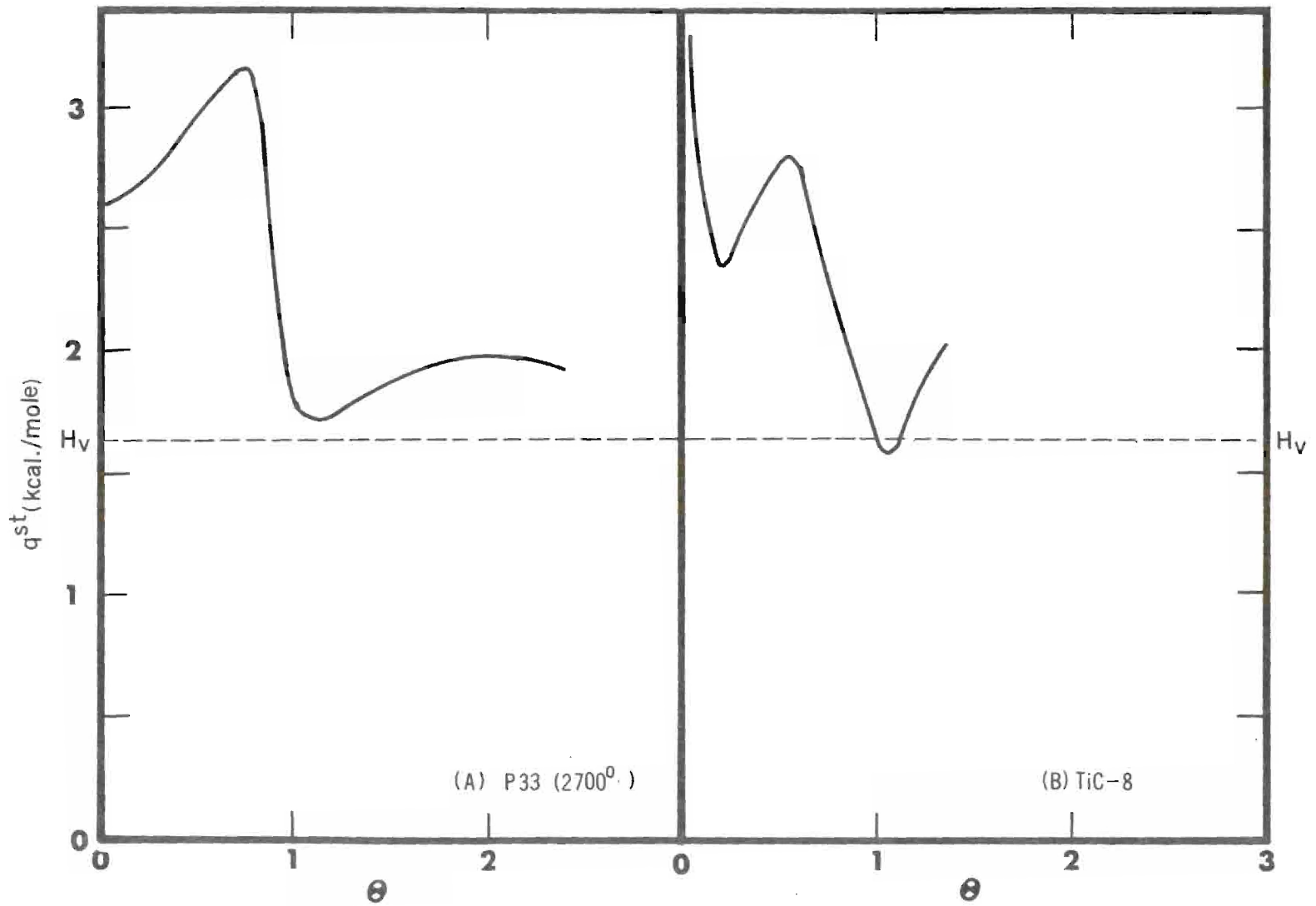

Figure 20. Isosteric Heats of Argon on P33 (2700°) and TiC-8

Adsorption of C_6H_6 on TiC-8

The physical adsorption of benzene on TiC-8 was studied using the low pressure side as shown in Figure 9. The cryostat described previously was used to obtain isotherms at temperatures of 251.73°K, 258.62°K, 263.01°K, 268.11°K, and a well-stirred ice bath was used for measurements at a temperature of 273.35°K.

The adsorption isotherms of benzene on TiC-8 are shown in Figures 21-27. The solid lines drawn through the points in Figures 21 and 22 are for visual aid only and again do not represent any mathematical fit to the data. All isotherms consist of both adsorption and desorption points and are completely reversible. These isotherms are similar in shape to those observed for benzene on graphitized carbon blacks by various authors such as Isirikyan and Kiselev (58), Smallwood (59) and Davis and Pierce (60). As Davis and Pierce (60) observed, the isotherms for benzene were observed to be concave to the pressure axis at the beginning of the isotherm.

In Figure 28a we have the isosteric heats for benzene adsorbed on Sterling MT graphitized carbon as reported by Davis and Pierce (60), and in Figure 28b we have the isosteric heats for benzene adsorbed on TiC-8. The heat curve for TiC-8 shows, from its initial steepness, more high energy sites are present on the TiC-8 surface than on the Sterling MT surface. This is in accord with what we have seen for argon adsorption on TiC-8. The net heats of adsorption (with reference to H_v for the pure solid) for the formation of the first layer are quite similar except that the net heat stays positive on the Sterling MT up to a

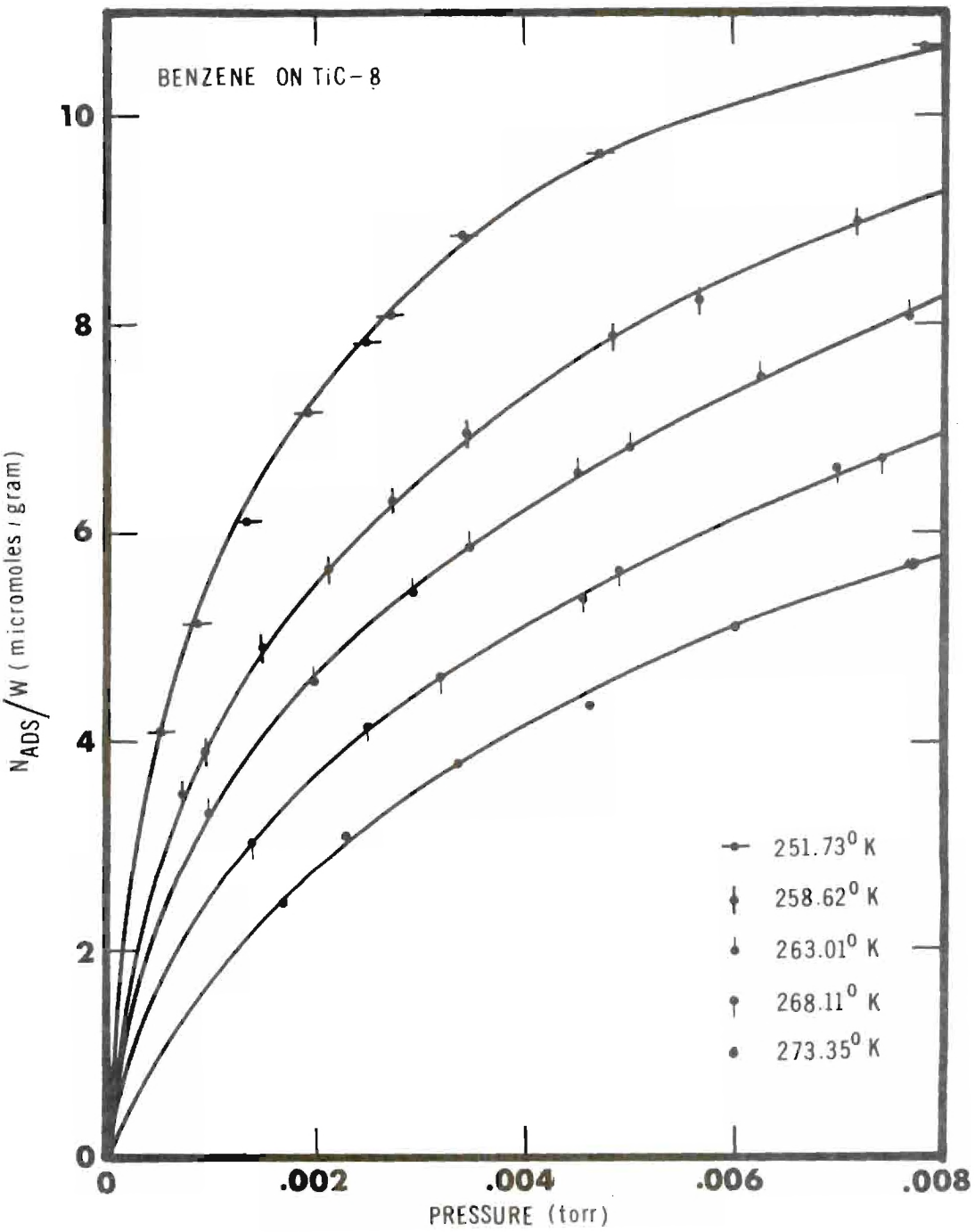

Figure 21. Adsorption Isotherms of Benzene on TiC-8

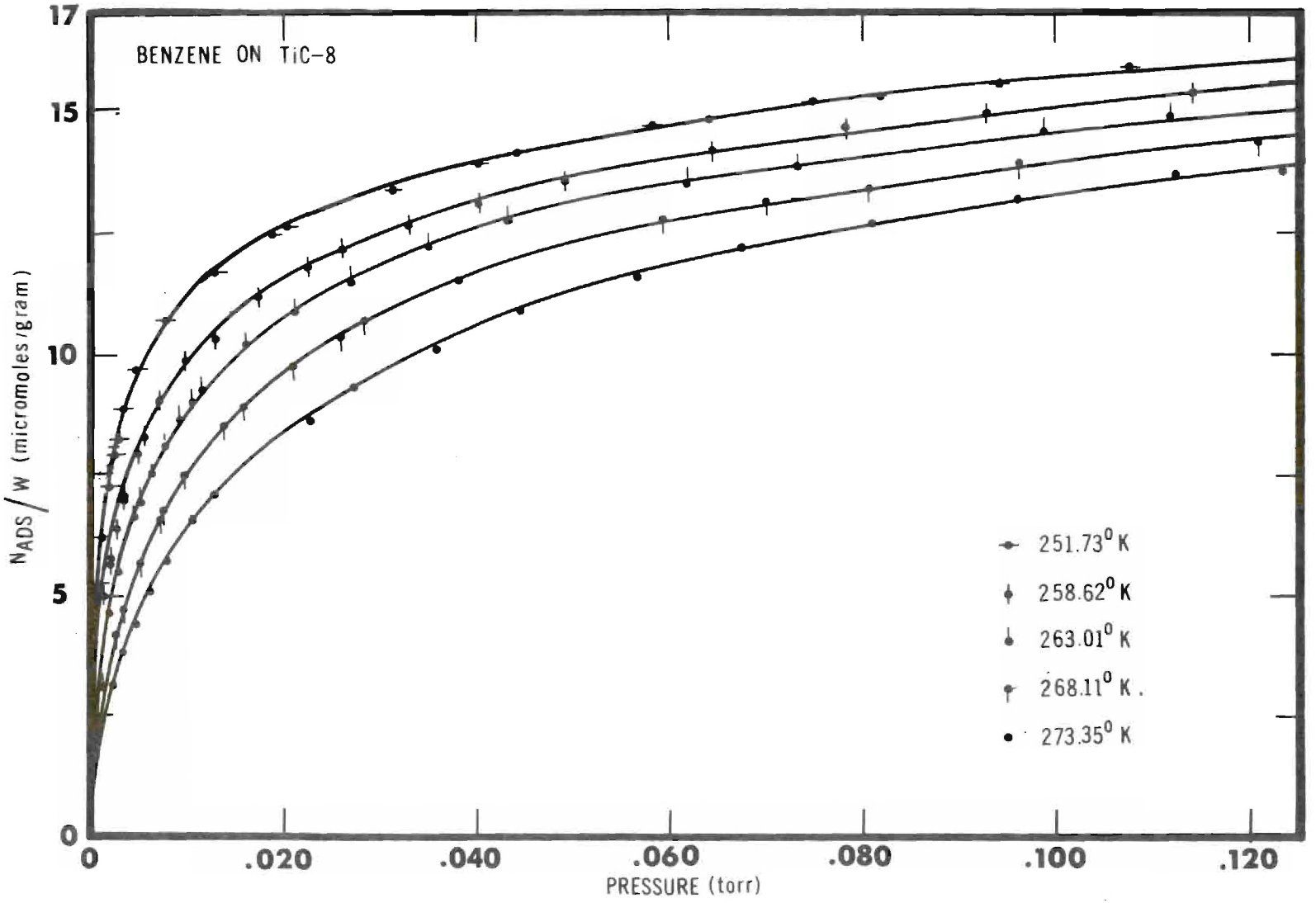

Figure 22. Adsorption Isotherms of Benzene on TiC-8

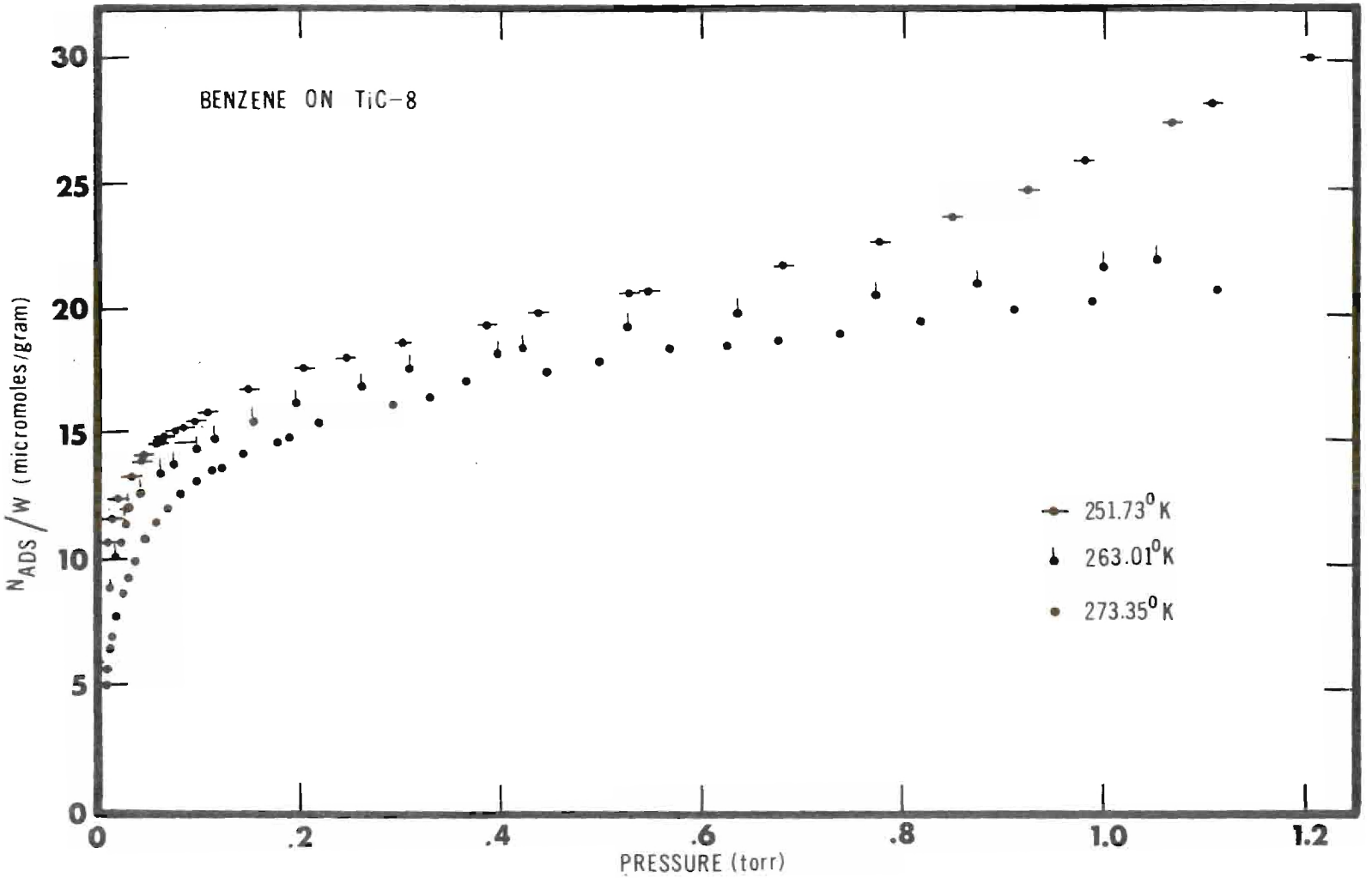

Figure 23. Adsorption Isotherms of Benzene on TiC-8

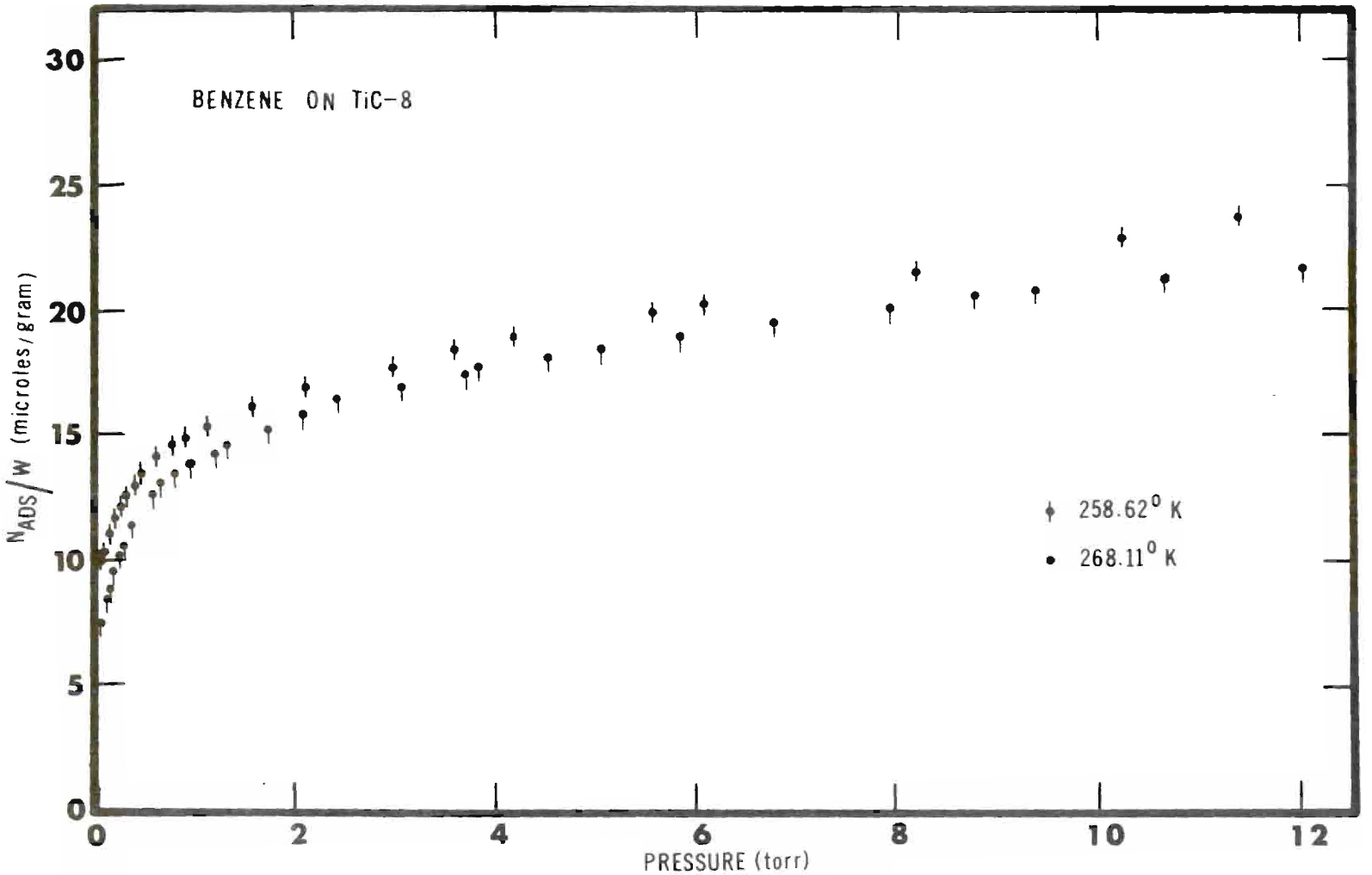

Figure 24. Adsorption Isotherms of Benzene on TiC-8

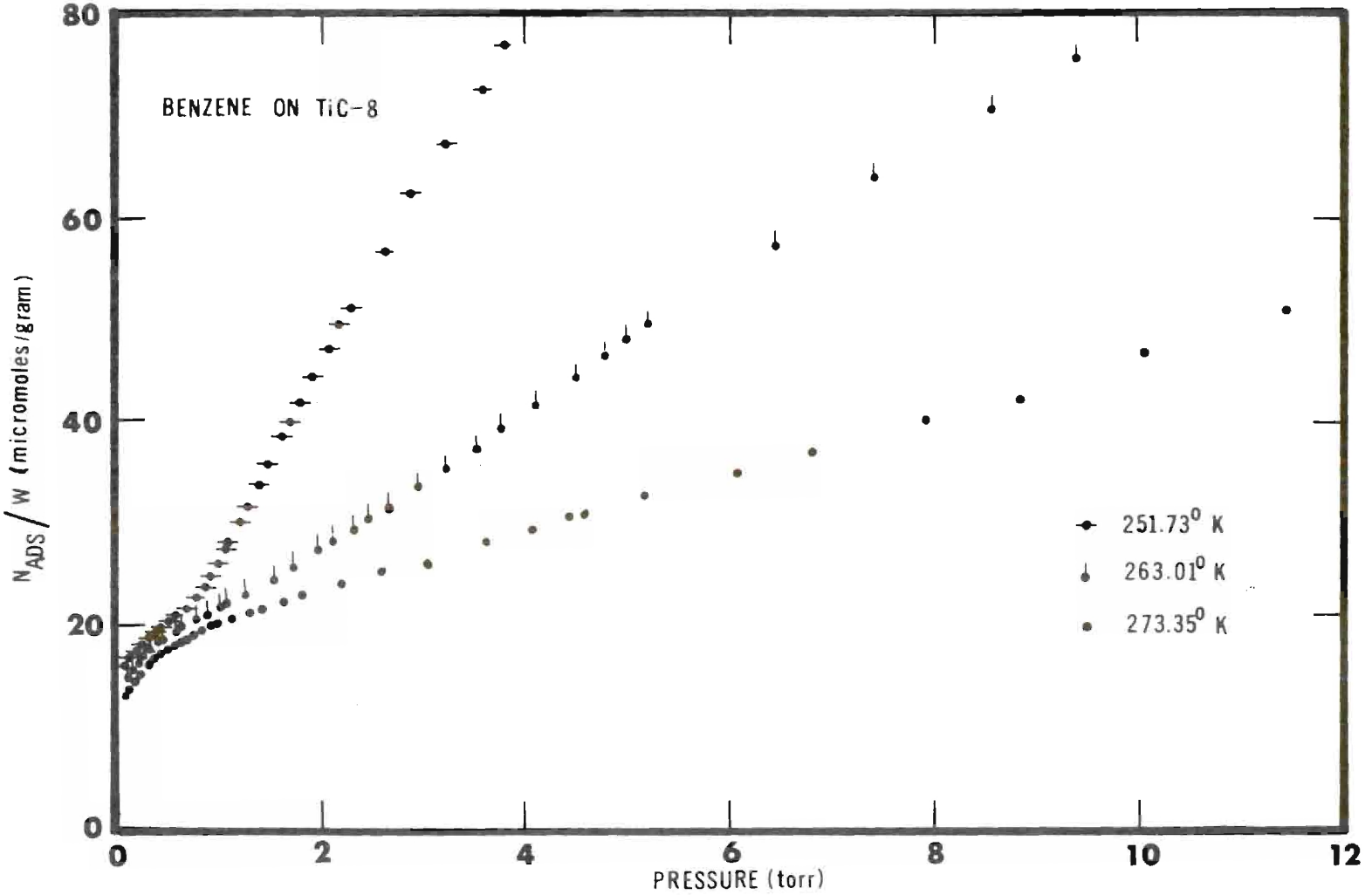

Figure 25. Adsorption Isotherms of Benzene on TiC-8

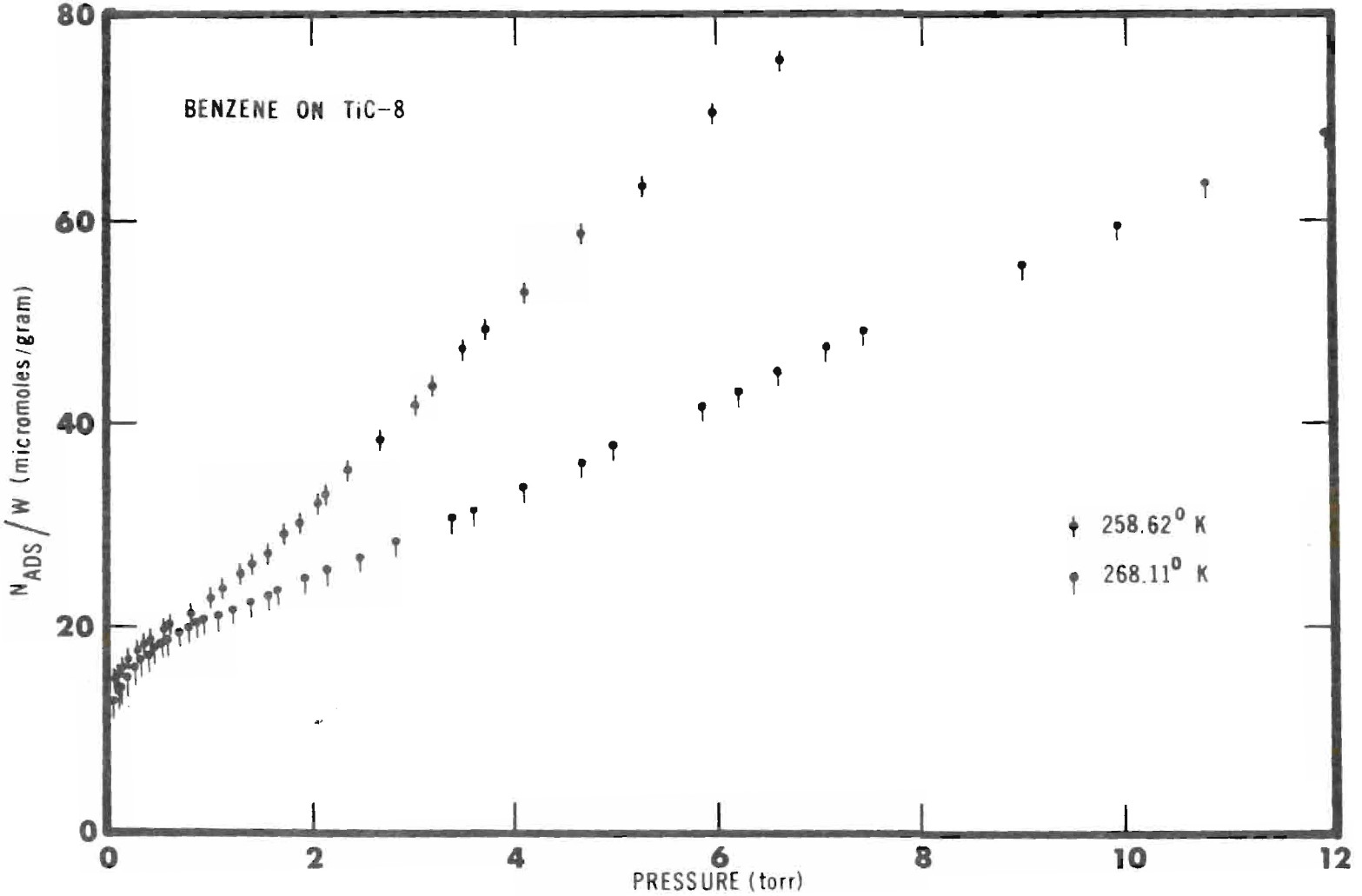

Figure 26. Adsorption Isotherms of Benzene on TiC-8

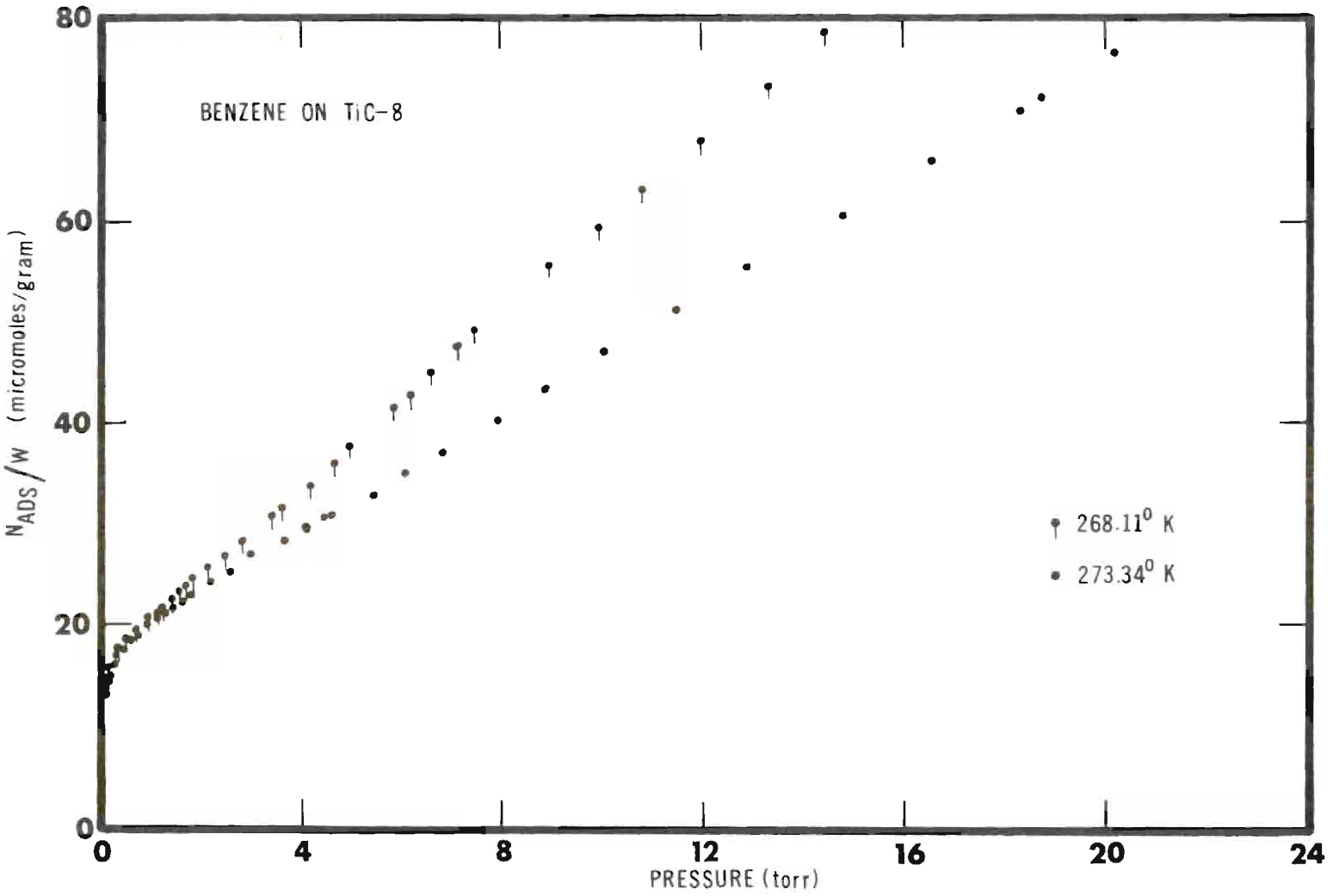

Figure 27. Adsorption Isotherms of Benzene on TiC-8

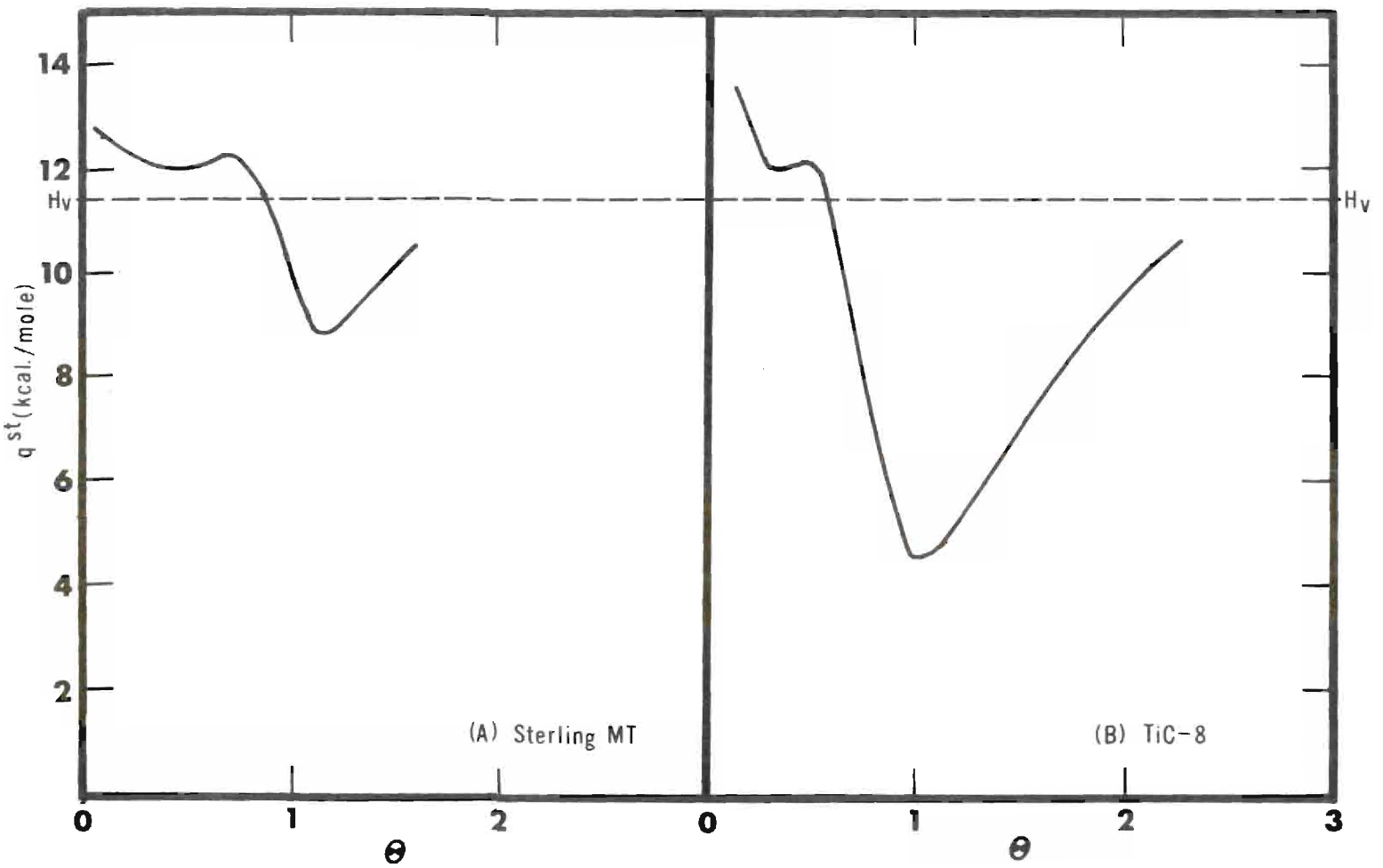

Figure 28. Isosteric Heats of Benzene on Sterling MT and TiC-8

coverage of about 0.9, while on TiC-8 the net heat turns negative at a coverage of about 0.6. What this means is that the structure of the adsorbed benzene layer on the Sterling MT surface is less compatible to additional benzene adsorption than is the adsorbed layer on the TiC-8 surface.

The isosteric heat curve for benzene on TiC-8 can be found tabulated in Appendix C. All isotherm data can be found in Appendix B. Table 5 lists all the monolayer capacities (using the Point B method) and calculated adsorbate cross-sections (using the cross-sectional area of nitrogen = 16.2$\mathring{A}^2$ as a standard). An error analysis of the isosteric heat curves can be found in Appendix D.

Table 5. Monolayer Capacities and Adsorbate Cross-Sections

Adsorbate	T(°K)	V_m $\left(\frac{\text{micromoles}}{g}\right)$	σ ($\mathring{A}^2$)
N_2	77.23	66.70	(16.2)
CH_4	77.10	66.10	16.3
Ar	77.10	61.35	17.6
	90.05	50.80	21.3
C_6H_6	273.35	20.46	52.8
	268.11	20.23	53.4
	263.01	20.13	53.7
	258.62	20.09	53.8
	251.73	20.00	54.0

CHAPTER VI

SITE ENERGY DISTRIBUTIONS

The Langmuir Equation

In 1918 Langmuir derived an equation to describe the adsorption of a gas onto a solid using a kinetic approach to the dynamics of adsorption. Using the basic assumption that a molecule is localized on an adsorption site, and that there are no interactions between adsorbed molecules, Langmuir set equal expressions for the rate of condensation and the rate of evaporation of adsorbed molecules and arrived at the equation

$$\theta = \frac{bP}{1 + bP} \quad \text{or} \quad bP = \frac{\theta}{1 - \theta} \qquad \text{(VI-1)}$$

where θ = the fraction of the surface sites occupied by an adsorbed molecule.

b = a constant which equals $1/P$ at $\theta = .5$.

Fowler (61) pointed out in 1935 that a kinetic derivation of Equation (VI-1) misleads one into thinking that the derivation was dependent upon the precise mechanisms of condensation and evaporation, whereas the derivation actually depends only upon the entire set of states (either adsorbed or gaseous) which is accessible to the molecule.

The molecular partition function for the molecule in the gas phase is composed of the molecular partition function for translational degrees of freedom and the molecular partition function for internal degrees of freedom, *viz.*

$$q^g = q^g_{trans} q^g_{int} \qquad \text{(VI-2)}$$

and the complete partition function is

$$Q^g(N,V,T) = \frac{1}{N!} (q^g)^N \qquad \text{(VI-3)}$$

The molecular partition function for the molecule in the adsorbed phase is

$$q^s = q^s_{site} q^s_{int} e^{Q/kT} \qquad \text{(VI-4)}$$

In the above equations q^g_{int} and q^s_{int} are the molecular partition functions for the internal energy of the molecule in the gaseous and in the adsorbed states, respectively. In order to investigate the equilibrium between the molecule in the gas phase and the molecules on the surface, we must choose the same zero of energy. We take an isolated gas molecule at rest as our zero of energy and use the factor $e^{Q/kT}$ in Equation (VI-4) to give the same zero of energy to the adsorbed molecule. This follows the approach used by Fowler and Guggenheim (62) and Q is thus the energy required to take a molecule from its lowest energy

state in an adsorbed monolayer to a point an infinite distance from the surface where it becomes a gas state molecule in its lowest energy level.

The molecular partition function for an adsorbed molecule, q^s, is a function of temperature only, and not of the degree of occupancy of the sites. To obtain the ensemble partition function, we need to multiply q^s by the number of distinguishable ways of placing N molecules on S sites. The first molecule adsorbing on the empty surface has S sites to choose from, the second has (S-1) and so on; thus, for N molecules there are

$$\frac{S!}{N!(S-n)!} \tag{VI-5}$$

ways of arranging N indistinguishable molecules on S sites.

Thus, the total partition function for the adsorbed phase is

$$Q^s(N,V,T) = \frac{S}{N!(S-N)!}(q^s)^N \tag{VI-7}$$

The Helmholtz free energy is given by

$$A(N,V,T) = -kT\ln Q(N,V,T), \tag{VI-8}$$

or for the adsorbed phase

$$A^s = -kT\ln\left[\frac{S}{N!(S-N)!}(q^s)^N\right]. \tag{VI-9}$$

Using Sterling's approximation for large factorials ($\ln x! = x\ln x - x$) gives us,

$$A^S = kT[-S\ln S + N\ln N + (S-N)\ln(S-N) - N\ln q^S]. \qquad \text{(VI-10)}$$

The chemical potential is given by

$$\mu^S = \left(\frac{\partial A^S}{\partial N}\right)_{T,V,S}, \qquad \text{(VI-11)}$$

thus,

$$\mu^S = kT\ln\left(\frac{N}{S-N}\right) - \ln q^S. \qquad \text{(VI-12)}$$

For the gas phase

$$Q(N,V,T) = \frac{1}{N!}\,(q^g)^N, \qquad \text{(VI-13)}$$

and the Helmholtz free energy is

$$A^g = -kT[N\ln q^g - N\ln N + N], \qquad \text{(VI-14)}$$

and the chemical potential is given by

$$\mu^g = -kT\left[\ln\left(\frac{q^g}{N}\right)\right]$$

At equilibrium we have $\mu^g = \mu^s$, so we set Equation (VI-15) equal to Equation (VI-12). We can eliminate kT from the two equations and define a variable Θ, which is the fraction of the surface covered or

$$\Theta = N/S. \tag{VI-16}$$

This yields

$$\frac{\Theta}{1 - \Theta} = \frac{q^s}{(q^g/N)}. \tag{VI-17}$$

We now recall Equation (VI-2)

$$q^g = q^g_{trans} q^g_{int}, \tag{VI-2}$$

and evaluate the translational molecular partition function, q^g_{trans}.

From an analysis of the classical particle in a three-dimensional box, we arrive at the following expression

$$\frac{q^g_{trans}}{N} = \left(\frac{2\pi mkT}{h^2}\right)^{3/2}\left(\frac{V}{N}\right) \tag{VI-18}$$

and using the ideal gas law PV = nkT we get

$$\frac{q^g_{trans}}{N} = \left(\frac{2\pi mkT}{h^2}\right)^{3/2}\left(\frac{kT}{P}\right). \tag{VI-19}$$

Substituting this result into Equation (VI-17) gives us

$$\frac{\Theta}{1 - \Theta} = \left[\left(\frac{h^2}{2\pi mkT}\right)^{3/2}\left(\frac{P}{kT}\right)\right] \frac{q^s}{q^g_{int}} . \qquad \text{(VI-20)}$$

There are two different assumptions which can be made at this point in evaluating q^s (since there are two different types of localized monolayers with which we can be concerned). The first type of localized monolayer assumption leads to the harmonic-oscillator (HO) model, and has been treated by Fowler (61). In the HO model each molecule is attached to the surface at a definite point. These points of attachment are capable of holding only one molecule, and the three degrees of translational freedom of the molecule in the gas phase are thus converted to three degrees of vibrational freedom about the point of attachment of the molecule. In the second localized monolayer model, called the particle-in-a-box (PB) model, some point of the adsorbed molecule, such as its center of mass, is bound tightly to the surface while allowing freedom of movement in two directions along the surface. This freedom of movement is restricted by the potential of the surface, and perhaps by interactions with other adsorbed molecules, to an effective two-dimensional "box" whose area is the observed experimental adsorbate cross-section. Thus, one degree of the three degrees of translational freedom of the gas phase molecule is converted to a vibrational degree of freedom normal to the surface, while the remaining two degrees are converted to translational degrees of freedom in a two-dimensional box.

Localized Harmonic Oscillator Model

We now make the assumption that when the molecule is adsorbed, uts three degrees of translational freedom become three degrees of vibrational freedom. One vibration of frequency ν_z is normal to the surface, and the other two vibrations of frequencies ν_x and ν_y are parallel to the surface.

Thus, the molecular partition function for the adsorbed molecule, q^s, becomes

$$q^s = q^s_{vib-x} q^s_{vib-y} q^s_{vib-z} q^s_{int} \exp(Q/kT). \qquad \text{(VI-21)}$$

To evaluate q^s_{vib-i}, where the subscript i refers to the *ith* vibrational mode, we begin with the harmonic oscillator approximation

$$\varepsilon_{ivib} = (n+\tfrac{1}{2})h\nu_i \qquad \text{(VI-22)}$$

and

$$q^s_{vib-i} = \prod_i \frac{e^{-h\nu_i/2kT}}{1 - e^{-h\nu_i/kT}}$$

For the localized Langmuir model the assumption

$$\nu_x = \nu_y = \nu_z = \nu_s \qquad \text{(VI-24)}$$

is often used (63). This assumption is used because at the present time there is no experimental data which would enable us to evaluate ν_x, ν_y

and ν_z separately. Thus, the localized Langmuir model gives us the following expression for Equation (VI-18)

$$\frac{\theta}{1-\theta} = \left[\left(\frac{h^2}{2\pi mkT}\right)^{3/2} \frac{P}{kT}\right]\left[\left(\frac{e^{-h\nu_s/2kT}}{1-e^{-h\nu_s/kT}}\right)^3\right] \exp\left(\frac{Q}{kT}\right) \frac{q^s_{int}}{q^g_{int}} \qquad \text{(VI-25)}$$

Before we can apply Equation (VI-25) to calculating a b value for benzene adsorbed on the TiC-8 surface, we need to evaluate q^s_{int}/q^g_{int}. To do this we must realize that

$$\frac{q^s_{int}}{q^g_{int}} = \frac{q^s_{rot} q^s_{vib}}{q^g_{rot}} \left(\frac{q^s_{\text{internal vibrations}} q^s_{el}}{q^g_{\text{internal vibrations}} q^g_{el}}\right) \qquad \text{(VI-26)}$$

where q^s_{rot} and q^g_{rot} are the molecular partition functions of the benzene molecule in the adsorbed and gas phase, respectively; q^s_{vib} is the molecular partition function for the vibrational degrees of freedom (other than the three vibrational degrees of freedom arising from the loss of three translational degrees of freedom as discussed earlier); q^g_{rot} is the molecular partition function for the rotational degrees of freedom of the benzene molecule in the gas phase; $q^s_{\text{internal vibrations}}$ and $q^g_{\text{internal vibrations}}$ are the molecular partition functions for the internal vibrational degrees of freedom of the benzene molecule in the adsorbed and gas phase, respectively; q^s_{el} and q^g_{el} are the molecular partition functions for the electronic energy levels of the benzene molecule in the adsorbed and gas phase, respectively. The internal

vibrational and electronic states of the benzene molecule are assumed to be unaffected upon adsorption and thus the ratio of their partition functions becomes unity.

From Hill (64) we obtain the following expression for q^g_{rot}:

$$q^g_{rot} = \frac{\pi 1/2}{\sigma^g_{C_6H_6}} \left(\frac{8\pi^2 I_A kT}{h^2}\right)^{1/2} \left(\frac{8\pi^2 I_B kT}{h^2}\right)^{1/2} \left(\frac{8\pi^2 I_C kT}{h^2}\right)^{1/2} \qquad \text{(VI-27)}$$

where I_A, I_B, and I_C are the three moments of inertia of the benzene molecule and are described by

$$I_C > I_A = I_B \qquad \text{(VI-28)}$$

with I_A and I_B being in the plane of the ring and I_C being about the six-fold axis normal to the ring. The quantity $\sigma^g_{C_6H_6}$ is a symmetry factor for the benzene molecule in the gas phase. The symmetry factor is the number of different ways a molecule can obtain the same orientation by rotation (counting like atoms as indistinguishable). For benzene in the gas phase, since there is a six-fold axis of rotation combined with a two-fold axis of rotation $\sigma^g_{C_6H_6} = 12$ (64). Upon being adsorbed, the degrees of rotational freedom about the A and B axis are lost and become torsional vibrational degrees of freedom. Thus, for the adsorbed phase we have

$$q^s_{rot} = \frac{\pi^{1/2}}{\sigma^s_{C_6H_6}} \left(\frac{8\pi^2 I_C kT}{h^2}\right)^{1/2} \qquad \text{(VI-29)}$$

where $\sigma^{s}_{C_6H_6}$ is now the symmetry factor for the benzene molecule in the adsorbed phase. For benzene $\sigma^{s}_{C_6H_6} = 6$ (65), since only the six-fold axis of rotation is left. In other words, we postulate that the benzene molecule is laying flat upon the surface and that the two rotational degrees of freedom located about axes in the plane of the ring have become torsional vibrational modes of freedom.

As before in the case of vibrational degrees of freedom, we use the harmonic oscillator approximation (VI-22) to obtain

$$q^{s}_{vib\text{-}tv} = \prod_{tv=1}^{2} \frac{e^{-h\nu_{tv}/2kT}}{1 - e^{-h\nu_{tv}/kT}} \qquad \text{(VI-30)}$$

where $q^{s}_{vib\text{-}tv}$ is the molecular partition function for the torsional vibrational degrees of freedom of the adsorbed benzene molecule. We will also assume that the two torsional vibrations have equal frequencies. This gives

$$\frac{q^{s}_{int}}{q^{g}_{int}} = \frac{\sigma^{g}_{C_6H_6}}{\sigma^{s}_{C_6H_6}} \left(\frac{8\pi^2 I_A kT}{h^2}\right)^{-\frac{1}{2}} \left(\frac{8\pi^2 I_B kT}{h^2}\right)^{-\frac{1}{2}} \left[\prod_{tv=1}^{2} \frac{e^{-h\nu_{tv}/2kT}}{1 - e^{-h\nu_{tv}/kT}}\right] \qquad \text{(VI-31)}$$

and inserting (VI-31) into (VI-25) yields

$$\frac{\theta}{1 - \theta} = \left\{\left[\frac{h^3}{(2\pi m)^{3/2}(kT)^{5/2}}\right]\left[\left(\frac{e^{-h\nu_s/2kT}}{1-e^{-h\nu_s/kT}}\right)^3\right]\left[\left(\frac{h^2}{4\pi^2 IkT}\right)\right]\right. \qquad \text{(VI-32)}$$

$$\left(\frac{e^{-h\nu_{tv}/2kT}}{1-e^{-h\nu_{tv}/kT}}\right)^2\left[\exp\left(\frac{Q}{kT}\right)\right]\Bigg\}^P$$

The entire quantity in braces is the constant b in Equation (VI-1). We can see that b is a function of the temperature, T, and of the energy, Q. In our calculation of site energy distributions, we will find b values from experimental data and will use the relationship

$$b = b^{\circ}\exp\left(\frac{Q}{kT}\right) \qquad \text{(VI-33)}$$

to find the energy of the sites. Thus, for benzene we need to evaluate b°, which from Equation (VI-32) we can see is simply

$$b^{\circ} = \left\{\left[\frac{h^3}{(2\pi m)^{3/2}(kT)^{5/2}}\right]\left[\left(\frac{e^{-h\nu_s/2kT}}{1-e^{-h\nu/kT}}\right)^3\right]\right. \qquad \text{(VI-34)}$$

$$\left.\left(\frac{h^2}{4\pi^2 IkT}\right)\left(\frac{e^{-h\nu_{tv}/2kT}}{1-e^{-h\nu_{tv}/kT}}\right)\right]\Bigg\}.$$

Evaluation of b° for Benzene-- Localized Harmonic Oscillator Model

The mass of the benzene molecule, m was found using the following values for the molecular weight of carbon, M_C, the molecular weight of hydrogen, M_H, and Avogadro's number, N_A:

M_C = 12.01 g $mole^{-1}$, the molecular weight of carbon (66).

M_H = 1.008 g $mole^{-1}$, the molecular weight of hydrogen (66).

N_A = 6.023 (10^{23}) $mole^{-1}$ (67) is Avogadro's number.

The value used for Planck's constant h was 6.626 (10^{-27}) erg sec (67), and the value used for the Boltzmann constant, k, was 1.381 (10^{-16}) erg/°K molecule (67).

The three moments of inertia for benzene, I_A, I_B and I_C used were those given by Pitzer and Scott (68). These values were compared to those calculated using bond lengths from X-ray data (69) and were

$$I_A = I_B = 1.453\ (10^{-38})\ gcm^2$$

$$I_C = 2.906\ (10^{-38})\ gcm^2 \qquad \text{(VI-35)}$$

The only quantities remaining in our expression for b° are the vibrational frequencies of the adsorbed benzene molecule ν_s and ν_{tv}. These frequencies will be obtained from the changes in entropy upon going from the gas to the adsorbed phase.

Before beginning an evaluation of entropy changes we must define our reference states. There are several reference states which can be chosen for the adsorbed phase (70); however, the one chosen in this study for the adsorbed phase is temperature T and θ = 0.5, as is recommended by Ross and Olivier (71). The reference state chosen for the gas phase was temperature T and 1 atmosphere pressure.

We now need to develop an equation to determine a vibrational frequency from a gain in entropy. The vibrational partition function for a harmonic oscillator with n degrees of vibrational freedom is given by

$$q(T) = \prod_{i=1}^{n} \frac{\exp(-h\nu_i/2kT)}{1 - \exp(-h\nu_i/kT)} . \qquad \text{(VI-36)}$$

This partition function yields

$$S_{vib} = \sum_{i=1}^{n} \left\{ \frac{Nk}{\exp(h\nu_i/kT-1)} \left(\frac{h\nu_i}{kT}\right) - Nk\ln[1-\exp(-h\nu_i/kT)] \right\} \qquad \text{(VI-37)}$$

which may be solved by an iterative procedure to obtain a vibrational frequency ν_i from an entropy S as described by DeBoer (72).

The first vibrational frequency we will determine will be that of the torsional vibrations. The torsional vibrations arise from three degrees of rotational freedom in the gas phase going to one degree of rotational freedom and two torsional vibrations as described earlier. Thus we will say

$$S^{s}_{tv} = -\Delta S_{rot} = S^{g}_{rot} - S^{s}_{rot}, \qquad \text{(VI-38)}$$

that is, the entropy gained by the benzene molecule attributable to torsional vibrations can be found by taking the difference of the rotational entropy of the gas phase and the rotational entropy of the

adsorbed phase at standard conditions. Using the molecular partition functions q^{g}_{rot} (Equation (VI-27)) and q^{s}_{rot} (Equation (VI-29)) in the following equations:

$$S^{g}_{rot} = NkT\left(\frac{\partial \ln q^{g}_{rot}(T)}{\partial T}\right)_{V,N} + Nk\ln[q^{g}_{rot}(T)] \qquad \text{(VI-39)}$$

$$S^{s}_{rot} = NkT\left(\frac{\partial \ln q^{s}_{rot}(T)}{\partial T}\right)_{V,N} + Nk\ln[q^{s}_{rot}(T)] \qquad \text{(VI-40)}$$

yields

$$S^{s}_{tv} = Nk\left[\ln\left(\frac{4\pi^2 Ik}{h^2}\right) + \ln T + 1\right] \qquad \text{(VI-41)}$$

Remembering that we are dividing this between two degrees of torsional vibrational freedom yields the values of ν_{tv} given in Table 5.

The next vibrational frequency we will evaluate is the frequency of the three vibrational degrees of freedom which arise from the loss of three translational degrees of freedom. We have called this frequency ν_s, and have assumed (for lack of a reasonable alternative) that this frequency is the same for the vibration normal to the surface (ν_z) as it is for vibrations in the plane of the surface (ν_x and ν_y). To evaluate this frequency using Equation (VI-37) we need to know $-\Delta S_{trans}$, which is the change in entropy going from the gas standard state to the adsorbed standard state. In this model of localized adsorption there

is no contribution of the entropy of translation from the adsorbed phase; thus ΔS_{trans} will be equal to S^{g}_{trans}.

The quantity S^{g}_{trans} may be found from the molecular partition function for the translation of an ideal polyatomic gas

$$q^{g}_{trans}(T) = \left(\frac{2\pi mkT}{h^2}\right)^{3/2} V \qquad \text{(VI-42)}$$

using

$$S^{g}_{trans} = NkT\left[\frac{\ln[q^{g}_{trans}(T)]}{T}\right]_{V,N} + Nkln[q^{g}_{trans}] - NklnN + NK. \qquad \text{(VI-43)}$$

Performing the indicated operations yields

$$\Delta S_{trans} = S^{g}_{trans} = Nkln\left(\frac{2\pi mkT}{h^2}\right)^{3/2}\left(\frac{kTe^{5/2}}{P}\right) \qquad \text{(VI-44)}$$

We now can evaluate ΔS^{s}_{vib} using

$$\Delta S_{vib} = \Delta S_{exp} - \Delta S_{trans} - \Delta S_{rot} \qquad \text{(VI-45)}$$

The values obtained for S^{s}_{vib} can be found in Table 6 along with the vibrational frequency ν_s obtained from Equation (VI-37).

Localized Particle-in-a-Box Model

When discussing localized Langmuir adsorption, we assumed that the three degrees of translational freedom in the gas phase were con-

Table 6. Localized Monolayer--Harmonic Oscillator Model Parameters, Entropies and Vibrational Frequencies for Benzene on TiC-8

T°K	273.34	268.11	263.01	258.62	251.73
$(.5)V_m\left(\frac{\text{micromoles}}{g}\right)$	10.22	10.11	10.06	9.92	9.86
$P(\text{torr})_{@\Theta=.5}$	.0364	.0240	.0157	.0101	.0052
$\phi_{@\Theta=.5}(\text{erg/cm}^2)$	7.122	7.179	7.267	6.989	6.922
$\sigma@(.5)V_M\left(\frac{\text{Å}^2}{\text{molecule}}\right)$	112.3	113.4	114.0	115.7	116.3
$\Delta\bar{H}$(kcal/mole)	11.64	11.63	11.62	11.65	11.65
$-\Delta\bar{S}^{\circ}$(cal/moledeg)	42.57	43.37	44.17	45.06	46.29
$-\Delta\bar{S}_{rot}$(cal/moledeg)	17.09	17.05	17.01	16.98	16.93
$-\Delta\bar{S}_{trans}$(cal/moledeg)	16.08	15.96	15.85	15.75	15.59
$\Delta\bar{S}_{vib}$(cal/moledeg)	9.40	10.63	11.31	12.33	13.77
$\nu_{tv}(\text{sec}^{-1})(10^{11})$	2.103	2.081	2.061	2.043	2.014
$\nu_s(\text{sec}^{-1})(10^{11})$	32.43	25.76	22.50	18.63	14.17
$b^{\circ}(\text{cm}^2/\text{dyne})(10^{12})$	1.150	2.318	3.418	6.649	13.72

verted to three degrees of vibrational freedom in the adsorbed phase. When considering mobile adsorption we assume that the three degrees of translational freedom present in the gas phase are converted into two degrees of translational freedom (in a two-dimensional box of length $a^2 = \sigma_o$, where σ_o is the area of an adsorption site), and one degree of vibrational freedom of the adsorbed molecule normal to the surface.

Thus Equation (VI-18) becomes

$$q^s = \underset{\sigma_o \text{box}}{q^s_{\text{trans}}} q^s_{\text{vib-z}} q^s_{\text{int}} \exp\left(\frac{Q}{kT}\right) \qquad \text{(VI-46)}$$

and in two dimensions

$$\underset{\sigma_o \text{box}}{q_{\text{trans}}} = \left(\frac{2\pi mkT}{h^2}\right)\sigma_o . \qquad \text{(VI-47)}$$

We again use the harmonic oscillator approximation (VI-23) to evaluate $q^s_{\text{vib-z}}$

$$q^s_{\text{vib-z}} = \frac{e^{-h\nu_z/2kT}}{1 - e^{-h\nu_z/kT}} , \qquad \text{(VI-48)}$$

and thus we have for benzene with three translational degrees of freedom going, two translational degrees of freedom on the surface and one vibrational degree of freedom.

$$\frac{\theta}{1 - \theta} = \left\{\left(\frac{h^2}{2\pi mkT}\right)^{1/2} \frac{P\sigma_o}{kT} \left[\frac{e^{-h\nu_z/2kT}}{1 - e^{-h\nu_z/kT}}\right] \exp\left(\frac{Q}{kT}\right)\right\} \frac{q^s_{\text{int}}}{q^g_{\text{int}}} \qquad \text{(VI-49)}$$

The ratio q^s_{int}/q^g_{int} remains the same as in the localized case and is given by Equation (VI-31). Substituting (VI-31) into Equation (VI-49) yields

$$\frac{\theta}{1-\theta} = \left\{\left(\frac{h^2}{2\pi mkT}\right)^{\frac{1}{2}} \frac{P\sigma_o}{kT}\left[\frac{e^{-h\nu_z/2kT}}{1-e^{-h\nu_z/kT}}\right]\exp\left(\frac{Q}{kT}\right)\right\} \tag{VI-50}$$

$$\left\{\frac{\sigma^g_{C_6H_6}}{\sigma^s_{C_6H_6}}\left(\frac{8\pi^2 I_A kT}{h^2}\right)^{-\frac{1}{2}}\left(\frac{8\pi^2 I_B kT}{h^2}\right)^{-\frac{1}{2}}\left[\prod_{tv=1}^{2}\frac{e^{-h\nu_{tv}/2kT}}{1-e^{-h\nu_{tv}/kT}}\right]\right\}$$

We now make the important assumption that the energy going from the loss of two translational and two rotational degrees of freedom is equally divided among the three new vibrations and arrives at

$$\frac{\theta}{1-\theta} = \left\{\left(\frac{h^2}{2\pi mkT}\right)^{\frac{1}{2}}\left(\frac{\sigma_o}{kT}\right)\left(\frac{h^2}{4\pi^2 IkT}\right)\left(\frac{e^{h\nu/2kT}}{e^{h\nu/kT}-1}\right)^3 e^{Q/RT}\right\} P \tag{VI-51}$$

Evaluation of b^o for Benzene-- Particle-in-a-Box Model

By comparing Equation (VI-51) with Equations (VI-32) and (VI-33) we see that

$$b^o = \left(\frac{h^2}{2\pi mkT}\right)^{\frac{1}{2}}\left(\frac{\sigma_o}{kT}\right)\left(\frac{h^2}{4\pi^2 IkT}\right)\left(\frac{e^{h\nu/2kT}}{e^{h\nu/kT}-1}\right)^3 . \tag{VI-52}$$

All the variables in the above equation are easily calculated as described earlier, except for the vibrational frequency ν. At the present time no data exist to calculate values of the vibrational frequency of the adsorbed molecule ν, so it must be estimated. This procedure is more straightforward than for the harmonic oscillator model discussed earlier. This is done by assuming that the difference between the experimental entropy change and that calculated for the translational and rotational losses, is due to the vibrational contributions, i.e.

$$\Delta S_{vib} = \Delta S_{exp} - \Delta S_{trans} - \Delta S_{rot}. \qquad \text{(VI-53)}$$

We also need to assume that the total entropy of vibration is equally divided among the three modes of vibration; thus we take $1/3\ \Delta S_{vib}$ and use it in solving the following equation, as described earlier by an iterative procedure to obtain ν.

$$\Delta S_{vib} = \frac{Nk}{e^{h\nu/kT} - 1}\left(\frac{h\nu}{kT}\right) - Nk\ln(1-e^{-h\nu/kT}) \qquad \text{(VI-54)}$$

To evaluate the entropy changes due to translational and rotational degrees of freedom from the partition functions, the following relationship was used

$$S = kT\left(\frac{\partial \ln Q}{\partial T}\right)_{V,N} + k\ln Q. \qquad \text{(VI-55)}$$

Employing the molecular partition functions given in the previous section gives the following expressions for the change in translational entropy, ΔS_{trans}, and the change in rotational entropy, ΔS_{rot}.

$$-\Delta S_{trans} = S^{g}_{trans} - S^{s}_{trans} \qquad \text{(VI-56)}$$

$$-\Delta S_{trans} = Nk\left\{\ln\left[\frac{2\pi Mk}{h^2}\right]^{\frac{1}{2}} + \ln\left(\frac{\bar{V}}{\sigma}\right) + \tfrac{1}{2}\ln T + \tfrac{1}{2}\right\} \qquad \text{(VI-57)}$$

where M is the molecular weight of benzene and $\bar{V}$ is its molar volume.

For the entropy change due to translational degrees of freedom, we have the following as described earlier,

$$-\Delta S_{rot} = S^{g}_{rot} - S^{s}_{rot} \qquad \text{(VI-58)}$$

$$-\Delta S_{rot} = Nk\left[\ln\left(\frac{4\pi^2 I_C k}{h^2}\right) + \ln T + 1\right] \qquad \text{(VI-59)}$$

The parameters and results can be found in Table 7.

The possibility of using the frequency of vibrations normal to the surface obtained for the particle-in-a-box model to calculate the b° values of the harmonic oscillator model was investigated. As can be seen from Tables 6 and 7, the two values found for this frequency are very close and the b° values calculated by swapping this frequency lie in between those found for each of the models. This approach proved to be unsatisfactory for computing the site energy distributions and since

Table 7. Localized Monolayer--Particle-in-a-Box Model Parameters, Entropies, and Vibrational Frequencies for Benzene on TiC-8

T(°K)	273.34	268.11	263.01	258.62	251.73
$(.5)V_M\left(\frac{\text{micromoles}}{g}\right)$	10.22	10.11	10.06	9.92	9.86
$P(\text{torr})_{@\theta=.5}$	.0364	.0240	.0157	.0101	.0052
$\phi_{@\theta=.5}(\text{erg/cm}^2)$	7.122	7.177	7.267	6.989	6.922
$@(.5)V_M\left(\frac{\text{Å}^2}{\text{molecule}}\right)$	112.3	113.4	114.0	115.7	116.3
$\Delta\bar{H}$(kcal/mole)	11.64	11.63	11.62	11.65	11.65
$-\Delta\bar{S}^\circ$(cal/moledeg)	42.57	43.37	44.17	45.06	46.29
$-\Delta\bar{S}_{rot}$	17.09	17.05	17.01	16.98	16.93
$-\Delta\bar{S}_{trans}$	16.75	16.71	16.68	16.63	16.60
$\Delta\bar{S}_{vib}$	8.73	9.61	10.48	11.45	12.77
$\nu(\text{sec}^{-1})(10^{11})$	36.40	30.69	25.94	21.62	16.82
$b^\circ(\text{cm}^2/\text{dyne})(10^{12})$	3.377	4.990	7.415	11.65	21.92

it does not correspond to any well-designed model, it will not be discussed further. The differences in the results for the vibrational entropy, S_{vib}, between the harmonic oscillator model and the particle-in-a-box model amounts to only about 1 cal moledeg. This difference arises because of the way in which the translational entropy is treated in each model. The values obtained for the various vibrational frequencies associated with each model are all reasonable numbers and since there are no experimental data on the frequencies of adsorbed benzene molecules to compare these numbers to, we must rely upon our site energy distribution functions to indicate the more correct model.

Langmuir Equation with Lateral Interactions

It is very easy to include provisions for lateral interactions between the adsorbed molecules into the framework provided by the Langmuir equation by modifying the expression for the molecular partition function for the adsorbed state. From Equation (VI-4) of the previous section

$$q^s = q^s_{site} q^s_{int} e^{Q/kT} \qquad \text{(VI-60)}$$

we see that we have used Q as the energy of adsorption. To this energy we must add a quantity of energy ω which corresponds to the lateral interaction energy.

The quantity ω, however, must be multiplied by the number of nearest neighbor sites Z, and by N/S, which is the probability of a nearest neighbor site being filled. The entire quantity $Z(N/S)\omega$ must

now be divided by two since the neighbors must interact pairwise. This approach assumes a completely random distribution of the adsorbed molecules in the monolayer, which is a crude approximation at best, but does greatly simplify the calculations (73). Thus we have

$$E_{ads} = Q + \frac{Z(N/S)\omega}{2} \qquad \text{(VI-61)}$$

as the energy of adsorption and Equation (VI-4) becomes

$$q^s = q^s_{site} q^s_{int} \exp\left(\frac{Q + \frac{Z(N/S)}{2}}{kT}\right). \qquad \text{(VI-62)}$$

The derivation proceeds as before and we arrive at an analogous Equation (VI-49)

$$\frac{\theta}{1 - \theta} = \left\{\left(\frac{h^2}{2\pi mkT}\right)^{3/2}\left(\frac{P\sigma_o}{kT}\right)\left[\prod_{i=1}^{1} \frac{e^{h\nu_z/2kT}}{e^{h\nu_z/kT} - 1}\right] e^{\alpha/kT}\right\} \frac{q^s_{int}}{q^g_{int}}. \qquad \text{(VI-63)}$$

where we have made the substitution

$$\alpha = Q + \frac{Z\theta\omega}{2} \qquad \text{(VI-64)}$$

In the case of argon q^s_{int}/q^g_{int} is equal to 1 since there are no vibrational or rotational degrees of freedom to consider. We now have

$$\frac{\theta}{1-\theta} = \left\{ \left(\frac{h^2}{2\pi mkT} \right)^{\frac{1}{2}} \left(\frac{\sigma_o}{kT} \right) \left[\frac{e^{h\nu_z/2kT}}{e^{h\nu_z/kT} - 1} \right] e^{\alpha/kT} \right\} > P \qquad \text{(VI-65)}$$

The vibrational frequency of the argon atom normal to the surface, ν_z, was chosen as $10^{13}\,sec^{-1}$. This value corresponds to $1/\tau_o$, where τ_o is Frenkel's characteristic adsorption time (2). From our studies on benzene adsorption we see that $10^{13}\,sec^{-1}$ is not a totally unrealistic choice for ν_z for argon since most vibrational frequencies found for benzene adsorption are of the order of magnitude of 10^{11} and $10^{12}\,sec^{-1}$ and we would expect the vibrational frequency for argon adsorption to be at least an order of magnitude higher because of the much smaller mass of the argon atom.

Calculation of Site Energy Distributions

The calculation of the site energy distribution followed closely the procedure described by Adamson and Ling (2). The surface of the TiC-8 was assumed to consist of noninteracting regions which are homogeneous in nature and which obeyed a local adsorption isotherm $\theta(P)$. This local adsorption isotherm $\theta(P)$, or more correctly local isotherm function $\theta(P,T,Q)$, where Q indicates the adsorbate-adsorbent interaction energy, was chosen to be the Langmuir equation for benzene adsorption, and the Langmuir plus lateral interaction equation for argon adsorption.

We also let $F(Q)$ be the integral site energy distribution, that is, F is the fraction of the surface whose site energy is equal to or

greater than Q, and we let $f(Q) = dF/dQ$ be the site energy distribution function itself.

We can relate all of these expressions by the integral equation

$$\Theta = \left[\int_0^\infty f(Q)\theta(P,T,Q)dQ\right]_{P,T} \qquad \text{(VI-66)}$$

where the integration is over all energies and employs the site energy distribution function $f(Q)$ and the local isotherm function $\theta(P,T,Q)$.

A straightforward approach to the solution of Equation (VI-66) would be to assume some analytical form for $f(Q)$ and $\theta(P,T,Q)$ which would yield some explicit expression for Θ upon integration. Such approaches have been tried and have yielded expressions for θ containing various adjustable parameters. However, experimental adsorption isotherms can usually be in agreement with several models, and agreement with a particular θ containing adjustable parameters is no proof that the initial assumptions are correct.

Clearly, a more realistic approach would be to determine $f(Q)$ from an assumed $\theta(P,T,Q)$ and the experimental adsorption isotherm Θ. Sips (74) showed how Equation (VI-66) could be solved in principle for an $f(Q)$ provided an analytical expression could be written for Θ. Honig and co-workers (75,76,77) have pursued this further and concluded that only certain expressions for $\theta(P,T,Q)$ and Θ are practical, namely the Langmuir equation for $\theta(P,T,Q)$ and the Fruendlich and Temkin isotherm equations for Θ. Such an approach obviously puts severe

restrictions upon the resultant f(Q) obtained.

Adamson and Ling (1) have taken Equation (VI-66) in an alternate form

$$\theta = \left[\int_0^1 \theta(P,T,Q)dF\right]_{P,T} \qquad \text{(VI-67)}$$

and have provided a method for finding F(Q). The method involves making successive approximations to F(Q) to generate θ using any local isotherm function $\theta(P,T,Q)$. The local isotherm function may be in convenient analytical form such as the Langmuir equation, or may require an iterative solution such as the Langmuir plus lateral interactions equation.

The experimental isotherm $\theta(P)$ was first plotted as θ vs $\log_{10}(1/P)$ for benzene where the Langmuir equation was used as $\theta(P,T,Q)$, and as θ vs $\log_{10}\left(\frac{RT}{\alpha P}\right)$ for argon adsorption using the Langmuir plus the lateral interaction equation as the local isotherm function. Only the submonolayer region of adsorption was considered in making these plots. The coverages were corrected for multiplayer effects by using the relationship $\theta = \theta_{exp}(1-p/p^{\circ})$ [as suggested by Adamson (2)] where p is the pressure at which the coverage is θ_{exp} and p° is the equilibrium vapor pressure of the bulk adsorbate at the temperature of the isotherm. This correction was very small and never exceeded 3% of θ_{exp}. This was the first approximation to the F vs Q plot since $\log_{10}(1/P) \simeq \log_{10}(b)$ which is directly related to Q in the Langmuir case. This plot was used to obtain a first approximation for F as a function of Q. Values

of F were then read off the plot along with their associated Q values, and these allowed the calculation of θ as a function of F at a given pressure. The area under the plot of θ vs F was then calculated using a Simpson's rule integration and this gave a calculated θ for that pressure. The calculations of θ and the Simpson's rule area using 20 intervals were performed on a Burroughs B5500 computer, and the resultant plots were made on large pieces of K&E graph paper. Increasing the number of intervals to 30 produced only a 0.1% change in the resultant θ which was not viewed as being significantly better, considering the additional computation time required.

The calculated θ values, θ_{CALCD} usually differed from the experimental θ values for the various pressures. For each θ_{CALCD}, a second approximation to F was made using

$$F_2 = \frac{F_1 \theta_{EXP}}{\theta_{CALCD}} . \qquad \text{(VI-68)}$$

The entire procedure was then repeated using a plot of F_2 vs Q. In all cases five successive approximations were used to obtain the final F vs Q plot. The plot of f(Q) vs Q was then obtained by taking the slope of the F vs Q plot, using increments of 0.05 on the $\log_{10}(b)$ axis. Using the procedure described earlier, b^o values were calculated for both the harmonic-oscillator and particle-in-a-box model of the Langmuir equation. These b^o's were then used to calculate the value of Q for the site energy distribution curves. The b^o values for the harmonic oscillator model does not yield a self-consistent set of site

energy distribution plots. The distributions determined at each temperature were shifted along the energy axis and did not superimpose. Clearly, it would not be possible to postulate a set of circumstances where the distribution of site energies of an adsorbent as inert as TiC would be temperature dependent.

Using b^{o} values for the particle-in-a-box model, we obtained a set of site energy distribution curves which were superimposable. This distribution curve is shown in Figure 29. The first peak at about 11.1 kcal/mole is quite sharp and distinct, whereas the second peak at 12.4 kcal/mole appears to be rising out of some structure, and there even seems to be evidence of another very small peak at about 14 kcal/mole, although this is at very low pressures and the uncertainties involved in this peak are greater. Taking smaller subdivisions when calculating the slopes to obtain f(Q) did not reveal any finer detail.

With the presence of this finer detail in mind, let us look at the site energy distribution curves for argon on TiC-8.

With argon as the adsorbate, the Langmuir equation did not yield a temperature independent site energy distribution. This was taken to be due to an incorrect choice in our local isotherm function, and the Langmuir plus lateral interaction equation was chosen next. Various values of the interaction energy, $z\omega/2$, were tried and the value of

$$\frac{z\omega}{2} = \frac{\Delta H_{vap}}{4} = 4.63 \text{ kcal/mole} \qquad \text{(VI-69)}$$

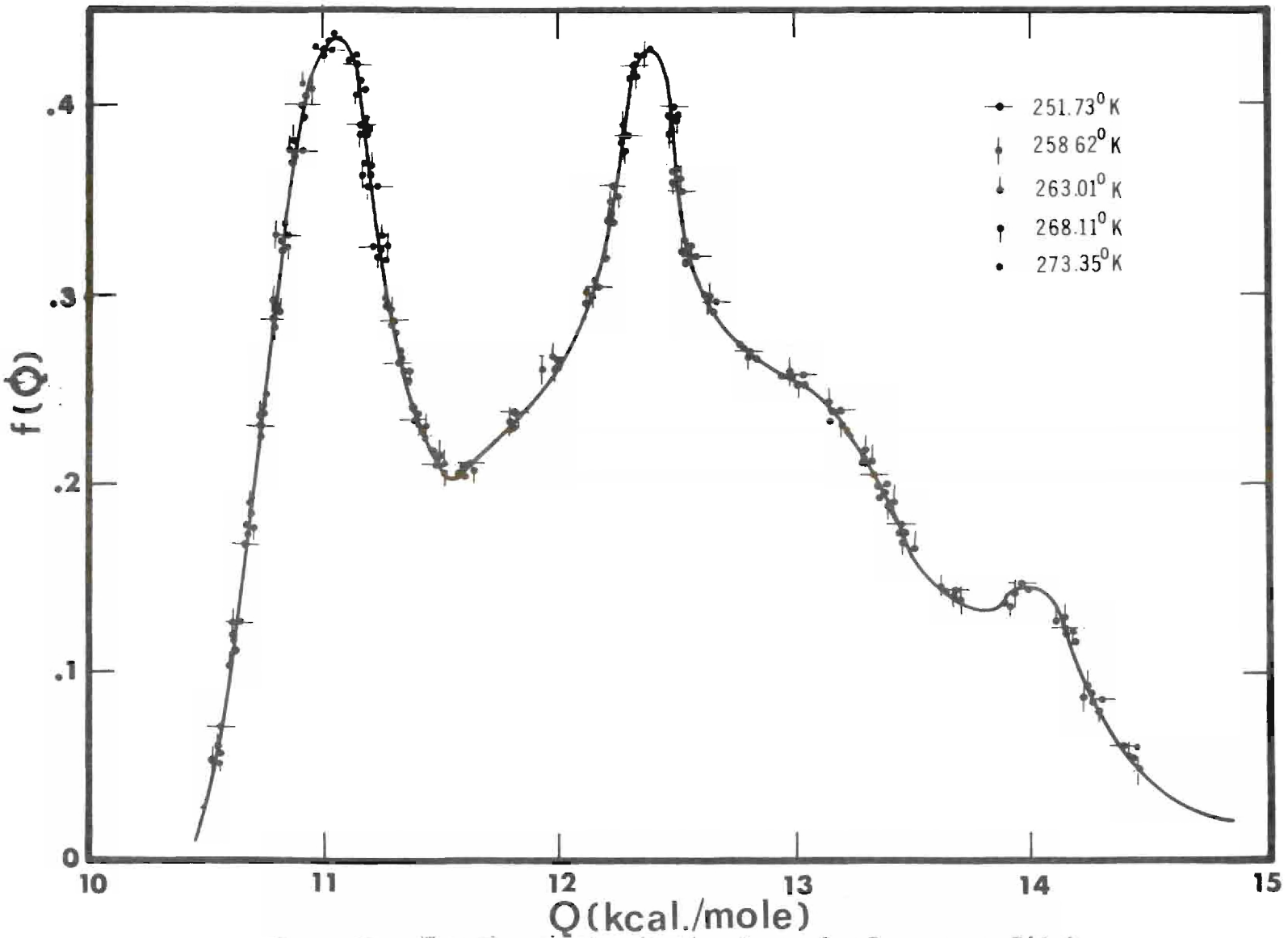

Figure 29. Site Energy Distribution Curve for Benzene on TiC-8

yielded the best set of site energy distributions. This relationship for z /2 is that used by Adamson (2).

The site energy distribution curve for argon on TiC-8 yielded all the structure desired, as is shown in Figure 30. Each of the four peaks is sharp and definite, and clearly reveals that there are most likely four surfaces involved in the adsorption process.

The site energy distribution for Ar on TiC-8 (Figure 30) can be compared to the site energy distribution for Ar on a graphitized carbon black MT-3100 (Figure 31) found by Hseih (4). The MT-3100 shows only one energy site at around 2.7 kcal/mole. TiC-8 exhibits a sharp peak at about 2.74 kcal/mole; it is not known if this could be attributed to the same type of crystal face.

Thus, the site energy distribution curves do not answer all the questions we may have about the nature of the TiC-8 surface, but they do yield some information. In going from graphitized carbon to titanium carbide, we have radically altered the surface. The isosteric heats of adsorption are very different from those found on graphitized carbon and suggest that the TiC-8 surface is composed of patches of different energies. This is borne out by the site energy distribution curves which show (in the case of argon) four distinct types of surfaces. The site energy distributions also show that a Langmuir isotherm with lateral interactions provides the best fit as far as local isotherm equations are concerned.

In the case of benzene we have found a rather strange distribution curve. The broadness of the second peak seems to indicate that

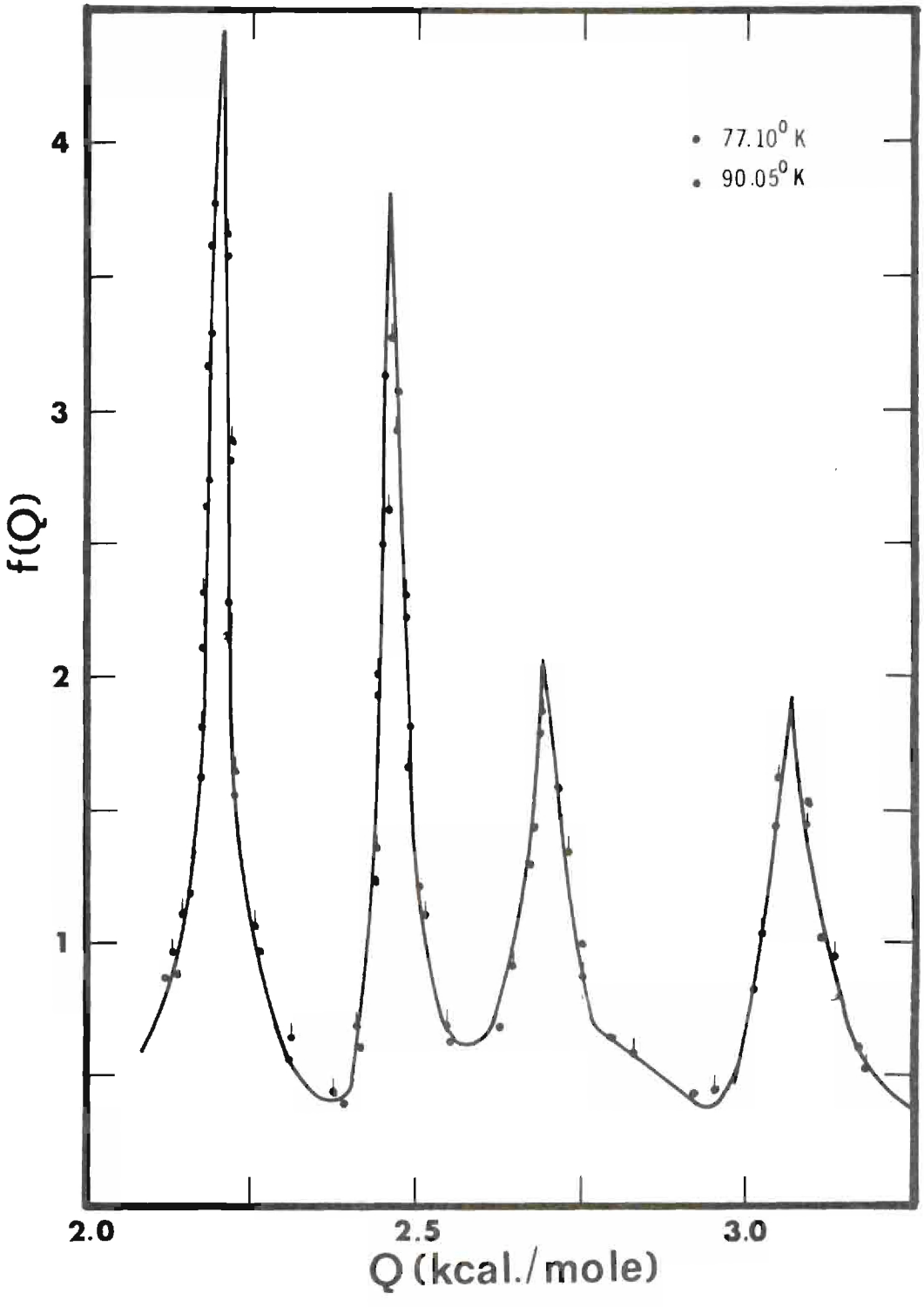

Figure 30. Site Energy Distribution Curve for Argon on TiC-8

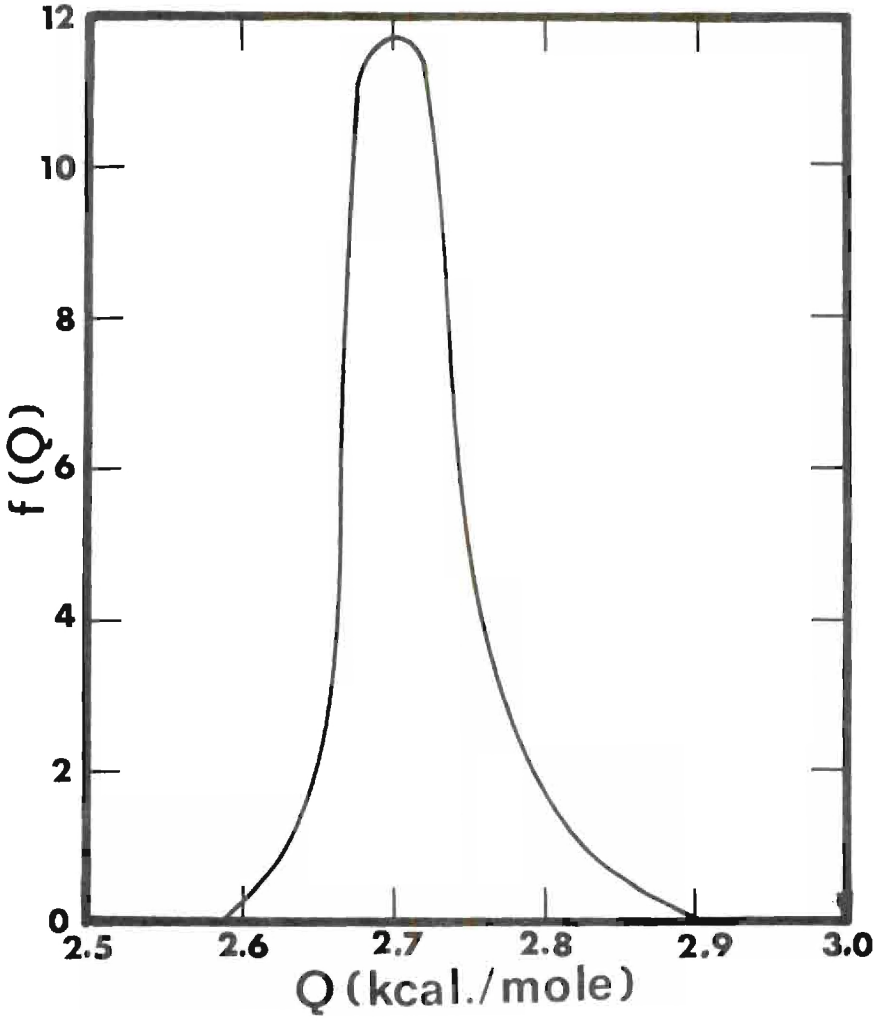

Figure 31. Site Energy Distribution Curve for Argon on MT-3100

the large area of the benzene molecule is perhaps covering several types of adsorption sites simultaneously. However, it was found that the benzene adsorption obeys a local isotherm where the molecule is free to translate within the confines of a two-dimensional box on the surface. We have called this the particle-in-a-box Langmuir model.

CHAPTER VII

CONCLUSIONS AND RECOMMENDATIONS

Conclusions

The volumetric adsorption apparatus constructed for use in this study proved to be well suited for investigating the physical adsorption of gases on titanium carbide. The cryostat used for studying benzene adsorption performed very well in the range of 251-268°K and has design capabilities for a much wider range. The technique of using a copper block with a heater to "balance off" a thermoelectric cold plate provides a very good method of obtaining this range of temperatures.

Using the synthesis described earlier in this work, we have shown that a stoichiometric transition metal carbide can be prepared in a pure form from a metal hydride and carbon. The titanium carbide prepared for this study proved to be unique in that all adsorption data indicated that we were not dealing with a single isoenergetic surface. In an effort to obtain at least a qualitative view of the energetics of the surface a semi-empirical method described by Adamson and co-workers (1,2) was employed to determine site energy distribution functions. Analysis of the experimental data for argon using this approach indicates that the surface is composed of perhaps as many as four types of adsorption sites. The same analysis procedure used on the benzene data indicates that perhaps two types of sites are covered by a single

benzene molecule; thus yielding a site energy distribution curve which indicates only two types of adsorption sites.

Recommendations

What remains to be done in the way of future research in this area is clear. There are many more carbides which can be synthesized from graphitized carbon black, using the procedure outlined here, and many transition metal nitrides which can be studied. Energies of interaction of adsorbates with the vast array or possible crystal faces formed, can be calculated. Low energy electron diffraction (LEED) studies on the TiC-8 surface would be of inestimable importance in determining which crystallographic planes bound the surface. It would be very interesting to see if LEED would reveal four different surfaces, or if it would reveal that our site energy distribution is due to only three surfaces plus cracks.

APPENDIX A

APPENDIX A

The Antoine Equation

The Antoine equation

$$\log_{10} p = A - \frac{B}{C + T} \qquad \text{(A-1)}$$

was used to convert measured pressures to temperatures. In Equation (A-1) p is in torr, T in °C and A, B and C are constants. Equation (A-1) was also used to convert measured (or calculated) temperatures to adsorbate vapor pressures.

The values of the constants A, B, C in Equation (A-1) were obtained from Table K of the American Petroleum Institute Research Project 44 series, and can be found in Table 8.

Correction of Mercury Column Heights

When measuring mercury column heights and converting the results to units of torr, the measured heights must be corrected for the thermal expansion of mercury, and for gravitational effects. The standard temperature is 0°C and the standard value of g_o, the standard acceleration of gravity is 980.665 cm/sec^2, and p_o, the density of mercury at 0°C and one atmosphere is given as 13.5955 g/cm^3 (78). The effects of pressure and isotopes were neglected. The latter effect was kept to a minimum by using triply-distilled mercury and making every effort to maintain a clean system.

Table 8. Antoine Constants

Substance	State	A	B	C
N_2	Liquid	6.49457	255.680	266.550
Ar	Liquid	6.61651	304.227	267.320
	Solid	7.50581	399.085	272.630
CH_4	Solid	7.69540	532.20	275.00
C_6H_6	Solid	9.1064	1885.9	244.2
O_2	Liquid	6.69144	319.013	266.697
CO_2	Solid	9.81066	1347.786	273.00
2,2,dimethylpropane	Liquid	6.73812	950.84	237.00

The following equation was used to correct the mercury column heights

$$h_o = h - h\left[\frac{P_o - p(T)}{P_o} + \frac{g_o - g}{g_o}\right] \qquad (A\text{-}2)$$

where h_o is the corrected height of the mercury column, h is the measured height of the mercury column at temperature T, p(T) is the density of mercury at temperature T as given by the 45*th* edition of the Chemical Rubber Handbook (78), g is the acceleration due to gravity at the manometer and p_o and g_o are as described previously. The value of g,

measured on the Georgia Institute of Technology campus, was taken as 979.5283 cm/sec^2 (79).

APPENDIX B

ADSORPTION DATA

Tabulated as amount adsorbed (in micromoles) per gram vs equilibrium pressure in torr.

Table 9. C_6H_6—TiC-8 Isotherm at 273.35°K

N_{ADS}/W (micromoles/g)	P_f (torr)	N_{ADS}/W (micromoles/g)	P_f (torr)	N_{ADS}/W (micromoles/g)	P_f (torr)
2.45	.00165	14.90	.190	26.22	3.02
3.12	.00228	15.54	.224	28.44	3.61
3.77	.00337	16.21	.293	29.60	4.07
4.34	.00465	16.56	.330	30.72	4.46
5.07	.00606	17.03	.367	30.90	4.57
5.67	.00774	17.57	.447	32.92	5.42
6.50	.0105	17.96	.497	35.01	6.06
7.01	.0129	18.30	.567	37.18	6.80
7.84	.0172	18.58	.624	40.43	7.92
8.58	.0228	18.80	.676	43.42	8.86
9.28	.0270	19.11	.737	47.32	10.04
10.03	.0357	19.60	.818	51.29	11.45
10.87	.0446	20.02	.910	55.40	12.90
11.58	.0568	20.42	.989	60.68	14.77
12.17	.0675	20.82	1.11	66.02	16.52
12.62	.0809	21.38	1.29	71.29	18.31
13.13	.0959	21.66	1.42	77.35	18.74
13.67	.112	22.46	1.63	78.99	20.21
13.74	.123	23.10	1.77	81.26	21.61
14.30	.142	24.39	2.19	84.72	22.19
14.74	.178	25.42	2.57		

Table 10. C_6H_6—TiC-8 Isotherm at 268.11°K

N_{ADS}/W (micromoles/g)	P_f (torr)	N_{ADS}/W (micromoles/g)	P_f (torr)	N_{ADS}/W (micromoles/g)	P_f (torr)
3.06	.00138	15.83	.209	30.72	3.37
4.17	.00250	16.25	.242	31.67	3.59
4.62	.00318	16.93	.306	33.76	4.08
5.39	.00458	17.48	.370	36.23	4.65
5.65	.00493	17.62	.384	37.78	4.96
6.60	.00700	18.14	.454	41.62	5.85
6.74	.00743	18.46	.505	43.02	6.19
7.47	.00968	18.97	.585	45.23	6.57
8.49	.0139	19.54	.678	47.51	7.05
8.87	.0157	20.14	.782	49.27	7.44
9.68	.0209	20.54	.876	55.88	8.99
10.35	.0259	20.81	.937	59.62	9.92
10.60	.0285	21.27	1.06	63.38	10.77
11.49	.0381	21.77	1.20	68.82	11.95
12.75	.0592	22.53	1.38	73.60	13.32
13.10	.0697	23.30	1.56	78.99	14.41
13.41	.0805	23.72	1.65	83.37	14.87
13.92	.0963	24.82	1.91		
14.36	.121	25.81	2.14		
14.68	.134	26.92	2.46		
15.34	.174	28.48	2.82		

Table 11. C_6H_6—TiC-8 Isotherm at 263.01°K

N_{ADS}/W (micromoles/g)	P_f (torr)	N_{ADS}/W (micromoles/g)	P_f (torr)	N_{ADS}/W (micromoles/g)	P_f (torr)
3.35	.00096	16.25	.196	37.56	3.53
4.57	.00198	16.99	.251	39.25	3.75
5.44	.00293	17.60	.307	41.70	4.12
5.89	.00349	18.32	.398	44.50	4.51
6.56	.00454	18.51	.423	46.65	4.79
6.85	.00503	19.38	.552	48.25	4.99
7.49	.00628	19.91	.636	49.65	5.21
8.09	.00768	20.60	.773	57.50	6.45
8.60	.00925	21.10	.875	64.20	7.40
8.97	.0105	21.75	1.00	70.90	8.56
9.20	.0116	22.04	1.05	75.90	9.40
10.17	.0161	23.27	1.27	80.90	10.05
10.82	.0209	24.60	1.50		
11.45	.0268	25.85	1.71		
12.15	.0348	27.50	1.96		
12.70	.0432	28.25	2.10		
13.47	.0618	29.55	2.31		
13.80	.0730	30.55	2.45		
14.57	.0985	31.72	2.66		
14.87	.115	33.75	2.95		
15.55	.153	35.51	3.28		

Table 12. C_6H_6—TiC-8 Isotherm at 258.62°K

N_{ADS}/W (micromoles/g)	P_f (torr)	N_{ADS}/W (micromoles/g)	P_f (torr)	N_{ADS}/W (micromoles/g)	P_f (torr)
3.52	.00073	16.12	.157	47.42	3.49
3.92	.00091	16.90	.211	49.31	3.71
4.91	.00149	17.62	.297	52.90	4.10
5.65	.00211	18.41	.358	58.70	4.66
6.30	.00275	18.94	.417	63.40	5.27
6.96	.00347	19.92	.556	70.60	5.90
7.93	.00488	20.25	.609	75.70	6.60
8.24	.00566	21.49	.819		
8.97	.00718	22.92	1.02		
9.86	.00989	23.72	1.13		
10.25	.0128	25.14	1.30		
11.15	.0173	26.17	1.41		
11.72	.0224	27.20	1.57		
12.13	.0261	29.23	1.73		
12.60	.0329	30.40	1.87		
13.05	.0401	32.45	2.08		
13.54	.0491	33.15	2.14		
14.16	.0645	35.41	2.36		
14.62	.0783	38.45	2.67		
14.91	.0928	41.73	3.00		
15.34	.114	43.62	3.18		

Table 13. C_6H_6—TiC-8 Isotherm at 251.73°K

N_{ADS}/W (micromoles/g)	P_f (torr)	N_{ADS}/W (micromoles/g)	P_f (torr)	N_{ADS}/W (micromoles/g)	P_f (torr)
4.13	.00052	16.75	.148	42.05	1.79
5.15	.00086	17.62	.204	44.45	1.92
6.12	.00135	18.07	.235	47.35	2.07
7.19	.00194	18.70	.304	49.60	2.16
7.84	.00250	19.42	.385	51.20	2.27
8.09	.00272	19.92	.438	56.92	2.61
8.80	.00341	20.61	.528	62.51	2.87
9.64	.00472	20.75	.548	67.30	3.19
10.65	.00782	21.82	.680	72.52	3.58
11.62	.0128	22.76	.775	77.30	3.80
12.40	.0187	23.72	.850		
12.57	.0205	24.85	.924		
13.37	.0314	26.01	.982		
13.92	.0404	27.52	1.06		
14.12	.0443	28.25	1.10		
14.67	.0583	30.15	1.20		
14.82	.0640	31.57	1.27		
15.14	.0747	33.73	1.39		
15.25	.0815	35.77	1.46		
15.51	.0941	38.52	1.62		
15.92	.107	39.92	1.69		

Table 14. Ar—TiC-8 Isotherm at 77.08°K

N_{ADS}/W (micromoles/g)	P_f (torr)	N_{ADS}/W (micromoles/g)	P_f (torr)	N_{ADS}/W (micromoles/g)	P_f (torr)
3.09	.00063	49.13	2.44	82.23	36.97
5.47	.00099	49.34	2.88	87.24	42.73
7.47	.00346	50.92	3.65	91.48	47.19
11.13	.0106	53.04	4.90	95.7	51.2
14.21	.0166	53.20	4.81	95.9	51.8
15.86	.0218	53.77	5.30	103.9	59.6
17.76	.0319	54.07	5.70	111.5	66.4
23.56	.0882	57.21	8.24	116.4	69.6
26.45	.141	58.95	9.83	121.7	73.9
31.23	.233	60.91	11.90	137.2	84.2
33.77	.344	61.73	12.82	145.2	92.1
36.66	.481	62.79	14.45	151.8	94.6
38.13	.614	62.80	14.62	152.2	96.6
38.25	.662	63.58	15.63	160.4	102.3
39.98	.815	64.31	16.65	170.2	106.6
40.43	.872	66.36	19.39	170.2	108.1
42.39	1.12	69.67	22.40	178.3	111.6
43.31	1.26	72.73	26.58	188.6	118.3
45.95	1.51	75.79	29.49	195.5	123.0
48.41	2.18	76.92	30.34	205.4	128.6
48.96	2.48	80.20	34.68	211.9	131.6

Table 15. Ar—TiC-8 Isotherm at 77.08°K

N_{ADS}/W (micromoles/g)	P_f (torr)	N_{ADS}/W (micromoles/g)	P_f (torr)	N_{ADS}/W (micromoles/g)	P_f (torr)
217.8	137.8	237.8	158.2	258.7	177.2
219.1	138.3	239.1	159.3	263.7	178.4
225.5	143.8	244.2	166.0	270.7	183.5
226.8	144.8	253.7	171.8	279.8	187.7
229.4	148.5	253.9	173.3	289.9	189.7

Table 16. Ar—TiC-8 Isotherm at 90.05°K

N_{ADS}/W (micromoles/g)	P_f (torr)	N_{ADS}/W (micromoles/g)	P_f (torr)	N_{ADS}/W (micromoles/g)	P_f (torr)
3.84	.0133	31.13	2.84	45 17	16.48
7.14	.0412	32.58	3.52	45.76	17.80
11.32	.0990	34.38	4.40	47.68	21.39
14.78	.188	36.18	5.49	47.80	22.41
16.25	.242	36.91	6.25	48.04	21.93
17.07	.310	37.89	6.95	49.00	24.60
18.11	.372	38.73	7.70	49.45	26.01
19.35	.477	41.13	10.14	50.48	29.17
22.57	.835	43.02	12.41	50.66	30.89
25.06	1.29	43.80	13.68	52.87	38.60
27.13	1.81	44.80	15.52		
28.71	2.29	45.14	16.30		

Table 17. N_2—TiC-8 Isotherm at 77.23°K

N_{ADS}/W (micromoles/g)	P_f (torr)	N_{ADS}/W (micromoles/g)	P_f (torr)	N_{ADS}/W (micromoles/g)	P_f (torr)
30.7	.3	76.5	68.8	106.8	209.5
60.0	8.3	82.4	93.0	115.6	241.6
63.7	15.8	84.7	106.8	123.3	277.1
63.7	16.4	90.5	134.0	124.7	279.1
66.8	25.4	91.4	137.9	134.8	314.6
68.8	34.8	93.5	145.9	139.3	332.4
71.5	43.1	100.3	179.3	140.8	332.8
75.0	58.0	105.9	208.1	148.0	352.6
75.8	65.8	106.8	210.5	149.7	367.9

Table 18. CH_4—TiC-8 Isotherm at 77.10°K

N_{ADS}/W (micromoles/g)	P_f (torr)	N_{ADS}/W (micromoles/g)	P_f (torr)	N_{ADS}/W (micromoles/g)	P_f (torr)
.27	.00017	72.80	.748	172.6	4.79
1.10	.00019	81.35	1.15	189.9	5.82
8.82	.00022	91.56	1.70	202.2	6.91
17.93	.00069	102.2	2.16	215.5	7.78
38.71	.00386	112.9	2.63	213.3	7.55
58.42	.153	124.0	3.04	230.7	8.35
58.70	.160	135.4	3.37	251.7	8.76
59.36	.180	146.6	3.76	286.3	9.00
66.04	.431	157.7	4.16		

APPENDIX C

Table 19. Spreading Pressures for Benzene on TiC-8 at 258.62°K

P (torr)	ϕ (ergs/cm^2)	P (torr)	ϕ (ergs/cm^2)	P (torr)	ϕ (ergs/cm^2)
.0002	.609	.09	15.72	1.10	30.39
.0004	1.080	.10	16.21	1.15	30.72
.0006	1.436	.15	18.57	1.20	31.04
.0008	1.742	.20	20.03	1.25	31.35
.001	2.011	.25	21.22	1.30	31.66
.002	3.143	.30	22.21	1.35	31.95
.003	3.898	.35	23.08	1.40	32.24
.004	4.516	.40	23.85	1.45	32.53
.005	5.045	.45	24.54	1.50	32.81
.006	5.509	.50	25.18	2.0	35.87
.007	5.924	.55	25.76	2.5	38.33
.008	6.301	.60	26.31	3.0	40.46
.009	6.646	.65	26.81	3.5	42.61
.01	6.966	.70	27.29	4.0	44.68
.02	9.535	.75	27.74	4.5	46.69
.03	11.05	.80	28.17	5.0	48.63
.04	12.19	.85	28.58	5.5	50.52
.05	13.12	.90	28.97	6.0	52.37
.06	13.90	.95	29.34	6.5	54.20
.07	14.58	1.00	29.70	7.0	56.04
.08	15.18	1.05	30.05		

Table 20. Spreading Pressures for Benzene on TiC-8 at 273.35°K

P (torr)	ϕ (ergs/cm^2)	P (torr)	ϕ (ergs/cm^2)	P (torr)	ϕ (ergs/cm^2)
.001	.6585	.40	18.45	6.5	40.66
.002	1.236	.50	19.73	7.0	41.55
.003	1.657	.60	20.83	7.5	42.42
.004	2.020	.70	21.78	8.0	43.26
.005	2.343	.80	22.63	8.5	44.08
.006	2.632	.90	23.39	9.0	44.88
.007	2.900	1.0	24.09	9.5	45.67
.008	3.146	1.1	24.73	10.0	46.44
.009	3.367	1.2	25.33	10.5	47.20
.01	3.583	1.3	25.89	11.0	47.95
.02	5.420	1.4	26.42	12.0	49.66
.03	6.612	1.5	26.91	13.0	51.08
.04	7.565	2.0	29.47	14.0	52.47
.05	8.366	2.5	31.27	15.0	53.83
.06	9.058	3.0	32.83	16.0	55.16
.07	9.669	3.5	34.22	17.0	56.47
.08	10.22	4.0	35.48	18.0	57.76
.09	10.71	4.5	36.65	19.0	59.04
.10	11.16	5.0	37.73	20.0	60.30
.20	14.77	5.5	38.76	21.0	61.55
.30	16.86	6.0	39.73	22.0	62.80

Table 21. Spreading Pressures for Benzene on TiC-8 at 268.11°K

P (torr)	ϕ (ergs/cm^2)	P (torr)	ϕ (ergs/cm^2)	P (torr)	ϕ (ergs/cm^2)
.001	1.046	.40	20.39	6.5	44.07
.002	1.805	.50	21.70	7.0	45.16
.003	2.343	.60	22.80	7.5	46.23
.004	2.790	.70	23.77	8.0	47.27
.005	3.180	.80	24.63	8.5	48.30
.006	3.582	.90	25.40	9.0	49.31
.007	3.844	1.0	26.11	9.5	50.31
.008	4.136	1.1	26.77	10.0	51.29
.009	4.407	1.2	27.37	10.5	52.26
.01	4.660	1.3	27.94	11.0	53.21
.02	6.77	1.4	28.48	12.0	55.40
.03	8.110	1.5	28.96	13.0	57.23
.04	9.152	2.0	31.63	14.0	59.01
.05	10.01	2.5	33.51	15.0	60.79
.06	10.75	3.0	35.16		
.07	11.39	3.5	36.66		
.08	11.96	4.0	38.06		
.09	12.48	4.5	39.36		
.10	12.95	5.0	40.61		
.20	16.65	5.5	41.81		
.30	18.78	6.0	42.96		

Table 22. Spreading Pressures for Benzene on TiC-8 at 263.01°K

P (torr)	ϕ (ergs/cm^2)	P (torr)	ϕ (ergs/cm^2)	P (torr)	ϕ (ergs/cm^2)
.001	1.580	.25	19.70	2.0	33.86
.002	2.542	.30	20.69	2.5	35.92
.003	3.186	.35	21.56	3.0	37.79
.004	3.719	.40	22.32	3.5	39.52
.005	4.183	.45	23.01	4.0	41.18
.006	4.592	.50	23.64	4.5	42.77
.007	4.963	.55	24.22	5.0	44.32
.008	5.301	.60	24.76	5.5	45.83
.009	5.613	.65	25.26	6.0	47.29
.01	5.903	.70	25.73	6.5	48.72
.02	8.283	.75	26.18	7.0	50.12
.03	9.727	.80	26.60	7.5	51.49
.04	10.83	.85	27.00	8.0	52.84
.05	11.73	.90	27.38	8.5	54.16
.06	12.49	.95	27.75	9.0	55.46
.07	13.15	1.0	28.10	9.5	56.75
.08	13.74	1.1	28.76	10.0	58.03
.09	14.27	1.2	29.39		
.10	14.75	1.3	29.97		
.15	17.07	1.4	30.53		
.20	18.52	1.5	31.06		

Table 23. Spreading Pressures for Benzene on TiC-8 at 251.73°K

P (torr)	ϕ (ergs/cm^2)	P (torr)	ϕ (ergs/cm^2)	P (torr)	ϕ (ergs/cm^2)
.00010	.655	.04	14.60	.85	31.34
.00012	.752	.05	15.55	.90	31.76
.00014	.842	.06	16.35	.95	32.16
.00016	.928	.07	17.05	1.00	32.56
.00018	1.008	.08	17.66	1.05	32.96
.0002	1.086	.09	18.21	1.10	33.34
.0004	1.794	.10	18.71	1.15	33.73
.0006	2.284	.15	21.10	1.20	34.11
.008	2.685	.20	22.59	1.25	34.48
.001	3.031	.25	23.79	1.30	34.86
.002	4.476	.30	24.81	1.35	35.23
.003	5.445	.35	25.70	1.40	35.59
.004	6.216	.40	26.49	1.45	35.96
.005	6.860	.45	27.20	1.50	36.33
.006	7.410	.50	27.84	2.0	40.50
.007	7.890	.55	28.44	2.5	43.93
.008	8.318	.60	28.99	3.0	47.25
.009	8.703	.65	29.51	3.5	50.43
.01	9.056	.70	30.00	4.0	53.50
.02	11.83	.75	30.46		
.03	13.41	.80	30.91		

Table 24. Isothermal Differential Heats of Adsorption for Benzene on TiC-8

ϕ (ergs/cm^2)	$\Delta\bar{H}$ (kcal/mole)	ϕ (ergs/cm^2)	$\Delta\bar{H}$ (kcal/mole)	ϕ (ergs/cm^2)	$\Delta\bar{H}$ (kcal/mole)
1	13.62	20	9.175	39	7.122
2	13.28	21	9.064	40	7.264
3	12.82	22	8.863	41	7.396
4	12.75	23	8.608	42	7.507
5	12.11	24	8.401	43	7.606
6	11.85	25	8.217	44	7.696
7	11.79	26	8.056	45	7.776
8	11.54	27	7.877	46	7.841
9	11.41	28	7.632	47	7.913
10	11.47	29	7.326	48	8.055
11	11.36	30	7.009	49	8.110
12	10.94	31	6.818	50	8.174
13	10.57	32	6.693	51	8.247
14	10.01	33	6.591	52	8.394
15	9.779	34	6.575	53	8.409
16	9.517	35	6.603	54	8.427
17	9.355	36	6.732	55	8.253
18	9.254	37	6.849		
19	9.123	38	7.017		

Table 25. Isosteric Heats of Adsorption for Argon on TiC-8

N_{ADS}/W (micromoles/g)	q_{st} (kcal/mole)	N_{ADS}/W (micromoles/g)	q_{st} (kcal/mole)
6	3.311	42	2.554
8	2.664	44	2.498
10	2.447	46	2.422
12	2.365	48	2.363
14	2.377	50	2.299
16	2.401	52	2.217
18	2.451	54	2.128
20	2.535	56	2.022
22	2.617	58	1.929
24	2.708	60	1.782
26	2.781	62	1.668
28	2.837	64	1.587
30	2.841	66	1.612
32	2.815	68	1.693
34	2.769	70	1.787
36	2.701	72	1.867
38	2.663	74	1.943
40	2.618	76	2.002

Table 26. Isosteric Heats of Adsorption for Benzene on TiC-8

N_{ADS}/w $\left(\frac{\text{micromoles}}{g}\right)$	q_{st} $\left(\frac{\text{kcal}}{\text{mole}}\right)$	N_{ADS}/W $\left(\frac{\text{micromoles}}{g}\right)$	q_{st} $\left(\frac{\text{kcal}}{\text{mole}}\right)$	N_{ADS}/W $\left(\frac{\text{micromoles}}{g}\right)$	q_{st} $\left(\frac{\text{kcal}}{\text{mole}}\right)$
2	13.91	23	5.193	44	9.997
3	13.38	24	5.636	45	10.02
4	12.83	25	6.057	46	10.11
5	12.25	26	6.468	47	10.12
6	12.00	27	6.902	48	10.25
7	12.18	28	7.297	49	10.24
8	12.31	29	7.657	50	10.37
9	12.13	30	7.986	51	10.31
10	11.48	31	8.284	52	10.45
11	10.14	32	8.519	53	10.46
12	9.004	33	8.737	54	10.56
13	7.968	34	8.950	55	10.52
14	7.371	35	9.153	56	10.59
15	6.440	36	9.331		
16	5.764	37	9.457		
17	4.987	38	9.588		
18	4.713	39	9.665		
19	4.731	40	9.742		
20	4.518	41	9.810		
21	4.584	42	9.876		
22	4.849	43	9.955		

APPENDIX D

APPENDIX D

ERROR ANALYSIS

Temperature

Values reported for the uncertainty associated with the temperature of an isotherm are the average deviations of all temperatures measured for that isotherm from the mean value.

Pressure 50-500 Torr

For all pressures measured in the range of 50-500 torr (using a manometer), the estimated uncertainty is ±0.5 torr.

Pressure 2×10^{-5}-50 Torr

An extensive error analysis was performed on all argon and benzene isotherms. The isotherms were first plotted as N_{ADS}/W vs p on large pieces of graph paper (using a number of different scales) and smooth curves were drawn through the experimental data. The deviations of each point from the smooth curve were then measured on both axes. The following formula was then applied

$$\sigma = \left[\frac{\sum(d)^2}{N - 1}\right]^{\frac{1}{2}} \qquad \text{(D-1)}$$

where σ = the standard deviation.

d = the deviation of the experimental point from the smooth curve.

N = the number of points.

The error limit was then set at two standard deviations. The following are the results for all isotherms.

Pressure Range	2σ (torr)	2σ (N_{ADS}/W)
.01 - .1	±0.001	±0.15
.1 - .5	±0.005	±0.17
.5 - 1.0	±0.01	±0.12
1.0 - 1.5	±0.03	±0.25
1.5 - 6.	±0.05	±0.50
6. - 11.	±0.15	±0.50
11. - 21.	±0.30	±0.37
21. - 50.	±0.50	±0.75

Below 0.01 torr the error is estimated at about 2%.

Isosteric Heats

The range of uncertainty in the isosteric heats can be calculated from the uncertainties in the pressure measurements. These values are

θ	cal/mole	θ	cal/mole
0.25	±275	1.00	±125
0.50	±175	>1.	±150
0.75	±100		

BIBLIOGRAPHY

BIBLIOGRAPHY

1. Adamson, A. W., Ling, I., Dormant, L., and Orem, M., *Journal of Colloid and Interface Science, 21,* 445 (1966).

2. Adamson, A. W., and Ling, I., *Advances in Chemistry Series Number 33,* 51 (1961).

3. Hsieh, P. Y., *Journal of Catalysis, 2,* 211 (1963).

4. Hsieh, P. Y., *Journal of Physical Chemistry, 68,* 1068 (1964).

5. Young, D. M. and Crowell, A. D., "Physical Adsorption of Gases," Butterworths, London (1962) pg. 25; Polley, M. H., Schaeffer, W. D., and Smith, W. R., *Journal of Physical Chemistry, 57,* 469 (1953).

6. Young, D. M. and Crowell, A. D., pages 38 and 42.

7. Morrison, J. A., Los, J. M., and Drain, L. E., *Transactions of the Faraday Society, 47,* 1023 (1951); Drain, L. E., and Morrison, J. A., *ibid. 48,* 316 (1952).

8. Larher, Y., *Journal of Physical Chemistry, 72,* 1847 (1968).

9. Ramsey, R. N., "Interaction of the Inert Gases with Hexagonal Boron Nitride," Doctoral Thesis, Georgia Institute of Technology (1970).

10. Pierotti, R. A. and Halsey, G. D., Jr., *Journal of Physical Chemistry, 63,* 680 (1959).

11. Dormant, L. M. and Adamson, A. W., *Journal of Colloid and Interface Science, 28,* 459 (1968).

12. Westbrook, J. H. and Stover, E. R., in "High Temperature Materials and Technology" (Campbell, I. E. and Shervood, E. M., editors), Wiley, New York (1967), page 312.

13. Kovalskii, A. E. and Makarenko, T. G., *Zhornal Tekh. Fizik,* 23, 265 (1953).

14. Toth, L. E., "Transition Metal Carbides and Nitrides," Academic Press, New York (1971), page 4.

15. Hollox, G. E. and Smallman, R. E., *Journal of Applied Physics, 37,* 818 (1966).

16. Williams, W. S., *Journal of Applied Physics, 35,* 1329 (1964).

17. Adamson, A. W. "Physical Chemistry of Surfaces," Interscience, New York (1960), page 283.

18. Williams, W. S., in "Propriete's Thermodynamiques Physiques et Structurales des Derives Semi-Metalliques," *Colloq. Int. Cent. Nat. Rech. Sci. No. 157 Paris* (1967), page 181.

19. Williams, W. S. and Schaal, R. D., *Journal of Applied Physics, 33,* 955 (1962).

20. Toth, L. E., page 171.

21. Stranski, I. N., *Ber., 75B,* 1667 (1942).

22. Orr, W. J. C., *Proceedings of the Royal Society, A173,* 349 (1939).

23. Hayakawa, T., *Bulletin of the Chemical Society of Japan, 30,* 343 (1957).

24. Kieffer, R. and Schwartzkopf, P., "Hartstoffe und Hartmettale," *Hartmetalle,* Springer, Vienna (1953).

25. Langer, A. W., *Chemical and Engineering News, 50,* 16 (1972).

26. Schwartzkopf, P. and Kieffer, R., *Refractory Hard Metals,* Macmillan, New York (1953).

27. Bleecker, W. H., United States Patent Number 2,849,275 (1958).

28. Storms, E. K., "The Refractory Carbides," Academic Press, New York (1967), page 6.

29. Ogawa, K. and Bando, Y., *Funtai Oyobi Funmatsuyakin, 6,* 160 (1959).

30. Nuffield, E. W., "X-Ray Diffraction Methods," Wiley, New York (1966).

31. Taylor, A. and Sinclair, H. B., *Proceedings of the Physical Society of London, 57,* 126 (1945).

32. Franklin, R. E., *Acta Cryst., 4,* 253 (1951).

33. Andrews, K. W., Dyson, D. J., and Keown, S. R., "Interpretation of Electron Diffraction Patterns," Plenum Press, New York (1971), page 14.

34. Weast, R. C., editor, "Chemical Rubber Handbook, 45th Edition," Chemical Rubber Company, Cleveland (1964), page E76.

35. Smith, J. V., editor, "Fink Inorganic Inded to the Powder Diffraction File," American Society for Testing Materials, Philadelphia (1964).

36. Davis, B. W., and Varsanik, R. G., *Journal of Colloid and Interface Science, 37,* 870 (1971).

37. Eggers, D. F., Jr., Gregory, N. W., Halsey, G. D., Jr., and Rabinovitch, B. S., "Physical Chemistry," Wiley, New York (1964), pages 330-2.

38. Hirschfelder, J. O., Curtiss, C. F., and Bird, R. B., "Molecular Theory of Gases and Liquids," Wiley, New York (1954), page 1110.

39. Hirschfelder, J. O., Curtiss, C. F., and Bird, R. B., page 1116.

40. Ross, S. and Olivier, J. P., "On Physical Adsorption," Interscience, New York (1964), *passim.*

41. Weber, S., *Communications from the Physical Laboratory at the University of Leiden, No. 216b* (1937).

42. Miller, G. A., *Journal of Physical Chemistry, 67,* 1359 (1963).

43. Euchen, A., editor, "Landolt-Börnstein, Zahlenwerte und Funktionen," Springer, Berlin (1950), pages 325, 369-71.

44. Jasper, J. J., "Laboratory Methods of Physical Chemistry," Houghton Mifflin, Boston (1938), page 39.

45. Magee, R. A., Master's Thesis in press, Georgia Institute of Technology (1972).

46. Young, D. M. and Crowell, A. D., page 66.

47. Hill, T. L., Emmett, P. H., and Joyner, L. G., *Journal of the American Chemical Society, 73,* 5102 (1951).

48. Joyner, L. G. and Emmett, P. H., *Journal of the American Chemical Society, 70,* 2353 (1948); Isirikyan, A. A. and Kiselev, A. V., *Journal of Physical Chemistry, 66,* 205 (1962).

49. Pierce, C., *Journal of Physical Chemistry, 73,* 813 (1969).

50. Young, D. M. and Crowell, A. D., page 226.

51. Adamson, A. W., "Physical Chemistry of Surfaces," page 478.

52. Young, D. M. and Crowell, A. D., page 185.

53. Young, D. M. and Crowell, A. D., page 237.

54. Singleton, J. P. and Halsey, G. D., Jr., *Journal of Physical Chemistry, 58,* 330 (1954).

55. Prenzlow, C. F. and Halsey, G. D., Jr., *Journal of Physical Chemistry, 61,* 1158 (1957).

56. Thomy, A. and Duval, X., *Colloq. Int. Centre Nat. Rech. Sci., No. 152,* 81 (1965).

57. Steele, W. A., *Advances in Colloid and Interface Science, 2,* 385 (1968).

58. Isirikyan, A. A. and Kiselev, A. V., *Journal of Physical Chemistry, 65,* 601 (1961).

59. Smallwood, R. E., "The Physical Adsorption of Benzene on Boron Nitride and Graphite," Master's Thesis, Georgia Institute of Technology (1967).

60. Davis, B. W. and Pierce, C., *Journal of Physical Chemistry, 70,* 1051 (1966).

61. Fowler, R. H., *Proceedings of the Cambridge Philosophical Society, 31,* 260 (1935).

62. Fowler, R. H. and Guggenheim, E. A., "Statistical Thermodynamics," Cambridge Press, Cambridge (1960), Chapter X.

63. Hill, T. L., *Journal of Chemical Physics, 17,* 520 (1949).

64. Hill, T. L., "Introduction to Statistical Thermodynamics," Addison-Wesley, Reading, Mass. (1960), page 165-6.

65. Kemball, C., *Proceedings of the Royal Society of London, A187,* 73 (1946).

66. Weast, R. C., inside back cover.

67. Weast, R. C., page F95.

68. Pitzer, K. S. and Scott, D. W., *Journal of the American Chemical Society, 65,* 803 (1943).

69. Kennard, O. in "International Tables for X-Ray Crystallography," Kynoch Press, England (1962), Vol. 3, page 276.

70. DeBoer, J. H., "The Dynamical Character of Adsorption," Clarendon Press, Oxford (1953), pages 110-2.

71. Ross, S. and Olivier, J. P., page 158.

72. DeBoer, J. H., page 110-121.

73. Fowler, R. and Guggenheim, E. A., page 430.

74. Sips, R., *Journal of Chemical Physics, 16,* 490 (1948).

75. Honig, J. M., *Journal of Chemical Physics, 24,* 510 (1956).

76. Honig, J. M., and Hill, E., *Journal of Chemical Physics, 22,* 851 (1954).

77. Honig, J. M., and Reyerson, L. H., *Journal of Chemical Physics, 23,* 2179 (1955).

78. Weast, R. C., page F5.

79. Straley, H. W., III and Husted, J. E., "Georgia Gravity Project" (Final Report Project A-943), Georgia Institute of Technology, Engineering Experiment Station, Atlanta, Georgia (1967).

VITA

Richard George Varsanik was born April 3, 1946, in Derby, Connecticut, to Helen and George Varsanik. He was reared in Seymour and graduated from Shelton High School in June, 1963. He entered The University of Bridgeport, Bridgeport, Connecticut, in September, 1963, and received the degree Bachelor of Arts in June, 1967. He entered the graduate division of the Georgia Institute of Technology in September, 1967, to study for the Doctor of Philosophy in the School of Chemistry. He was married to the former Rosemarie Shuster of Shelton, Connecticut, in January of 1969.